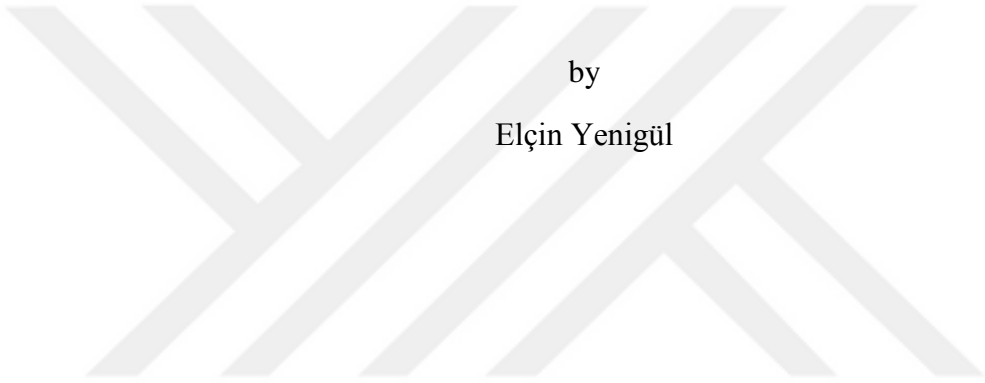


EXPERIMENTAL INVESTIGATION OF PEPTIDE SELF-ASSEMBLY STRUCTURES
AND APPLICATIONS



by
Elçin Yenigül

Submitted to Graduate School of Natural and Applied Sciences
in Partial Fulfillment of the Requirements
for the Degree of Doctor of Philosophy in
Chemical Engineering

Yeditepe University

2018

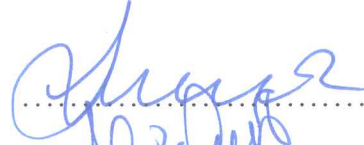
EXPERIMENTAL INVESTIGATION OF PEPTIDE SELF-ASSEMBLY STRUCTURES
AND APPLICATIONS

APPROVED BY:

Prof. Dr. Seyda Bucak
(Thesis Supervisor)


.....

Prof. Dr. Sinem Göktürk


.....

Assoc. Prof. Dr. Ali Demir Sezer


.....

Assoc. Prof. Dr. Erde Can


.....

Assoc. Prof. Dr. Tuğba Davran Candan


.....

DATE OF APPROVAL:/....../2018

ACKNOWLEDGEMENTS

I would like to thank everyone who become part of this thesis and research. Not only being part of it also taking very special places in my life. Especially,

To my supervisor Prof. Dr. Seyda Bucak, who guided me to reach where I am right now. With her strength, knowledge and vision; I steered the right path in this thesis and in my life. She has not been only a guide, also a model to me since we met. It is a privilege to be coached by you. Words are not enough to express my gratitudes and appreciation to you. Special thanks to you for your valuable support.

To Prof. Dr. Fikrettin Sahin who introduce me to biotechnology and open a new world in front of me, also provided laboratuary access for different stages of the research of this thesis. I would like to express my deepest appreciation and sincere to you for the support of solving the problems and being more than a leader.

To Prof. Dr. Ulf Olsson, SAXS Systems for collobration and extended scientific support,with his enormous knowledge,

To Dr. Celen Cagri Cenker and Anil Kurut, for their valuable support and friendship during SAXS studies in Lund,

To Burcin Asutay, Dr. Esra Coban, Secil Demir, Binnur Kiratli, Basak Senturk, Tuba Arjumend, Mustafa Yogurtcu, for their endless patience and replies about all cell culture related topics, not only in this thesis, also other stages of my life,

To Assist. Prof. Dr.Cem Levent Altan, Berk Gazioglu and Ilayda Degitz for their support and friendship,

To Erdinc Yenigul, for being always there as a brother and a good friend. Special thanks to him for his meaningful support for proof reading,

Last but not least, my father Ismet Yenigul, my mother Bahriye Yenigul for being more than a family. My inspirations, my supervisors, my supports. They are the best tools in my life to achieve my desires and my goals. Deepest thanks for believing me and encouraging me.

To my niece Leala Rose Yenigul, for her innocent questions and great expressions.

And of course, Elvin, my baby, my girl, my pearl, the most precious gift I ever received, the happiness of my life. I always feel there are something missing in your absence. When I walk down the stairs of the life path, you are the reason to dream for tomorrows. Special thanks to you for protecting my computer during typing stages of this thesis.

ABSTRACT

EXPERIMENTAL INVESTIGATION OF PEPTIDE SELF-ASSEMBLY STRUCTURES AND APPLICATIONS

The chemistry and applications of peptides are some of the major fields of biotechnology in today's world. This brings sufficient amount of interest to develop new bioengineering tools. Especially, introduction of nanotechnology to our lives allows researches to characterise the details at 'nano-scale' which opens up to more questions and as a result looking for more answers. Over the years, self-assembly developed to understand the dynamic behavior of the molecules with intermolecular interactions. Peptides are molecules which are small fragments of proteins that naturally exist and tend to self-assemble to form macrostructures.

In the current study, small oligopeptide molecules are considered. Peptide sequences with the combination of non-polar Alanine aminoacids with positively charged Lysine residues are investigated. Thus, Ala-Ala-Ala-Ala-Ala-Ala-Lys (A6K) and Ala-Ala-Ala-Ala-Ala-Ala-Ala-Ala-Ala-Lys (A10K) are the model peptides which were studied. A6K were dissolved and its self-assembly behaviour was investigated in both water (H_2O) and deuterium oxide (D_2O). Also the effect of altering pH to self-assembly of the A6K was studied by addition of NaOH. Self-assembling properties of A6K in the solution form were analysed by using imaging and scattering techniques. An extended phase diagram was obtained for the peptide A6K to classify the formed macrostructures. Since the molecule of the peptide is pulverized with a counter-ion, the electrostatic effect was also investigated for different counter-ions such as tri-flouro acetate (tfa^-) and chloride (Cl^-).

For application, the model peptide A10K was chosen and the cytotoxicity of peptide were studied. The self-assembly behaviour of A10K was previously studied. Varying cell lines were used during the experimental studies such as fibroblast (TM3, HDF), epithelial cells (Vero), endothel cells (HUVEC) and keratinocytes (HaCaT). Then, *in vitro* scratch assay were utilized for A10K, to explore this peptide as a potential tool for wound healing.

ÖZET

KENDİLİĞİNDEN KÜMELENEN PEPTİT YAPILARININ DENEYSEL OLARAK İNCELENMESİ VE UYGULAMALARI

Günümüz dünyasında peptit kimyası ve uygulamaları, biyoteknolojinin bazı temel alanlarından. Bu da, yeni biyomühendislik araçlarının geliştirilmesinde yeterli miktarda ilginin oluşmasını sağlamaktadır. Özellikle, nanoteknolojinin hayatlarımıza girmesi, araştırmacılara ‘nano-boyutta’ karakterizasyon kazandırmış olup, araştırılacak daha çok soru ve daha çok cevap getirmiştir. Nanoteknolojinin kazandırdıkları ile, moleküllerin moleküller arası etkileşimler ile dinamik davranışlarını anlamak için ‘kendi kendine kümeleşme’, araştırma alanında bir kavram olarak gelişmiştir. Peptitler doğal olarak bulunabilen ve proteinlerin küçük parçaları olan moleküllerdir ve makroyapılar oluşturmak üzere kendi kendine kümeleşme eğiliminde olabilirler.

Mevcut çalışmada küçük oligopeptitler ele alınmıştır. Apolar Alanin amino asidinin pozitif yüklü Lizin ile oluşturduğu peptit dizileri incelenmiştir. Dolayısıyla, Ala-Ala-Ala-Ala-Ala-Ala-Lys (A6K) ve Ala-Ala-Ala-Ala-Ala-Ala-Ala-Ala-Ala-Ala-Lys (A10K) çalışılmış olan model peptitlerdir. A6K hem su hem de döteryumlu su içerisinde çözülerek incelenmiştir. Ayrıca kendi kendine kümeleşmeye pH değişiminin etkisi de NaOH eklenerek çalışılmıştır. A6K’nın solüsyon içerisinde kendi kendine kümeleşme özellikleri görüntüleme ve saçılma teknikleri kullanılarak analiz edilmiştir. Oluşan makroyapıları sınıflandırmak için A6K peptidine genişletilmiş bir faz diyagramı oluşturulmuştur. Peptit molekülü, bir iyon değiştirici ile taşındığı için, elektrostatik etkiler, tri-floro asetat ya da klorür gibi farklı iyon taşıyıcılar kullanılarak incelenmiştir.

Çalışmada uygulama için, model peptit olarak A10K seçilmiştir ve sitotoksitesi araştırılmıştır. A10K’nin kendi kendine kümeleşmesi daha önce çalışılmıştır. Deneysel çalışma boyunca, fibroblastlar (TM3 ve HDF), epitel hücreleri (Vero), endotel hücreleri (HUVEC), ve keratinosit (HaCaT) gibi hücre hatlarıyla çalışılmıştır. Sonrasında, A10K çözeltisi ile hücre kültüründe yara iyileşmesi incelenmiştir.

TABLE OF CONTENTS

ACKNOWLEDGEMENTS.....	ii
ABSTRACT.....	iv
ÖZET	v
LIST OF FIGURES	viii
LIST OF TABLES.....	xii
LIST OF SYMBOLS/ABBREVIATIONS.....	xv
1. INTRODUCTION	1
2. THEORETICAL BACKGROUND	3
2.1. AMINO ACIDS	3
2.2. PEPTIDES.....	4
2.2.1. Secondary Structures - the α -Helix and β -Sheet	6
2.3. SELF-ASSEMBLY.....	8
2.3.1. Self-assembly of Peptides	11
2.3.2. Self-assembly of Peptide A6K and A10K.....	15
2.4. APPLICATIONS OF PEPTIDES.....	18
3. MATERIALS AND METHODS	19
3.1. MATERIALS	19
3.2. METHODS.....	21
3.2.1. Dynamic Light Scattering (DLS)	21
3.2.2. Zeta-Potential Analyzer.....	23
3.2.3. Light Microscopy	23
3.2.4. Small Angle X-Ray Scattering (SAXS)	25
3.2.5. Cryo-Transmission Electron Microscopy (Cryo-TEM).....	29
3.2.6. Infrared Spectroscopy (IR).....	30
3.2.7. Ultraviolet-Visible (UV) Spectroscopy.....	32
4. STUDY OF SELF-ASSEMBLY OF PEPTIDES.....	34
4.1. PREPARATION OF PEPTIDE SOLUTIONS	34

4.2. INVESTIGATION OF (TFA) ₂ -A ₆ K IN H ₂ O AND VARYING CONCENTRATIONS OF NaOH	35
4.2.1. Physical Properties	35
4.2.2. Self Assembly Behavior by SAXS Studies	38
4.2.3. Extended Phase Diagram.....	60
4.3. INVESTIGATION OF (Cl) ₂ -A ₆ K.....	65
4.3.1. Physical Properties	65
4.3.2. Self Assembly Behaviour by SAXS Experiments	66
4.4. SUMMARY OF (Cl) ₂ -A ₆ K IN D ₂ O AND (TFA) ₂ -A ₆ K AT VARYING NaOH SOLUTION.....	70
5. APPLICATION OF PEPTIDE A10K	72
5.1. MEASUREMENT OF PHYSICAL PROPERTIES OF PEPTIDE-MEDIUM SOLUTION.....	75
5.2. CYTOTOXICITY OF PEPTIDE A10K FOR VARIOUS CELL LINES	77
5.2.1 Tetrazolium Salt Based Assay (MTS Assay).....	77
5.2.2. Cell Viability Results of Peptide A10K for Different Cell Lines	78
5.3. APPLICATION OF THE PEPTIDE SOLUTION FOR WOUND HEALING.....	81
5.3.1. Preparation of Scratch Assay	81
5.4. RESULTS OF SCRATCH ASSAYS.....	82
5.4.1. Utilization of A10K for Scratch Assay by Using HaCAT Cells.....	82
5.4.2. Utilization of A10K for Scratch Assay by Using HDF Cells.....	87
6. RESULTS AND DISCUSSION	88
REFERENCES	91
APPENDIX A.....	102

LIST OF FIGURES

Figure 2.1. Basic configuration of the amino acid.....	3
Figure 2.2. The conventional features and pKa values of common amino acids	4
Figure 2.3. Scheme of peptide formation	5
Figure 2.4. N and C terminals of a peptide sequence	6
Figure 2.5. Configuration of α -Helix.....	7
Figure 2.6. Conformation of β -sheet.....	7
Figure 2.7. Static and dynamic self-assembly	9
Figure 2.8. Self-assembly of commutative and non-commutative	10
Figure 2.9. Various morphologies coexist through self-assembly.....	11
Figure 2.10. TEM data of the surfactant-like peptides A6D, V6D, V6D2, and L6D2 in water.....	13
Figure 2.11. Molecular structure of A6K	15

Figure 2.12. Molecular structure of A10K	16
Figure 3.1. Schematic representaion of DLS working principle	22
Figure 3.2. An image of a Dynamic Light Scattering instrument.....	22
Figure 3.3. An image of a Light Microscopy	24
Figure 3.4. Schematic layouts of common microscopy techniques.....	25
Figure 3.5. Schematic layout of a SAXS setup detecting the incident, scattered and transmitted X-Ray beams and the 2-D detector.....	26
Figure 3.6. Determination of an image of a protein by cryo-TEM that involves several stages.....	30
Figure 3.7. An image of an FTIR.....	31
Figure 3.8. An image of a UV-VIS spectrophotometer	33
Figure 4.1. Images of 8 per cent and 12 per cent (tfa) ₂ -A6K peptide at various NaOH Concentrations	38
Figure 4.2. 14 Per cent (tfa) ₂ -A6K in 0.01 M NaOH for varying models	41
Figure 4.3. 14 Per cent (tfa) ₂ -A6K in 0.1 M NaOH for varying models	42

Figure 4.4. 14 Per cent (tfa) ₂ -A6K in 0.2 M NaOH for varying models	43
Figure 4.5. 14 Per cent (tfa) ₂ -A6K in 0.5 M NaOH for varying models	45
Figure 4.6. 12 Per cent (tfa) ₂ -A6K in 0.5 M NaOH for varying models	47
Figure 4.7. 10 Per cent (tfa) ₂ -A6K in 0.1 M NaOH for varying models	48
Figure 4.8. 8. Per cent (tfa) ₂ -A6K in 0.1 M NaOH for varying models	49
Figure 4.9. 10. Per cent (tfa) ₂ -A6K in 0.2 M NaOH for varying models	51
Figure 4.10. 16 Per cent (tfa) ₂ -A6K in 0.01 M NaOH for varying models	52
Figure 4.11. 6 Per cent (tfa) ₂ -A6K in 0.2 M NaOH for varying models.....	53
Figure 4.12. 12 Per cent (tfa) ₂ -A6K in 0.2 M NaOH for varying models.....	55
Figure 4.13. 12 Per cent (tfa) ₂ -A6K in 0.1 M NaOH for varying models	56
Figure 4.14. 8 Per cent(tfa) ₂ -A6K in 0.2 M NaOH for varying models	58
Figure 4.15. Imaging data of (tfa) ₂ -A6K	60
Figure 4.16. FTIR spectra of for (tfa) ₂ -A6K.....	61

Figure 4.17. Estimation of ‘cac’ for $x=0.2$ and $x=0.5$ for different mass ratio.....	62
Figure 4.18. FTIR spectra of $w_i = 0.16$ A6K in pure water (black squares) and $w_i= 0.125$ with $x=1$ (red circles).....	63
Figure 4.19. Phase diagram of $(tfa)_2$ -A6K.....	64
Figure 4.20. Image of $(Cl)_2$ -A6K for varying concentration in D_2O	66
Figure 4.21. 14 Per cent $(Cl)_2$ -A ₆ K in D_2O for varying model.....	68
Figure 4.22. 16 Per cent $(Cl)_2$ -A ₆ K in D_2O for varying model.....	69
Figure 5.1. Summary of phases for wound healing	74
Figure 5.2. A10K viability for HUVEC	79
Figure 5.3. A10K viability for VERO	79
Figure 5.4. A10K viability for TM3	80
Figure 5.5. A10K viability for HDF	80
Figure 5.6. A10K viability for HaCaT	81

Figure 5.7. Light Microscopy images of scratch assay for HaCaT Cells 84

Figure 6.1. Physical features of $(tfa)_2-A_6K$ in H_2O 88



LIST OF TABLES

Table 3.1. Chemicals for cytotoxicity of A10K.....	19
Table 3.2. Cells and solutions used for cytotoxicity of A10K.....	20
Table 4.1. Properties and image of (tfa) ₂ -A6K peptide, in H ₂ O.....	35
Table 4.2. (tfa) ₂ -A6K in 0.01 M NaOH, in water.....	36
Table 4.3. (tfa) ₂ -A6K in 0.1 M NaOH, in water.....	36
Table 4.4. (tfa) ₂ -A6K in 0.2 M NaOH, in water.....	37
Table 4.5. (tfa) ₂ -A6K in 0.5 M NaOH, in water.....	37
Table 4.6. (tfa) ₂ -A6K in 1 M NaOH, in water.....	37
Table 4.7. Summary of the existance of the structures for three models at different NaOH molarity while the peptide concentration kept constant	58
Table 4.8. Summary of the existance of the structures for three models at different peptide concentration while [NaOH] kept constant	59
Table 4.9. Prepared samples at various concentrations at D ₂ O for (Cl) ₂ -A6K.....	65

Table 4.10. The cross section diameters and the cross section edge lengths.....	70
Table 5.1. The events that take place during normal wound healing phases.....	73
Table 5.2. Zeta-Potential Data of 2×10^4 $\mu\text{g/mL}$ A ₁₀ K in medium, only medium (DMEM HG) and FBS	76
Table 5.3. pH Measurements of 2×10^4 $\mu\text{g/mL}$ A ₁₀ K in medium, only medium (DMEM HG) and FBS	76
Table 5.4. Per cent closure of the wound for 12.5 $\mu\text{g/mL}$ A10K at various time intervals	84
Table 5.5. Per cent closure of the wound for 25 $\mu\text{g/mL}$ A10K at various time intervals....	85
Table 5.6. Per cent closure of the wound for 50 $\mu\text{g/mL}$ A10K at various time intervals....	86
Table 5.7. Per cent closure of the wound for 100 $\mu\text{g/mL}$ A10K at various time intervals..	86

LIST OF SYMBOLS/ABBREVIATIONS

A	L-alanine
A	Wave amplitude
A	Edges of parallelepiped form
b	Scattering length
A_s	Scattering amplitude
A6K	Ala-Ala-Ala-Ala-Ala-Ala-Lys
A10K	Ala-Ala-Ala-Ala-Ala-Ala-Ala-Ala-Ala-Ala-Lys
Cl ⁻	Chloride
D	L-aspartic acid
K	Lysine
k	Wave vector
L	Length of the circular or elliptical cylinder
$P(q)$	Form factor
$P(r)$	Scattering length intensity
$P^*(q)$	Form factor of infinitely thin rod
$P_{CS}(q)$	Form factor of the cross section
q	Scattering vector
r	Distance of the detector
R	L-arginine
R_1	The cross section of elliptical cylinder
R_2	The cross section of elliptical cylinder
R	The cross section of circular cylinder
tfa ⁻	Tri-flouro acetate
W	L-tryptophane
V	L-valine
V	Scattering volume
λ	Wavelength

AFM	Atomic force microscopy
Cac	Critical aggregation concentration
CD	Circular dichroism
Cryo-TEM	Cryo-transmission electron microscopy
DLS	Dynamic light scattering
DMEM	Dubleco Eagle's Minimum Essential Medium
DMSO	Dimethyl sulfoxide
D ₂ O	Deuterium oxide
DPBS	Dulbecco's phosphate buffered salt solution
ERK	Extracellularly-responsive kinase
FBS	Fetal bovine serume
FTIR	Fourier-transform infrared
HaCaT	Human epidermal keratinocytes
HDF	Human dermal fibroblast
HUVEC	Human umbilical vein endothelial cell
IDRs	Innate defense regulators
IR	Infrared
JNK	c-Jun N-terminal kinase
MAPK	Mitogen-activated protein kinase
MTS Assay	Tetrazolium Salt Based Assay
NMR	Nuclear magnetic resonance
PDGF	Platelet-derived growth factor
TGF- β	Transforming growth factor beta
Tiger 17	WCKPKPKPRCH
TM3	Leydig cell(<i>Mus musculus</i> , mouse)
UV-VIS	Ultraviolet-visible spectroscopy
WAXS	Wide angle X-ray scattering
XRD	X-ray diffraction
Vero	Kidney epithelial cell

1. INTRODUCTION

Life started with atomic and molecular base interactions where every organism find their own way in this endless evolution and adaptation. Modern science studies show us that, every organism contains molecules where these molecules are made of nucleic acids, amino acids, fatty acids. In order to understand the behavior of more complex structures, it is important to investigate the sequencing and self-assembly of smaller molecules which lead to those complex structures. By conceiving the mechanism of self-assembly processes in organisms, the scientists recognised that these self-assembled structures could supply enormous opportunities for designing novel supramolecular structures in the field of electronics, optics, biomedicine for synthetic, biological, non-biological or geochemical systems [1,2].

Development and improvements of modern peptide chemistry lead to the possibility of synthesizing desired peptides which assist to the systematic investigation of the relationship between significant oligopeptide molecule and its macroscopic phases and the structures formed in such processes [3-5]. Insights on the formation behavior of peptide self- assembly is crucial not only procuring nanomaterials for the desired features but also in combating Alzheimer's and Parkinson's neurodegenerative diseases. These fundamental disorders are quite related with the accumulations of some short amyloid forming oligopeptides in human brain [3].

Spontaneous association of molecules to form three-dimensional multicomponent complexes can be termed 'molecular self-assembly'[6]. It is one of the aspects of fabricating new materials that contain intramolecular forces such as non-covalent interactions of hydrogen bonding, hydrophobic, electrostatic, metal—ligand, stacking or van der Waals interactions. These are quite dynamic and mostly fragile interactions depending on their relatively feeble nature, changing from less than 5 kJ mol^{-1} for van der Waals interactions to up to 120 kJ mol^{-1} for hydrogen bonding. On the other hand, the energies of covalent bonds can rise up to 400 kJ mol^{-1} . Even so, certain amount of these weak interactions or their combination can still result in stable assembling properties. Different self-assembled supramolecular structures have been prepared so far using these

interactions in the field of modern biotechnology and plenty of new self-assembling nanomaterials are arranged into aligned complex structures [2].

Since it is considered that the accumulation of peptides in human brain causes degenerative diseases as a result of self-assembly of peptides, preventing peptide accumulation can be accomplished by understanding the biochemical and biophysical nature or mechanism that underlies it [7]. Therefore, an increasing attention has been given to the amyloid peptides or local part of these peptides because of their relationship with neurodegenerative diseases [6].

The formation of materials in solutions is a widespread phenomenon in synthetic, biological and geochemical systems. In all of these environments, materials development proceeds through dynamic processes, such as nucleation, self-assembly, crystal growth and coarsening [8].

Here, in the current study self-assembly of peptide of A6K and A10K is investigated at varying physicochemical environments. Taking this further, cytotoxicity studies of these peptides were studied and wound healing assays were performed to overlook the application field for enlarging the study in the biotechnological point of view. Combining all the information obtained a general understanding on peptide self assembly is aimed to be achieved.

2. THEORETICAL BACKGROUND

2.1. AMINO ACIDS

An amino acid is an organic substance, with the general formula of $\text{H}_2\text{NCHRCOOH}$, containing an amino group and a carboxyl functional group that binds to a saturated carbon atom. Figure 2.1 represents the structure of an amino acid.

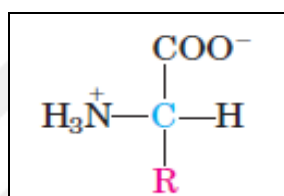


Figure 2.1 Basic configuration of the amino acid (R group, side chain, is different for each amino acid, except for glycine where $\text{R}=\text{H}$ for that) [9]

Apart from glycine which is the simplest amino acid, amino acids have a stereogenic center on the carbon atom. The asymmetric carbon at the center allows amino acids to have an optical activity except for glycine.

When the amino group of the amino acid is linked directly to the central carbon atom that is α -carbon, it is referred to as α -amino acids. All of the 20 common amino acids that occur naturally in proteins are α -amino acids. Besides the α -carbon that has the amino and carboxyl group, it also engages to an R side chain. R groups differ in size, electric charge, structure and solubility in water that allows the variations in amino acids. Depending on the properties of the side chains, R group, amino acids are classified, in particular, considering the polarity or affinity to interact with water. The character of side chain varies widely from hydrophobic (non-polar) to hydrophilic (polar). Some features and pKa values of common amino acids are listed in Figure 2.2.

Amino acid	Abbreviation/ symbol	M_r	pK_a values			pI	Hydropathy index*	Occurrence in proteins (%) [†]
			pK_1 (—COOH)	pK_2 (—NH ₃ ⁺)	pK_R (R group)			
Nonpolar, aliphatic								
R groups								
Glycine	Gly G	75	2.34	9.60		5.97	-0.4	7.2
Alanine	Ala A	89	2.34	9.69		6.01	1.8	7.8
Proline	Pro P	115	1.99	10.96		6.48	1.6	5.2
Valine	Val V	117	2.32	9.62		5.97	4.2	6.6
Leucine	Leu L	131	2.36	9.60		5.98	3.8	9.1
Isoleucine	Ile I	131	2.36	9.68		6.02	4.5	5.3
Methionine	Met M	149	2.28	9.21		5.74	1.9	2.3
Aromatic R groups								
Phenylalanine	Phe F	165	1.83	9.13		5.48	2.8	3.9
Tyrosine	Tyr Y	181	2.20	9.11	10.07	5.66	-1.3	3.2
Tryptophan	Trp W	204	2.38	9.39		5.89	-0.9	1.4
Polar, uncharged								
R groups								
Serine	Ser S	105	2.21	9.15		5.68	-0.8	6.8
Threonine	Thr T	119	2.11	9.62		5.87	-0.7	5.9
Cysteine	Cys C	121	1.96	10.28	8.18	5.07	2.5	1.9
Asparagine	Asn N	132	2.02	8.80		5.41	-3.5	4.3
Glutamine	Gln Q	146	2.17	9.13		5.65	-3.5	4.2
Positively charged								
R groups								
Lysine	Lys K	146	2.18	8.95	10.53	9.74	-3.9	5.9
Histidine	His H	155	1.82	9.17	6.00	7.59	-3.2	2.3
Arginine	Arg R	174	2.17	9.04	12.48	10.76	-4.5	5.1
Negatively charged								
R groups								
Aspartate	Asp D	133	1.88	9.60	3.65	2.77	-3.5	5.3
Glutamate	Glu E	147	2.19	9.67	4.25	3.22	-3.5	6.3

Figure 2.2. The conventional features and pKa values of common amino acids [9]

Since α -carbon is the chiral center, special nomenclature was developed to designate the configuration of the functional groups at the stereogenic center to determine the absolute configuration. Thus, D and L system is used to represent isoforms. Most of the biological samples with a chiral center are found in one stereoisomeric form either D or L. Generally, proteins contain L-isoforms while very few amino acid residues occur in D-form in small peptides [9-12].

2.2. PEPTIDES

Peptides are molecules that are composed of amino acids that have unique functions which are supplied by individual features of each amino acid. The specificity of the function is

further increased by the constitution of several amino acids to allow peptides act as chemical transporters, specific stimulators or inhibitors and neurotransmitters [13].

From a chemical point of view, peptides are formed via peptide bonds between amino acids through a condensation reaction. When two amino acids cluster, the amino group of the amino acid reacts with the carboxyl of the other, results the condensation reaction that produce the peptide bond. This linkage occurs by the removal of water molecule through dehydation process. Thus, peptides contain few amino acids residues linked together by peptide bonds [11, 14, 15]. If the number of the amino acid residue is less that 30, the term oligopeptide is used to refer to the structure [16]. These are relatively small molecules compared to the proteins since the proteins form when the molecular weight of the peptide is greater than about 12,000 g/mol. o acid residues. Still, it is possible to say proteins may contain thousands of amino acids. Molecules have more than 100 amino acid residues are reffered as proteins while less are regarded peptides [9, 13].

Figure 2.3 represents the process of peptide bond formation to yield a dipeptide through condensation.

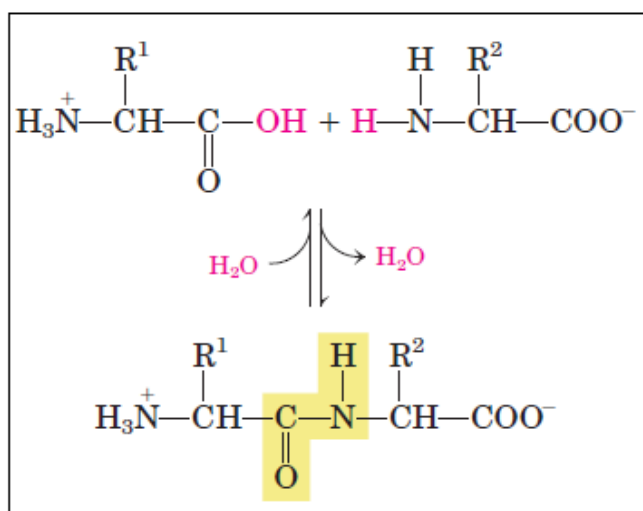


Figure 2.3. Scheme of peptide formation [9]

The organization or the sequence of the peptide link specifies the covalent structure of the compound. It is regarded as primary structure. Apart from this, some non-covalent interactions such as hydrogen bonding exists between amide groups that define the

secondary structure of the molecule. Also, proteins and peptides may have tertiary structures through chain folding as a result of polar or non-polar interactions or disulfide bridges. Finally, if more than one polypeptide chain exists; quaternary structure describes the packing of the chain.

Each peptide has a free amino group that is referred as amino end or N-terminal. On the opposite side of the peptide, a free carboxyl group appears in the chain and is named as carboxyl terminal or C-terminal. Figure 2.4 describes the terminals of a peptide [13].

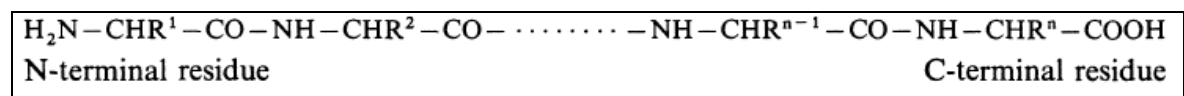


Figure 2.4. N and C terminals of a peptide sequence [13]

2.2.1. Secondary structures - the α -Helix and β -sheet

Secondary structures of the proteins or polypeptides occur through the localized parts of the molecule that results in three-dimensional conformation. Hydrogen bonding interaction exists between the N-H proton of the amide and C=O oxygen of the other. Thus, two possible stable organization of the structure may form, α -Helix and β -sheet.

When the chain of the peptide folds in particular into the right-handed spiral between the carboxyl oxygen and the amine hydrogen of the fourth residues, α -Helix structure grows. α -Helix form is shown in Figure 2.5.

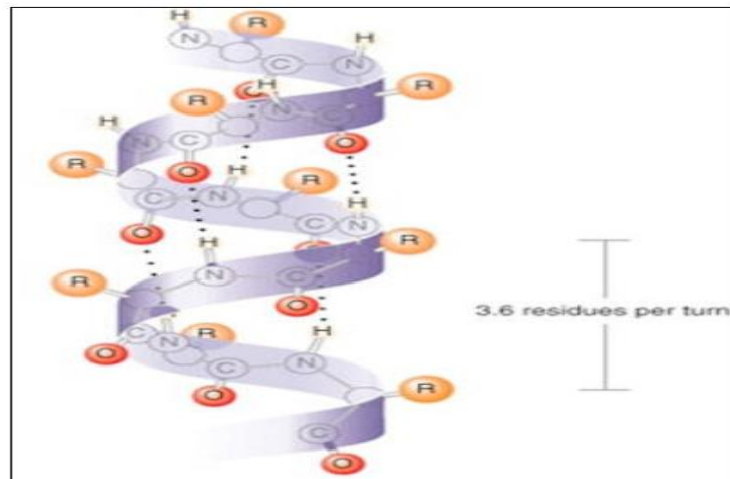


Figure 2.5. Configuration of α -Helix [17]

The other most frequently sighted secondary structure is β -sheet. In this structure, two or more peptide chains or also referred as strands align side-by-side as shown in Figure 2.6. Here, hydrogen bonding exhibits in between carboxyl and NH groups of backbone of the peptides.

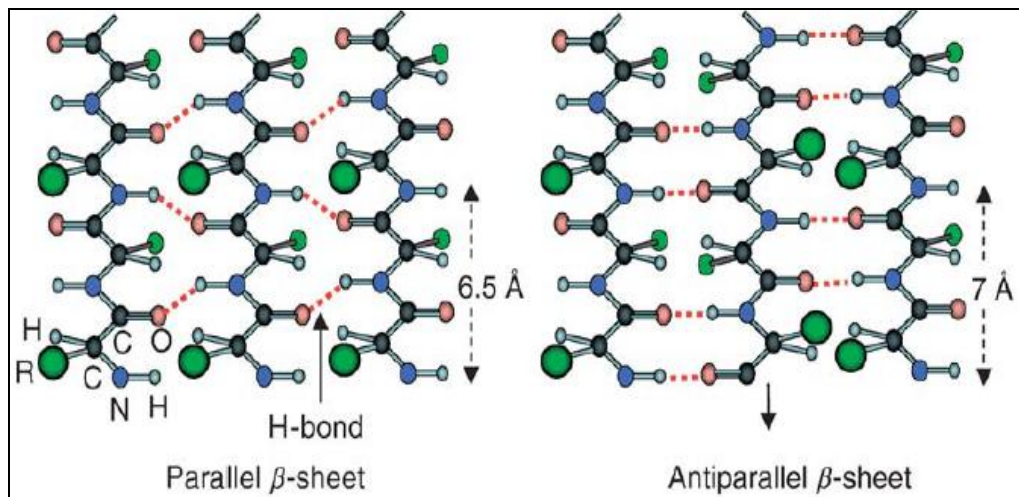


Figure 2.6. Conformation of β -sheet [18]

The β -sheet conformation composes in two forms. If the strands run into the same aspect, parallel β -sheet occurs. On the other hand, when the strands line up in opposite directions, it is called antiparallel β -sheet [19, 20].

Additionally, the major distinction in between β -sheet and α -Helix is that hydrogen bonding forms between different polypeptides in β -sheet whereas it occurs within the same strand in α -Helix [11, 21].

The analysis and the determination of the secondary structures can be obtained by using infrared spectra. The most convenient infrared band for protein or peptide structures in aqueous media is amide I band which exists roughly between 1700 and 1600 cm^{-1} . The amide I band supplies significant amount of the C=O stretching vibration of the amide group linked to the flat NH bending [22].

2.3. SELF-ASSEMBLY

In life, there are some causes to the demand of clarifying self-assembly. One of them is organisms are attracted by the organization of order from disorder. Furthermore, living cells tend to self-assemble that increase the importance of understanding the mechanism underlying self-assembly to sight the life. Also the cell allows enormous examples of functional self-assembly to inspire envision of non-living systems [23, 24]. The multicomponent three dimensional complex structures form in nature through the association of the molecules result as molecular self-assembly [6].

The definition of the term of 'self-assembly' is quite elastic. Although it is possible to confuse the description of it with the 'formation', there are distinct diversities between them that do not make them synonymous. Self-assembly is a reversible system and can be controlled by the certain construction of the components that separates it from formation. It is a spontaneous phenomenon in which the pre-existing components (separate or certain parts of the disordered structure) of the process organize into patterns or larger functional structures without human intervention. Self-assembly process involves intermolecular bonds via non-covalent interactions such as hydrogen bonding, electrostatic or van der Waals interactions [2, 6]. It is possible to find out self-assembling processes within nature and technology.

There are two types of self-assembly. One of them is static and the other is dynamic. Figure 2.7 represents static and dynamic self-assembly examples.

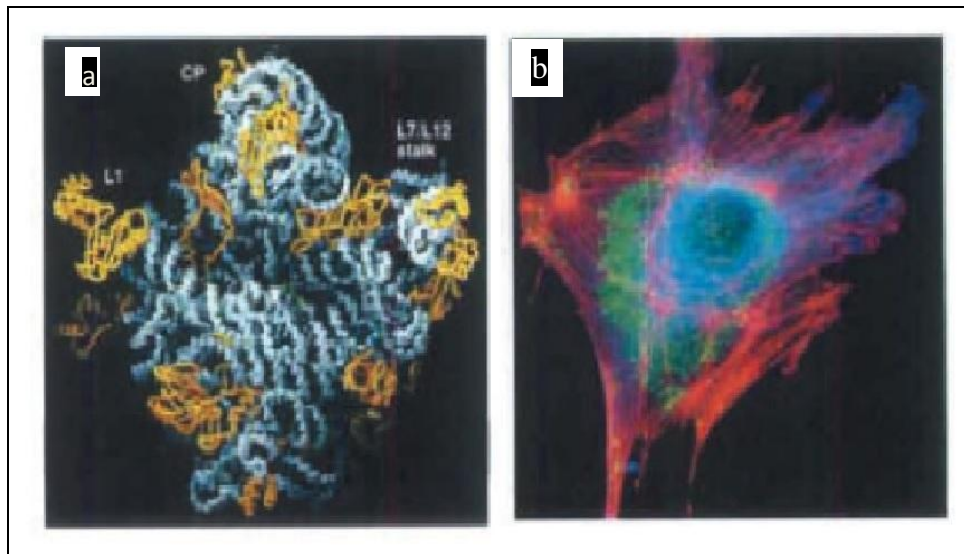


Figure 2.7. Static and dynamic self-assembly a) Static self-assembly of ribosome's crystal structure b) Optical micrographs of dynamic self-assembly of a cell [24]

In static self-assembly the system is in global or local equilibrium and does not conflict energy. Here formation of the aligned structure may need energy but once it is formed, then it is stable. On the other hand, in dynamic self-assembly the association of the ordered structures or patterns is valid only if the process dissipates energy [24-27].

Molecular self-assembly is characterized by spontaneous diffusion and specific association of molecules dictated by non-covalent interactions. There is vast number of recent examples involving different molecular entities: organic molecules, proteins, peptides, DNA and others. Although this is not a comprehensive list, it represents the diversity of building blocks that can be used. Assembly can be biologically inspired where complex nanoscale structures are made to function with precision. For example, cells can be thought as active units that respond to their environment and are epitomes of advanced microtechnology. However, the hardware of cells is implemented from biomolecules such as proteins, lipids and DNA, often self-assembled into functional nano scale structures.

Nanoassemblies, recognition events are controlled by convenient thermodynamics, often mediated through weak non-covalent interactions like hydrogen bonding, electrostatic interactions containing dipoles and formal charges, hydrophobic forces and van der Waals interactions. Eventhough lot of these interactions may be minor in magnitude (<5

kcal/mol), the large number formed in the final assembled structure is significant. The large entropic cost of ordering molecules is only slightly off-set by the favorable enthalpy gained from these weak interactions, rendering the self-assembled system to exist in a thermodynamic equilibrium. Therefore, self-assembly is a dynamic process through weak forces imposing reversible associations to obtain an energetically optimized supramolecular construction.

Non-covalent synthesis of supramolecular structures can be classified as commutative or non-commutative. Commutative self-assembly describes a process in which given steps leading to the formation of the supramolecular structure may be interchanged (Figure 2.8.a). Non-commutative self-assembly takes place through a sequence of steps that cannot be interchanged; for example, a hierarchical process in which intermediate structures are formed and subsequently assemble into complex systems (Figure 2.8.b).

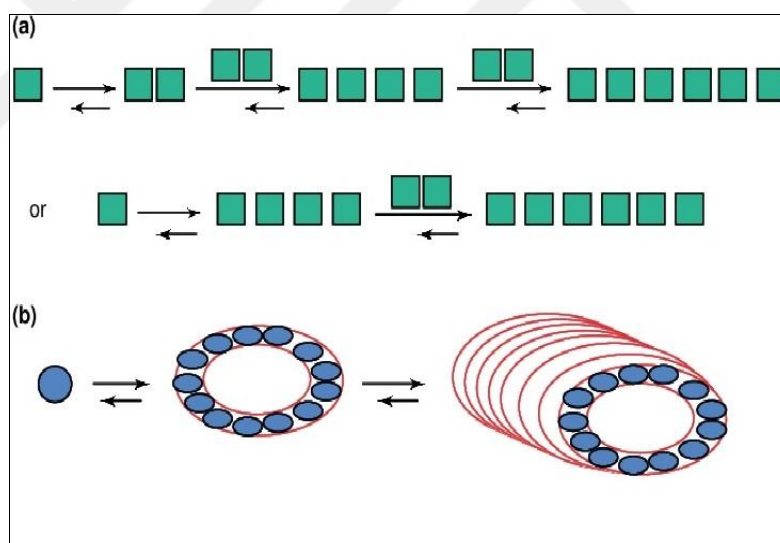


Figure 2.8. Self-assembly of commutative and non-commutative a) Steps of commutative process b) Non-commutative processes aligning hierarchical order in the assembly system

[28]

2.3.1. Self-assembly of Peptides

Understanding the mechanism of self-assembly and the outcomes of it at nanoscale bring an increasing attention of designing novel supramolecular structures. Therefore, plenty of self-assembling structures have been fabricated and analyzed such as block copolymers, phospholipids, complex DNA aggregates, enzymes, proteins and peptides [29-32]. During the process of designing the structure, some features of the building block is considered such as chemical functionality, molecule morphology, and mechanical characteristic of the molecule. Peptides are one of the molecular building blocks that are used to prepare self-assembled structures having an extend ability of biofunctionality such as ligand and metal recognition, biocompatibility or biodegradability. It also allows the promising possibility of attaching intramolecular peptide folding to material features [29, 30]. The self-organizations of peptides with varying morphologies have shown at Figure 2.9.

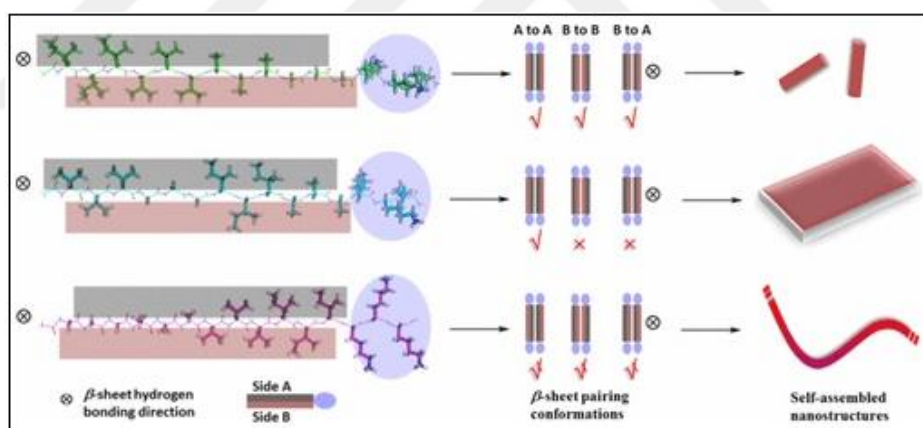


Figure 2.9. Various morphologies coexist through self-assembly [33]

Although it is possible to come across to polypeptide self-assembly such as amyloid fibril formation or microbial physiological systems related to medical disorders, the organization features of the peptides have inspired the scientists for developing bio-nanoassemblies, involving nanotubes, nanofibrils, nanotapes and hydrogels at nanoscale [32].

One of the first studies on self-assembled peptide structures was obtained by Zhang unintentionally while working on yeast genetics and protein chemistry. The focus of the

study was to understand the structure of left-handed Z-DNA. During the study Zhang accidentally found something novel which is the identification of a protein called Zuotin that binds to left-handed DNA in the presence of excess amount of salmon DNA containing right-handed B-DNA and random DNA structures. Zuotin contains repeating sixteen peptide residues for the sequence n-AEAEAKAKAEAEAKAK-c (EAK16-II). This peptide has been improved to design a class of basic beta-sheet peptides. By the sight of this serendipitous discovery, the working group has an inspiration of designing varying members of these peptides that can be used in tissue engineering as three-dimensional scaffolds. They found out that four different segment of yeast zuotin (RDA 16-I, RAD16-II, EAK-I and EAK16-II) have self-assemble forming beta-sheet organization in an aqueous solution and further go into form nanofiber scaffolds. Moreover, self-complementary peptide EAK16 generates an insoluble membrane in a macroscopic scale. Some circular dichroism (CD) studies proved an identical spectrum of β -sheet formation with the ellipticity between 195-220 nm [34].

The search of Zhang and co-workers have undergone for the self-assembled oligopeptides which are a new type of biodegradable and bioequivalent biomaterials. These structures have a great potential for the application in the field of biomedical and pharmaceutical areas [35]. The basic characteristic of this class of material is having a sequence of changeable hydrophobic side chain and charged side chain that was invented by Zhang et al. [36]. They have demonstrated the potential of using non-conjugated peptide as a monomer to obtain organized nano scale structures. These relatively small linear peptides containing around 7-8 residues are distinguished by well-determined hydrophobic and hydrophilic residues. The study was performed by characterizing the peptide with a hydrophilic head containing aspartic acid and a tail of hydrophobic amino acids that are alanine, valine or leucine. These peptides denote as surfactant-like properties which are analogous to the other biological surfactants. In aqueous solution, these peptides self-assemble into well-organized nanotubes and nanovesicles via molecular interactions of hydrogen bonding which was represented in Figure 2.10 [6, 37].

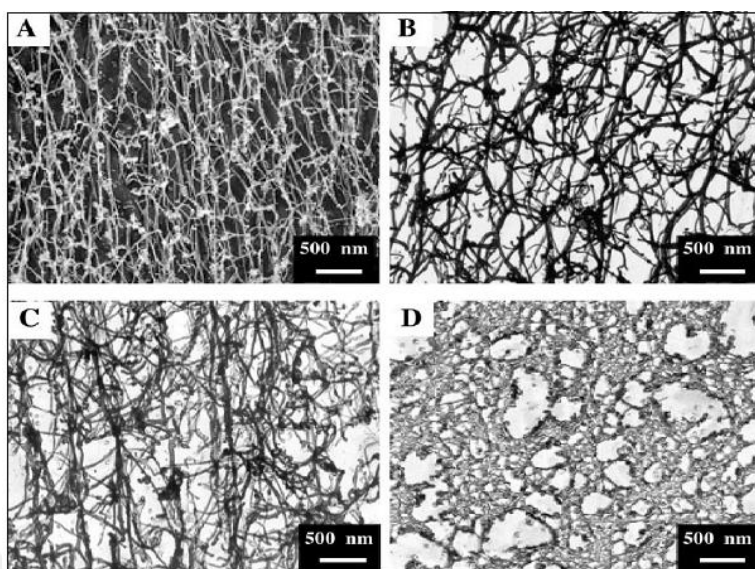


Figure 2.10. TEM data of the surfactant-like peptides A6D, V6D, V6D2, and L6D2 in water a) A6D b) V6D c) V6D2 d) L6D2 [37]

Zhao supported these findings and reveals that although these surfactant-like peptides have varying arrangement and totally distinct compositions; they collaborate about a common feature. They composed of a hydrophilic head containing 1-2 charged amino acids and a hydrophobic tail consisting of four or more consecutive hydrophobic amino acids. Due to this basic molecular construction, these peptides conduct themselves to self-assemble in aqueous solution to form nanostructures at varying sizes. Sufficient amount of work have supported that almost all of the surfactant like peptides undergo self-assembly into dynamic nanoscale structures in water media [38-40]. Also, the structures that are fabricated by alanine and valine containing tails are more stable and uniform comparing to the peptides having tails with glycine, isoleucine and leucine [41].

Among the scientists self-assembling properties of peptides have been examined and Ghadiri and co-workers were the first to define a new type of organic nanotubes related to cyclic polypeptides to be formed rationally. The design of these cyclic polypeptides was performed by changing the even number of D- and L- amino acids that form self-assembled nanotubes via hydrogen bonding. The diameter of these nanotubes can be managed by alternating the amount of amino acids in the peptide sequence [6]. These

peptide nanotubes are revealed as a new class of antibiotic agents since they are toxic to bacteria [42].

Cyclic polypeptide structures were also investigated by Seebach and co-workers. They revealed that cyclic tetrapeptides contain chiral β -amino acids tend to form disklike conformations and pack to embrace hollow tubular patterns through the results of X-ray powder diffraction and molecular modeling of cyclo[cyclo[-(b3-(S)-HAla)4-], cyclo[-(b3-S)-HAla3-(R)-HAla)2-], and cyclo[-(b3-(S)-HAla)2-(b3-(R)-HAla)2-] [43]. Lanreotide octapeptide is another cyclic peptide that was studied to form tubular structures with nanometric scales in water solution. It was revealed that the self-assembling process of this peptide is based on the distinction of aliphatic/aromatic parts that promote the formation of β -sheet fibrils [44].

Peptide-based nanostructures were also obtained through self-aggregation of 12 short ionic oligopeptides composed of 4-7 amino acid residues such as RADARAD, RWDW, RDWW, RVDV and RDVV (The letters correspond to: A= L-alanine, D= L-aspartic acid, W= L-tryptophane, R=L-arginine, V=L-valine). It was found if the hydrophobicity of the neutral residues increases, the critical aggregation concentration (cac) of the tetrapeptides decreases [29].

A wide range of peptides and proteins have offered to fabricate nanofiber alignment such as well-known amyloid fibril formation which causes several diseases in physiological conditions. Much work have naturally focused on the amyloid forming peptides, or selected fragments of these because of the close connection to neurodegenerative diseases like Alzheimer, Parkinson disease, bovine spongiform encephalopathy, or type II diabetes [45-51]. These well-ordered and structures are still being investigated by the research groups to identify the mechanism under it. Alignment of the nanofibers are well-organized and they represents significant regularity and, at some point, helical periodicity. In the point of dimensions, these nanofibers resemble to the extracellular matrices that are considerable for allowing a diversity of cells to adhere together to occur tissues [52].

Self-assembling of peptides to serve supramolecular structures of helical ribbons have been obtained with the arrangement of β -sheet peptide, KFE8 (sequence of amino acid: FKFEFKFE) by Hwang et al. Computational approach of KFE8 satisfied the helical

ribbons at certain dimensions [53]. Studies for β -helix structures have been sustained and Perutz and colleagues have demonstrated the formation of nanotubes from polyglutamines. They represented the span of the polypeptide chain and the amount of consecutive glutamines residues on the peptide chain is crucial for the occurrence of β -helix structure. This outcome was also proved by computational simulations. Since polyglutamines are significant biocompounds, understanding the nanotube formation of polyglutamines brought a great insight to design novel scaffolds [52, 54, 55].

2.3.2. Self-assembly of Peptide A6K and A10K

So far many short peptides have been worked on self-organization processes into different structures including fibers, tapes, tubes and spheres. In the current study, short peptides of A6K and A10K have been investigated for the dynamic behavior at varying conditions.

Cationic peptide A6K has six hydrophobic alanine chains with a hydrophilic lysine head group while A10K consists of ten alanines and a single lysine. Alanine has no charge at the side chain which composed of a single methyl is represented in Figure 2.11-2.12.

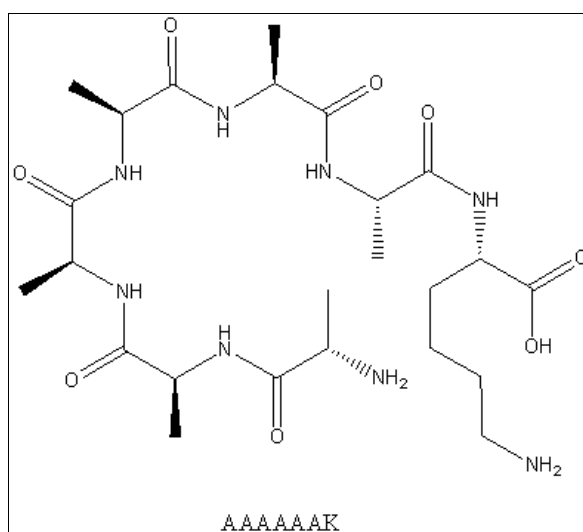


Figure 2.11. Molecular structure of A6K

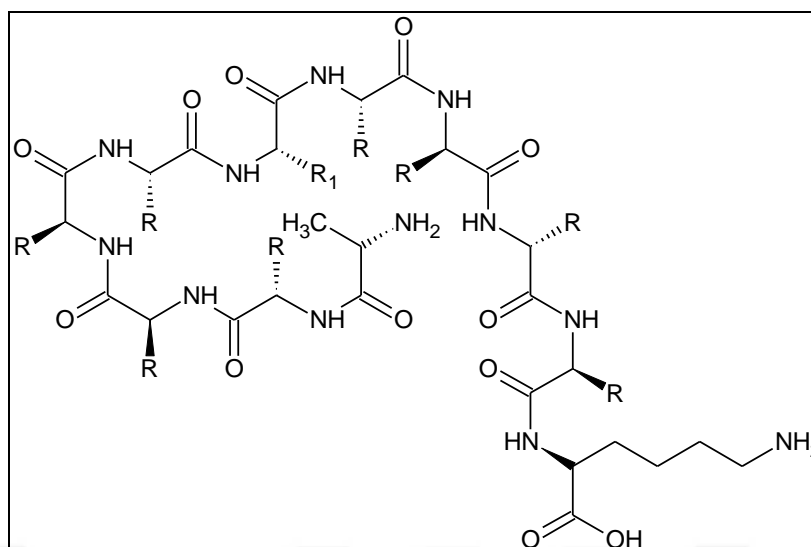


Figure 2.12. Molecular structure of A10K

As it can be clearly seen, N-terminus of this peptide contains alanine, the residue of -NH_2 in the structure is placed at the other side. Since consecutive five alanine groups that are connected each other via peptide bonds do not have any side chains, they occur the hydrophobic part of the peptide. On the other hand, lysine terminates the sequence of the peptide with -COOH group that is located in C-terminus. However, lysine has an -NH_2 containing side chain at this location. pK_a values of these groups are approximately 10 for -NH_2 groups in N-terminus of alanine and in side chain of lysine and approximately 2 for -COOH in C-terminus of alanine.

Some of the studies were performed by using end-capped peptide. Because of the changes in N-terminus due to the variation of pH, this terminal has covered with -CH_3 group. Zhang and co-workers are one of the first groups to investigate and design novel nanostructures by altering the sequence of the peptide or hydrophobic and hydrophilic region of the chain, have also worked for these end-capped peptides. When N-terminus of the peptide is capped, the structure resembles to more likely surfactant. So, it solely constitutes a hydrophilic group at one end and a hydrophobic tail at the other side that is similar to an amphiphilic molecule. Therefore, they introduced lipid-like peptides also named peptide surfactants to form dynamic structures in pure solution such as other surfactants, depending on to the concentration, remarkably pH variation or ionic strength of salts parameters. They reported a detailed study about peptides of end-capped A6K and

A6D with relevant images of atomic force microscopy (AFM) and results of dynamic light scattering (DLS) [56]. Unlikely the peptides they study have formed vesicular and tubular nanostructures which have obtained at different concentrations for distinctively varying sizes, features and elasticity.

On the other hand, in the present study, N-terminus of the peptides is not capped which allows to carry positive charge in aqueous solution and certainly does not exhibit the feature of surfactant. This peptide is remarkably different from similarly sequenced peptides where the N-terminal is end-capped. End capping completely changes the charge distribution on the peptide, leading to novel structure formation. Bucak and her research group published some interesting results for investigation of non-capped A6K where nanotube formation was observed and the cryo-TEM results were well-supported with SAXS experiments in shedding light on detailed structure analysis [3]. Extended search was performed for the model peptide AnK, where A is alanine and K is lysine when $n=4, 6, 8$ and 10 . It revealed that A4K has very high water solubility and did not exhibit a significant self-assembly. In addition, A8K and A10K was studied using small angle X-ray scattering (SAXS) and wide angle X-ray scattering (WAXS) that confirms the presence of thin rodlike aggregates with the size of 100 nm having biaxial cross-section [1].

Additionally, local structures leading to the formation of nanotubes from A6K has been investigated using flow aligned X-ray diffraction (XRD) [57]. The work on investigation of structures formed by A6K in water is extended and relevant results and conclusions are published [58].

In taking this work further, investigating structures of the same peptide A6K for another counter-ion and various pH values was performed in the current study. As pH alters the charge of the peptide, different structures were obtained at different pH values. Counter-ion also has a shielding effect on the charges and hence was expected to influence the self-assembly structures. This investigation was important to understand the effect of charge distribution on peptide-peptide interactions.

2.4. APPLICATIONS OF PEPTIDES

Self-assembling features of peptides inspires various applications ranging from nanoelectronics, computational devices, and photonic crystals to biotechnology, biomineralization, targeting drug delivery and tissue engineering scaffolds.

As a point of protein chemistry, soluble proteins displaying a desired function, such as a particular enzymatic activity or binding epitope can be modified at their surfaces to enable self-assembly; the resultant nanostructure contains a factory of sites whose function is dictated by the monomeric precursor. In terms of production, many proteins can be overexpressed and technologies to incorporate non-coded residues facilitate diversity. In spite of these advantages, peptides and proteins have limitations. Devices that must operate in rigorous environments, such as at high temperature, or in strongly acidic and alkaline solutions, may require more robust materials. For electronic applications, limited electrical conductivity is a severe drawback. For applications that necessitate in vivo function, enzymatic degradation may be problematic. However, controlled degradation can be advantageous for tissue engineering applications where extracellular matrix substitutes fabricated from self-assembled peptides or proteins may potentially be degraded at a rate similar to tissue regeneration [28].

3. MATERIALS AND METHODS

3.1. MATERIALS

Table 3.1. Chemicals for cytotoxicity of A10K

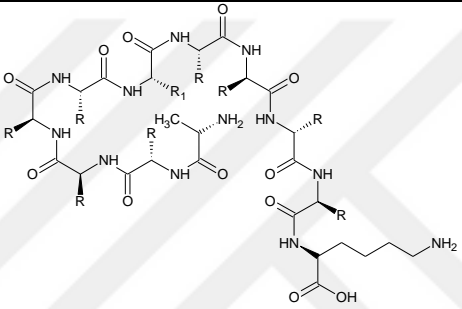
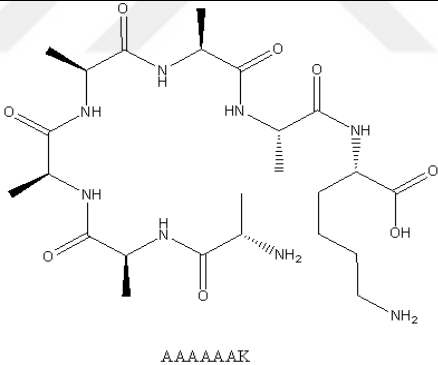
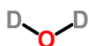
Chemical name	Formula	Structure	Provider	Purity
Peptide Alanine(10)- Lysine(1)	A10K		(CPC Scientific Lot No: CM- 08-012-59	
Peptide Alanine(6)- Lysine(1)	A6K(with Cloride counter- ion)	 AAAAAAK	(CPC Scientific Lot No:	
Heavy Water	D ₂ O		Armar Chemicals	99.8%
Tetrazolium Salt	MTS Reagent Powder	-	CellTiter 96®Aqueous Promega Corporation	

Table 3.2. Cells and solutions used for cytotoxicity of A10K

Cell Type	Abbreviation	Supplier
Human Umbilical Vein Endothelial Cell	HUVEC	ATCC-CRL Virginia, USA
Human Epidermal Keratinocytes	HaCaT	ATCC-CRL Virginia, USA
Kidney Epithelial Cell	Vero	ATCC-CRL Virginia, USA
Leydig Cell (Mus musculus, mouse)	TM3	ATCC-CRL Virginia, USA
Human Dermal Fibroblast	HDF	Isolated from Human Foreskin [59]
Dubleco Eagle's Minimum Essential Medium	DMEM	Gibco

Penicillin-Streptomycin- Amphotericin	Anti-Anti (100X)	Gibco
Fetal bovine serume	FBS	Gibco
Dulbecco's Phosphate Buffered Salt Solution	(DPBS; w/o: Calcium, w/o: Magnesium)	PAN Biotech, GmbH
Dimethyl sulfoxide	DMSO	Sigma-Aldrich, UK

3.2. METHODS

3.2.1. Dynamic Light Scattering (DLS)

Dynamic Light Scattering is a commonly used method which allows the determination of particle size down to 1 nm. This technique is based on the measurement of the distribution of velocity for particle movement in the sample by analyzing dynamic fluctuations of scattering intensity of light caused by the Brownian motion. Hydrodynamic radius which is calculated by Stokes-Einstein equation [60] is obtained from a microscopic point of view, the basic principle supply the illumination of the sample by a laser beam and the fluctuations of the scattered light from the sample are detected at a known scattering angle θ by using a photon detector. Basic working principle of DLS is shown in Figure 3.1. Additionally, a simple representation of the instrument is submitted in Figure 3.2. Size of various systems such as emulsions, proteins, nanoparticles, colloids and peptides can be determined by this method.

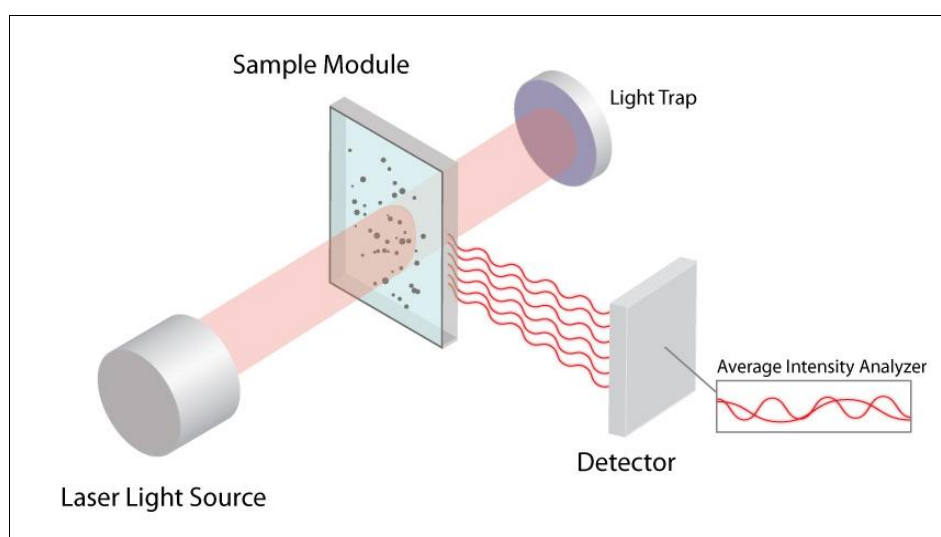


Figure 3.1. Schematic representation of DLS working principle [61]



Figure 3.2. An image of a DLS instrument

In this study, DLS is the instrument used for the measurement of zeta-potential of only medium, medium with FBS and complete medium (FBS, medium and antibiotic) contains peptide that is described in the next section.

3.2.2. Zeta-Potential Analyzer

Zeta potential is one of the indirect measurement techniques to determine the net charge on the surface of the particle by obtaining zeta potential value. This method is widely used due to the feature of most accessible instrument to characterize the superficial properties of the particle in the current media. Hence, analyse of zeta potential can be systematically used as a pre-screening method to check batch to batch stability.

Additionally, the surface charge of the particle is strongly related with the existence of physical state, for instance stability, absorption of proteins and peptides. It also influences the interaction of the particle with biological systems. So, the values of zeta potential are especially remarkable to specify the particles interested for biomedical applications. It can possibly supply information about the tendency of the particles to aggregate in aqueous media to associate the physical-chemical features of the particle in their *in vivo* and *in vitro* operation [62].

3.2.3. Light Microscopy

Light microscopy is one of the imminent research tools in research modern biology and many applications. Since the biological systems contain plenty scales of complexity, light microscopy is used to access information from various biological scales in living cells [63]. Apart from the other microscope techniques it allows, *in vivo* studying or observations in their native hydrated environments. Secondly, it labels the highly specific of multiple components, and lastly allows the determination of the comprehensive internal structures to be imaged in three dimensions. However, its major weakness is its limited resolution, particularly in the axial, or focus, direction. Confocal or computational approaches techniques have improved the system resolution both laterally and axially, but there still are great limitations of resolution for axial direction. Fundamentally, the wavelength of the light limits to the resolving power of optical microscope [64].

The most widely, light microscopy techniques can be classified into two categories; one is brightfield and the other is fluorescence. In brightfield microscopy the detection objective and the source of the light is positioned at the opposite parts of the samples, then the

sample is viewed by the behaviour of the passing light through the sample such as scatters, deflections or absorbance of it. Commonly cells are transparent and slim; they do not tend to absorb much light.

On the other hand, molecules called fluorescent dyes (fluorophores) are utilized in fluorescence microscopy to absorb one wavelength of the light (the excitation wavelength) and emit a second, longer wavelength of it (the emission wavelength). Generally, many molecules in the cell are not naturally fluorescent; therefore the fluorescent markers are introduced to the sample to be imaged. This allows the markers to be targeted to the relevant molecule or molecules, either by genetically encoding a fluorescent protein or by combining a fluorescently marked antibody. Various fluorescent molecules can be employed simultaneously to distinguish and detect at very low abundance of the molecule, making fluorescence microscopy a powerful technique. In fluorescence microscopy epifluorescence is typically used, which the fluorescence excitation light expose the sample through the same objective that is used to reveal emission of the sample [65].

A schematic representation of commonly used light microscopy illustration is submitted at Figure 3.3 while the used light microscopy during the experimental study is shown at Figure 3.4.



Figure 3.3. An image of a Light Microscope

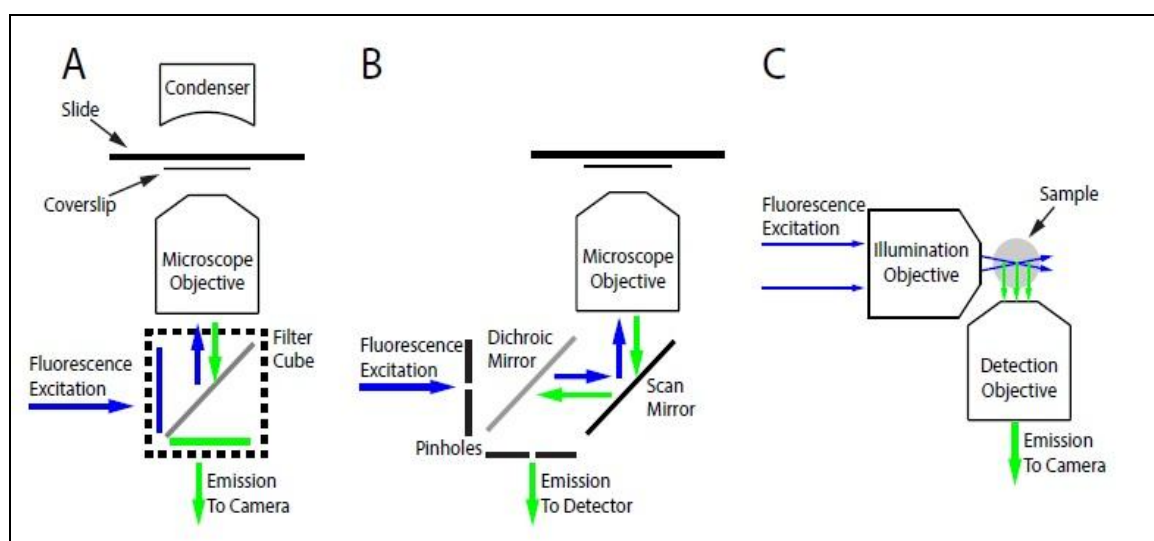


Figure 3.4. Schematic layouts of common microscopy techniques a) An inverted epifluorescence microscope b) A Confocal microscope c) A light sheet microscope [65]

Here, Light Microscopy is utilized to visualize the morphology and the growth of the cells, and monitor the scratch of the cells during the wound healing process that is explained in detail at Chapter V.

3.2.4. Small Angle X-Ray Scattering (SAXS)

X-ray small angle analysis is a universal technique which covers a broad range of particles from very small biological samples to enormous macromolecular ones for studying structural features from 5 kDa up to 100 MDa that is used to indirectly get information about the morphology and size of particles [66]. Any scattering process is characterized by a reciprocity law, which gives an inverse relationship between particle size and scattering angle. Colloidal dimensions (between tens and several thousand \AA) are enormously large compared to the X-ray wavelength [67].

Scattering techniques use radiation as a source of investigation of the unknown sample. Light, X-Ray and Neutron scattering have similar working principles but the interaction of the radiation with the scattering medium is different. For Small Angle X-Ray Scattering, SAXS, radiation is X-Rays and the scattering contrast is the fluctuations of the electron density.

Colloidal interactions, multi-scale structures in soft colloids, polyelectrolyte brushes and the amphiphilic self-assembly occurring at the millisecond time scale are only some examples of what can be measured by SAXS [16, 68]. It gives supplementary information about macromolecular folding, aggregation, extended conformations, macromolecular structures, flexibly linked domains, shape, conformation, and self-assembly in solution, while at the lower resolution range of about 50\AA to 10\AA resolution, but without the size limitations inherent in nuclear magnetic resonance (NMR) and electron microscopy studies [69].

Basically, SAXS set-up consists of four main components. X-Rays is the first part as a source, that are produced in an electron tube by using two electrodes, where one sends electrons at an enormous speed to the other one. The anode is hit by the electrons and during the electronic organization, X-Rays are produced. The other part is a monochromator. Then, the beam of X-Rays is arranged, making the rays as parallel as possible to each other. This monochromatic and arranged X-Ray beam then hits the sample and a small part of the incoming beam is scattered. The last part is the detector to collect information from the scattered light. Vacuum has a great importance to use in a SAXS system to prevent the strong background scattering from air. Additionally a conventional SAXS set up also contains a beam stop that is needed to protect the detector from the primary beam. The diagram of Figure 3.5 represents a brief set up of SAXS system.

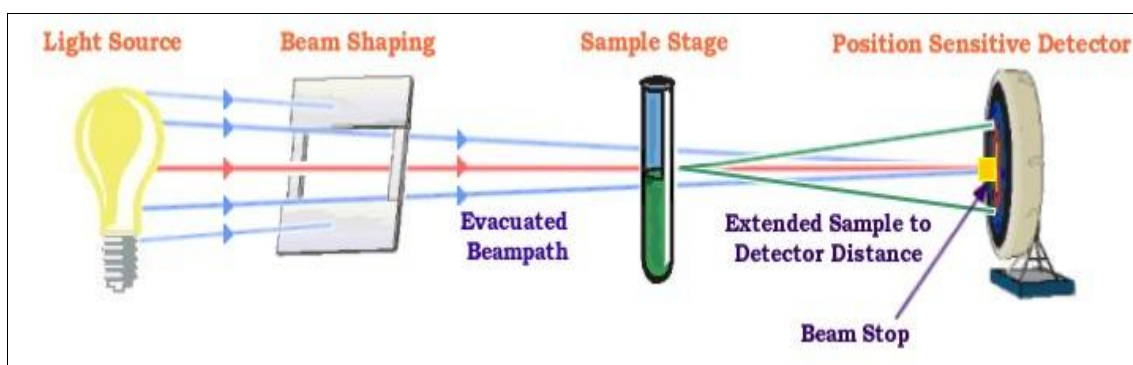


Figure 3.5. Schematic layout of a SAXS setup detecting the incident, scattered and transmitted X-Ray beams and the 2-D detector [16]

As it was previously mentioned, the principle of the SAXS is based on the measurement of the electron density fluctuations. The electric field of the radiation scattered to a point detector at position r , where A_0 is the initial amplitude, has a wave amplitude, A , which has a value of

$$A = A_0 e^{i\vec{k} \cdot \vec{r}} \quad (3.1)$$

if it is a planar wave. k is the wave vector with a value of

$$|\vec{k}| = \frac{2\pi}{\lambda} \quad (3.2)$$

where λ is the wavelength of the incoming planar wave. It has the same direction with light. In SAXS, it is not amplitude, which is being measured. Scattered intensity is measured. The intensity, which is the energy flux, or the number of particles, per time and area, is proportional to the square of the amplitude. Radiation source hits on the detector, “enlightening” a certain area. As one move further away from the source, the illuminated area gets bigger but the intensity decreases.

Area is directly proportional with the square of the distance, r , on the other hand, is inversely proportional to the square of the distance. When these relations are combined, one gets the result that A , amplitude, is inversely proportional to the distance, r . Consider a single scattering center at the origin. The wave comes with amplitude of as stated in equation (3.1) and it is scattered where

$$A_s = A_0 \frac{b}{r} e^{ik_s r} \quad (3.3)$$

Here, b is known as the scattering length, which can be thought as the probability of being scattered. Here it is assumed that the scattering is quasielastic, meaning there is a negligible change in the frequency. A and A_s are assumed to be in phase as well. If there is a phase shift, the scattering center is not placed at the origin, then the scattering amplitude becomes;

$$A_s = A_0 \frac{b}{r} e^{ik_s r} e^{-i\vec{q} \cdot \vec{R}} \quad (3.4)$$

In equation (3.4), there is a vector, q , known as the scattering vector. It is the difference between the scattering vector of the incoming wave and the scattered vector and its value is;

$$q = \frac{4\pi}{\lambda} \sin\left(\frac{\theta}{2}\right) \quad (3.5)$$

If there are N scattering centers, all the scattered waves are summed up.

$$I = \frac{1}{V} \langle b^2 \sum_{i=1}^N \sum_{j=1}^N e^{-i\vec{q} \cdot \vec{r}_{ij}} \rangle \quad (3.6)$$

$$\vec{r}_{ij} \equiv \vec{r}_i - \vec{r}_j \quad (3.7)$$

In this equation, V is the scattering volume. All the scatterings from individual atoms are summed up to get information about the structures we have. Then, here is the basic idea of how imaging and scattering are related:

$$I(\vec{q}) = |A|^2 = \frac{1}{V} \left| \sum_i b e^{i\vec{q} \cdot \vec{r}_i} \right|^2 \quad (3.8)$$

if it is imagined all the atoms are collected in a sphere, then;

$$\frac{1}{V} = \left| \sum_{V_{sphere}} d\vec{r} q(\vec{r}) e^{i\vec{q} \cdot \vec{r}} \right|^2 = \frac{1}{V} P(\vec{q}) \quad (3.9)$$

$P(q)$ is known as the form factor and it gives information about the size and the shape of the structures. Fourier transform of $P(r)$, scattering length density, in equation (3.9) relates scattering and imaging (3.8).

Each characteristic shape has different form factors that supplies varying mathematical models, which allows the predictions of the morphology from the scattering data. In this work, SAXS is used to estimate the formed structures in the samples of varying concentrations for A6K with different counter ions at altering pH values as well as A6K in H_2O .

3.2.5. Cryo-Transmission Electron Microscopy (Cryo-TEM)

Cryo-TEM is one of the most powerful imaging techniques that can be applied to the nano-scale particles, self-assembling structures, geochemical and biological minerals, electrochemical systems or macromolecular conformations [8, 70]. It is also known as cryo-EM, and was developed in the 1980s for visualizing biological samples in a virtually natural state at the resolution of the transmission electron microscope (TEM) (0.1–2 nm). Conventional preparation techniques of TEM contain drying and distaining processes or plastic embedding of the samples, causing the sample that is captured to correspond to a deformed version of the original specimen.

For cryo-TEM the technique basically contains imaging of the sample in a frozen-hydrated state. Sample preparation of Cryo-TEM typically involves the process of putting a droplet of the sample on an electron microscopy (EM) grid, immersing with filter paper to remove excess solvent of the sample, and flash freezing the grid in a cryogen which causes the solvent to compose a vitreous or amorphous, glass-like state. A typically used grid of the system has a hollow carbon support film that allows sample particles to be suspended in a layer of frozen solvent within the support layer's hole. Later on, frozen sample's cryo-TEM images can be picked up without any adsorption interference or background signal from the support layer. This preparation method preserves the sample specimen in the solid state that can be placed into the ultra-high vacuum of a TEM.

Liquid nitrogen is carried on to the frozen sample grid in cryo-TEM during the imaging process. The advantage of the cryo-TEM is that images can be collected from the existing specimen in a frozen-hydrated state that is as it exists in solution.

A schematic representation of a cryo-TEM is shown in Figure 3.6.

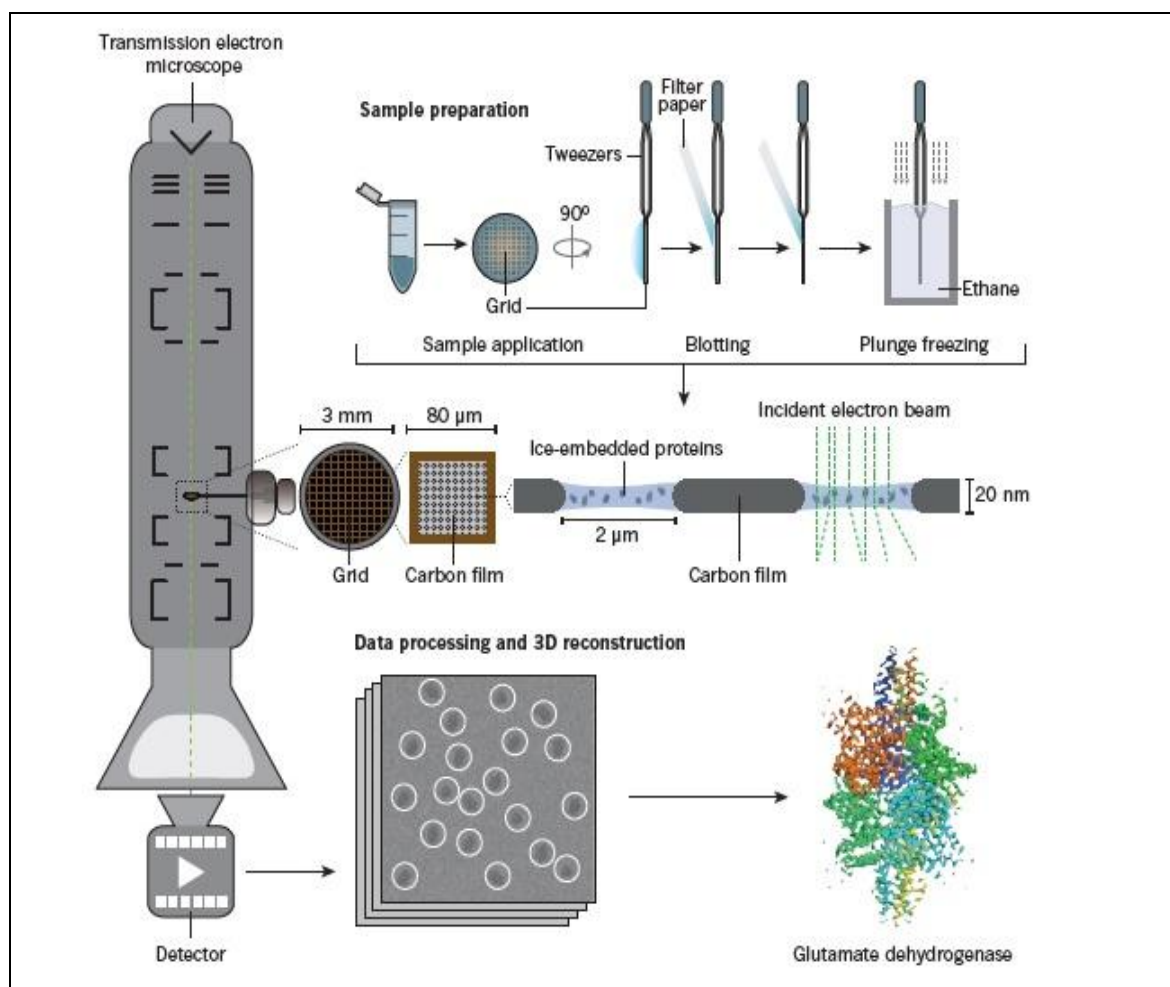


Figure 3.6. Determination of an image of a protein by cryo-TEM that involves several stages [71]

In this study, cryo-TEM is used to obtain actual images of self-assembly structures formed by oligopeptides for A6K and A10K.

3.2.6. Infrared Spectroscopy (IR)

Infrared spectroscopy is one of the major tools in analytical chemistry within instrumental techniques. One of the great advantages of IR is to allow studying almost any samples any state. Among the various attachments and apparatus, IR is capable to work out with liquids, solutions, pastes, powders, films, fibres and wide range of surfaces.

It is commercially available since late 1940s. At the very beginning the system relied on prisms to behave as dispersive elements. Then later on diffraction gratings were introduced to that current instrument. Further improvements brought the most important features in IR with introduction of Fourier-transform spectrometers. In this system an interferometer is used and it employs the well-established mathematical models of Fourier-transformation. Fourier-transform IR (FTIR) spectroscopy has significantly developed the quality of the spectrum of the IR and decreased the analysis time to obtain the data [72].

The image of an FTIR is submitted in Figure 3.7.

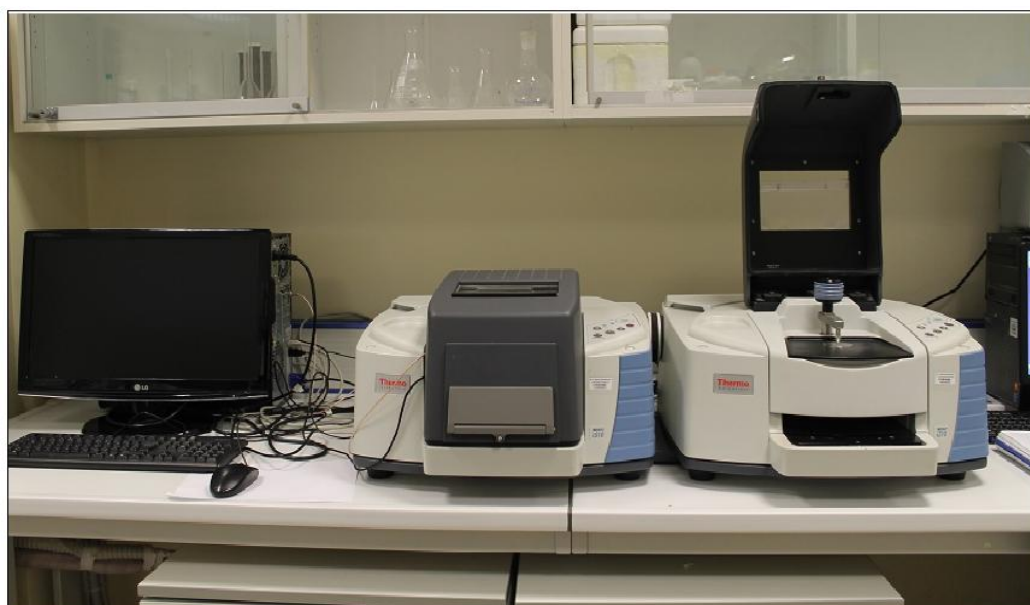


Figure 3.7. An image of an FTIR spectrometer

Since the molecules and compounds are made of atoms that are chemically bonded, there is a movement of these atoms and chemical bonds which are comprised of springs and balls in constant motion. The stretching and bending vibrations of the motion allow understanding the movement. Each particular bond has their own characteristic nature of the frequencies of the vibrations; therefore appear differently on the IR spectrum.

The radiation of IR is generally described as that electromagnetic radiation whose frequency is between 20 and 14,500 cm^{-1} . Chemical compounds absorb IR radiation within this region of the spectrum. This supplies a dipole moment variation during a normal

molecular vibration, molecular rotation, and molecular rotation–vibration or from combinations and differences in the normal molecular vibrations. The IR band's frequencies and intensities produced by a chemical compound specifically characterize that material. Then the IR spectrum of it can be used to identify and quantify the special material in an unknown specimen [73].

Here, FTIR is used to define Amide I bonds of peptide self-assembly structures to gain as complementary results to insight about the second structures formed by peptides.

3.2.7. Ultraviolet-Visible (UV-VIS) Spectroscopy

UV spectroscopy is one of the most commonly found analytical tool within laboratory equipments to investigate absorption or reflectance of the light in 200-800 nm range which is the UV-VIS region of electromagnetic spectrum [74]. It produces plenty of qualitative information for identification of pure substances [75] and quantitative information based on the intensity of the absorbed light.

When radiation comes across with a matter, a number of processes occurs such as reflection, absorption, scattering, photochemical reaction or emission/reemission. It is the absorbance that is measured by the UV-VIS spectrophotometer [76].

Generally, liquid samples are placed in a glass, plastic or quartz cuvettes that possess varying optical properties. Then, the sample in the cuvette is hit by the light and the absorbance of the substance if any is recorded as a spectrum which is a graphical representation of light transmitted or absorbed by material as a function of the wavelength.

UV spectrophotometer that was used in the experimental studies is shown in Figure 3.8.

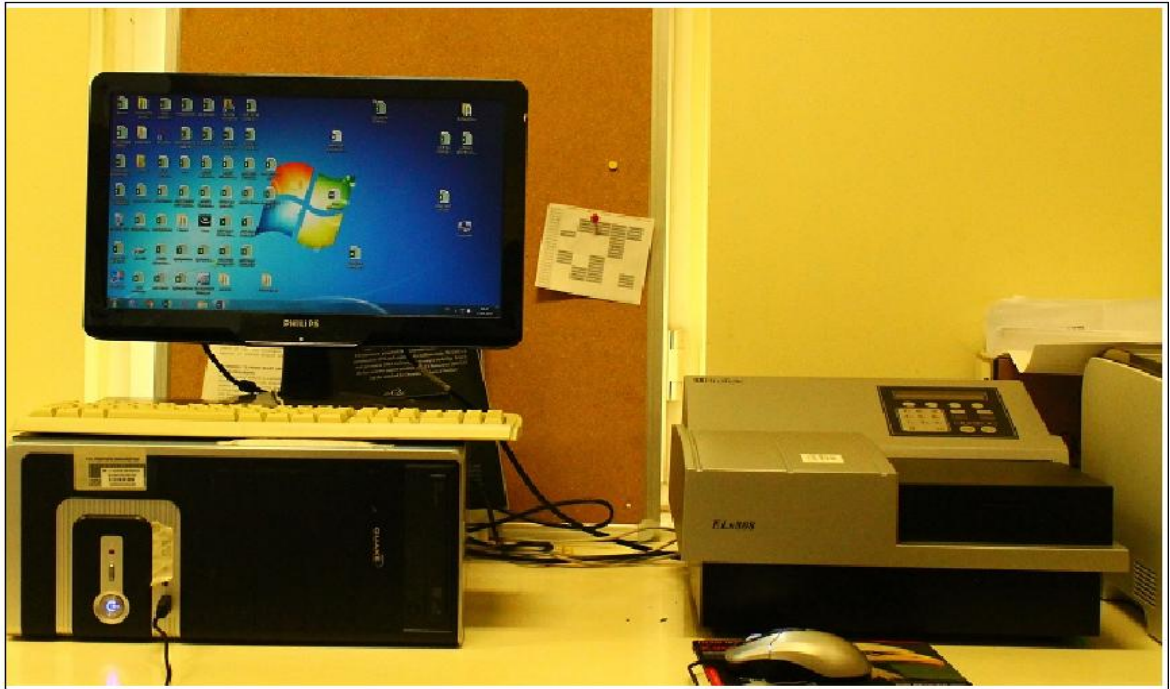


Figure 3.8. An image of a UV-VIS spectrophotometer

UV spectroscopy is used for cell cytotoxicity calculations during the experimental studies, to determine the absorbance of alive or death cells on a certain plate that is described in Section 5.

4. STUDY OF SELF-ASSEMBLY OF PEPTIDES

As previously mentioned, the model peptide (tfa)₂-A₆K revealed some substantial information to former researches [3, 58]. The organization and self-assembling properties of this peptide in aqueous media provides hollow nanotubes at a certain radius (26 nm). Then the coming question was how about if the peptide is inside of a different solvent such as a basic media obtained by NaOH solutions. Moreover, it was wondered what the forming structures are when the peptide has another counter-ion. So, the research was planned to be improved for extensive physicochemical parameters to determine the boundaries of the forming structures and to understand what formed structures are. One of the major features expected to effect the process of the formation is the charge of the monomers, as peptides in the system are pH dependent.

In this chapter, the peptide of (tfa)₂-A₆K was investigated by solubilizing it in a different solvent obtained by varying concentrations of NaOH (0.01M, 0.1 M, 0.2M, 0.5M and 1M NaOH). There are turbidity and pH measurement results of (tfa)₂-A₆K in H₂O in comparison with the same peptide in H₂O and D₂O. The self-assembly structures formed by the peptide under these physical conditions were analysed by SAXS, along with structures formed by another salt form, (Cl)₂-A₆K.

4.1. PREPARATION OF PEPTIDE SOLUTIONS

For the experimental studies the peptide A₆K (97 per cent purity) with TFA counter-ion, and peptide with chloride counter-ion (Cl)₂-A₆K was purchased from CPC Scientific, Inc. and used without further purification. Chloride salt will be referred to as (Cl)₂-A₆K and tfa as counter-ion will be referred as (tfa)₂-A₆K, Other peptide which was used for longer Alanine residue in the study (Chapter V) is represented as A₁₀K (CPC Scientific, Inc.). Heavy water, D₂O (99.8 per cent isotopic purity), was obtained from Armar Chemicals.

The self-assembly behavior of (tfa)₂-A₆K in D₂O has been investigated [16] in detail.

For the determination of the behaviour of peptide (tfa)₂-A₆K in H₂O, various concentrations of the samples were prepared and the solutions concentrations were 8 per

cent, 10 per cent, 12 per cent and 14 per cent (tfa)₂-A₆K, respectively. H₂O was used since it is expected to form the nanotubes for the samples at higher critical aggregation concentration due to stronger hydrogen bonding interactions of H₂O.

One of the physical properties that can possibly have an influence on the formation of self-assembly is pH. Therefore, we aimed to investigate the behaviour of (tfa)₂-A₆K samples at different pH values. Various NaOH solutions were prepared at certain molarity which shows the relevant pH values measured by micro-probe pH-meter. So, 8 per cent, 10 per cent, 12 per cent and 14 per cent (tfa)₂-A₆K were prepared in 0.01M, 0.1 M, 0.2M, 0.5M and 1M NaOH (in H₂O).

Moreover, peptide (Cl)₂-A₆K, was prepared in D₂O for the concentrations of 10 per cent, 12 per cent, 14 per cent and 16 per cent to explore the effect of counter-ion on the self-assembly structures.

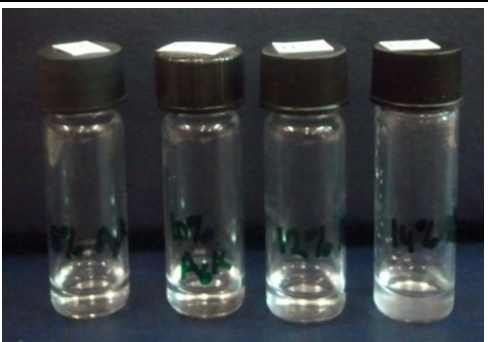
4.2. INVESTIGATION OF (TFA)₂-A₆K IN H₂O AND VARYING CONCENTRATIONS OF NAOH

4.2.1. Physical Properties

As long as A₆K undergoes to self-assemble into nanotubes, it has critical importance to determine the boundaries of this formation. Bearing this in mind, prepared solutions of different concentration for (tfa)₂-A₆K and the related images, turbidity and pH values are submitted in Table 4.1 and described as A₆K shortly.

Table 4.1. Properties and image of (tfa)₂-A₆K peptide, in H₂O

Sample	pH	Net Charge	Turbidity
8 % A ₆ K	2.18	1.7	Clear
10 % A ₆ K	2.15	1.7	Clear
12 % A ₆ K	2.08	1.7	Clear
14 % A ₆ K	1.98	1.8	Slight turbidity



It should be noted that these results are very similar with those obtained for $(\text{tfa})_2\text{-A6K}$ in D_2O in previous work [3].

How altering pH in other words changing the concentration of NaOH affects the physical properties; turbidity and pH of the solutions were investigated. The results of $(\text{tfa})_2\text{-A6K}$ in different molarity of NaOH is represented at Table 4.2-4.6 which is referred as A6K. It is clearly seen that $(\text{tfa})_2\text{-A6K}$ in NaOH solutions have higher viscosities than those prepared in water, some are already gels. Moreover, some solutions are birefringent, as observed under polarized light, suggesting presence of a nematic phase.

Table 4.2. $(\text{tfa})_2\text{-A6K}$ in 0.01 M NaOH, in water

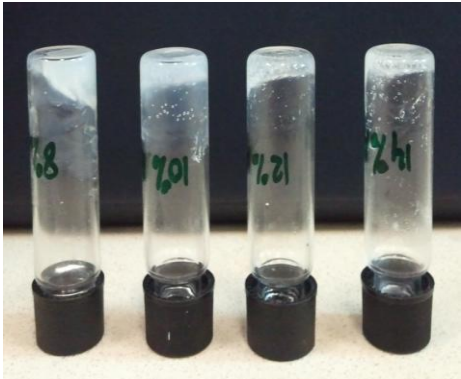
Sample	pH	Net Charge	Turbidity
8 % A6K	2.54	1.5	Clear
10 % A6K	2.65	1.5	Slight turbidity
12 % A6K	2.56	1.5	Slightly more turbid
14 % A6K	2.55	1.5	Slightly more turbid

Table 4.3. $(\text{tfa})_2\text{-A6K}$ in 0.1 M NaOH, in water

Sample	pH	Net Charge	Turbidity
8 % A6K	4.07	1	Clear gel
10 % A6K	3.88	1	Turbid gel
12 % A6K	3.60	1-1.5	Turbid gel
14 % A6K	3.34	1-1.5	Turbid gel

Table 4.4. (tfa)₂-A6K in 0.2 M NaOH, in water

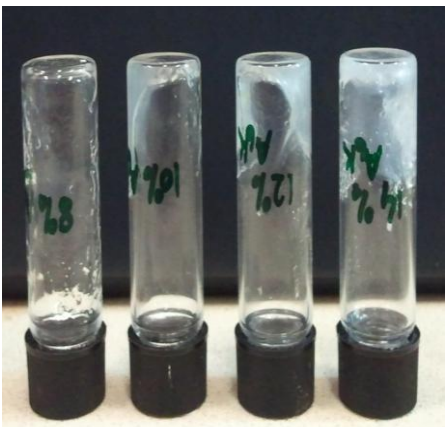
Sample	pH	Net Charge	Turbidity
8 % A6K	8.75	1	Turbid gel
10 % A6K	6.83	1	Turbid gel
12 % A6K	N/A		Turbid gel
14 % A6K	N/A		Turbid gel


Table 4.5. (tfa)₂-A6K in 0.5 M NaOH, in water

Sample	pH	Net Charge	Turbidity
8 % A6K	12.34	-1	Fluid, not turbid
10 % A6K	12.59	-1	Gel like slightly turbid
12 % A6K	12.19	-1	Gel turbid
14 % A6K	N/A		Gel turbid/paste

Table 4.6. (tfa)₂-A6K in 1 M NaOH, in water

Sample	pH	Net Charge	Turbidity
8 % A6K	13.08	-1	Slightly turbid gel
10 % A6K	13.09	-1	Turbid gel
12 % A6K	13.07	-1	Turbid gel
14 % A6K	13.01	-1	Turbid gel



The physical comparison of the solutions for increasing NaOH molarity for A6K is submitted in Figure 4.1.

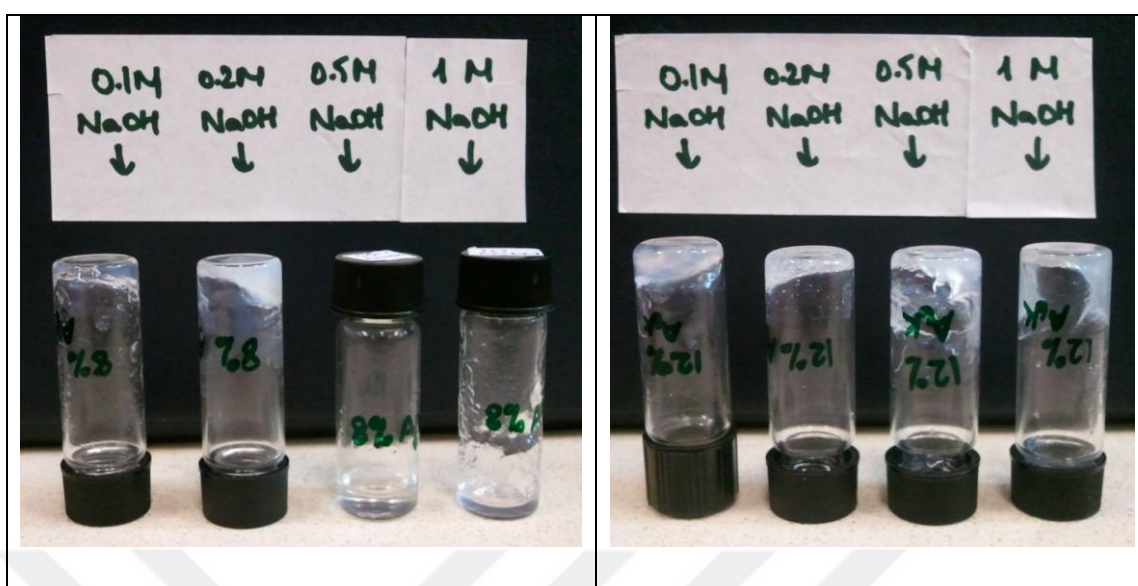


Figure 4.1. Images of 8 per cent and 12 per cent $(tfa)_2$ -A6K peptide at various NaOH concentrations

It is clearly seen from the figures, when the concentration of the NaOH increases which is consistent with increasing pH, the samples turn into gel-like phase at more narrow concentration level of peptides. Figure 4.1 describes the turbidity for the concentration of 8 per cent and when the pH increases up to approximately 12, solution becomes more fluidic rather than gel-like appearance. If the concentration of the peptide is 12 per cent, peptides are turbid-gel even for 0.1 M NaOH.

In the point of charge distribution, peptide has positive total charge ($\sim +2$) at low pH which is obtained when placed in H_2O and -1 at high pH, due to deprotonation of both the C and N ends. This means that the peptide's charge is distributed from positive to negative the variation of pH. It is clearly seen that the electrostatic forces play an important role in the self-assembly behavior of these peptides which is worthy of further investigation.

4.2.2. Self-Assembly Behavior by SAXS Studies

SAXS experiments of this study were performed in MAX-lab, Lund, Sweden. MAX-lab is a national laboratory operated jointly by the Swedish Research Council and Lund University. There are three electron storage rings (MAX I, MAX II and MAX III) and one

electron preaccelerator, MAX injector, which delivers electrons to the storage rings. All three storage rings produce synchrotron light used for experiments. Beamline 1711 at MAX II was used for SAXS experiments. It utilizes a 13-period, 1.8 T, multipole-wiggler utilized to operate in the 0.85 (14.6 keV) to 1.55 Å (8.0 keV) region. The beamline has a single crystal monochromator which provide a high photon flux at the sample while sacrificing easy tenability and high energy resolution.

The exposure was 300 s in every experiment. After subtracting the dark current, each scattering curve was normalised to incident beam intensity, transmission and exposure time. Water was measured in a capillary and subtracted from the measurements which were also performed in capillaries. The measurements which were performed using cells with mica windows were background-corrected by subtracting the mica windows only since the mica cells could not be filled with water.

The behaviour of peptide (tfa)₂-A₆K in H₂O, or various concentrations of NaOH prepared in H₂O was investigated by using SAXS. The scattering curves listed in Table 4.10 were fitted with the form factor of a parallelepiped (a “brick stone”), the form factor of a cylinder with a circular cross section and the form factor of a cylinder with an elliptical cross section. The latter two form factors were factorised according to $I_{\text{model}(q)} = S \cdot P^*_{(q)} \cdot P_{\text{CS}(q)}$.

$P^*_{(q)}$ is the form factor of infinitely thin rod and $P_{\text{CS}(q)}$ is the form factor of the cross section [77].

The fitting routine minimizes the χ^2 -function

$$\chi^2 = \sum_k^N \left(\frac{I_{\text{experiment}}(q_k) - I_{\text{model}}(q_k)}{\sigma(I_{\text{experiment}}(q_k))} \right)^2 \quad (4.1)$$

The longest dimension was kept constant at a value of $C = 400$ nm (that’s the C-edge of the brick stone) or at $L = 400$ nm (L being the length of the circular or the elliptical cylinder). The fit parameters are a constant factor, S, to shift the model curve along the ordinate for all models, the edges A and B in case of the parallelepiped form factor, the cross section radii R_1 and R_2 in case of elliptical cylinder and the cross section radius R in case of the circular cylinder. The background was assumed to be q-independent (an additive constant).

Each scattering curve was analysed with these 3 models, with 5 different initial values of the cross section size to minimize the χ^2 -function for each model.

In the case where the circular cylinder model was used, 5 different initial values for the cross section radius R were applied for the fitting routine. In the case of the other 2 models, the initial values for the edge length A or the cross section radius R_1 were kept constant and the initial values for the edge length B or the cross section radius R_2 were varied. Moreover, the Guinier approximation, the Gaussian chain model and the sphere model were tried as a q -dependent background, with a proper weight factor. To estimate the background, the intensities of the last 20 q values were averaged (q -range from 3.35 nm^{-1} to 3.48 nm^{-1}) and used as the initial value. The result for the fitted background was restricted to be within ± 5 per cent of this average value.

The data of SAXS for the samples of $(\text{tfa})_2\text{-A6K}$ at varying pH are listed in Figure 4.2-4.14.

The best model fit to the scattering curves from 14 per cent $(\text{tfa})_2\text{-A6K}$ in 0.01 M NaOH is achieved with the elliptical cylinder. Still, this model fails to reproduce the slight oscillations between $q = 0.1 \text{ nm}^{-1}$ and $q = 0.3 \text{ nm}^{-1}$.

In the case of 14 per cent $(\text{tfa})_2\text{-A6K}$ in 0.1 M NaOH, the cylinder with elliptical cross section fits the scattering data best.

The best fit to the experimental data in the case of 14 per cent $(\text{tfa})_2\text{-A6K}$ in 0.2 M NaOH is the cylinder with the circular cross section. Interestingly, the parallelepiped model and the elliptical cylinder model both fail to describe the scattering curve because the model fits do not result in similar cross section dimensions A and B or R_1 and R_2 , respectively.

The scattering curves from 14 per cent $(\text{tfa})_2\text{-A6K}$ in 0.5 M NaOH can be fitted best with the elliptical cylinder. The model fits with the parallelepiped form factor give cross section dimensions of $A = 2.6 \text{ nm}$ and $B = 8.6 \text{ nm}$, independent of the initial values of A and B . The model fits with the circular cylinder give a cross section dimension of $R = 1.8 \text{ nm}$ independent of the initial value for A . In the case of the elliptical cylinder, the fit result depends on the initial values of R_1 and R_2 . Figure 4.2-4.5 describes the results.

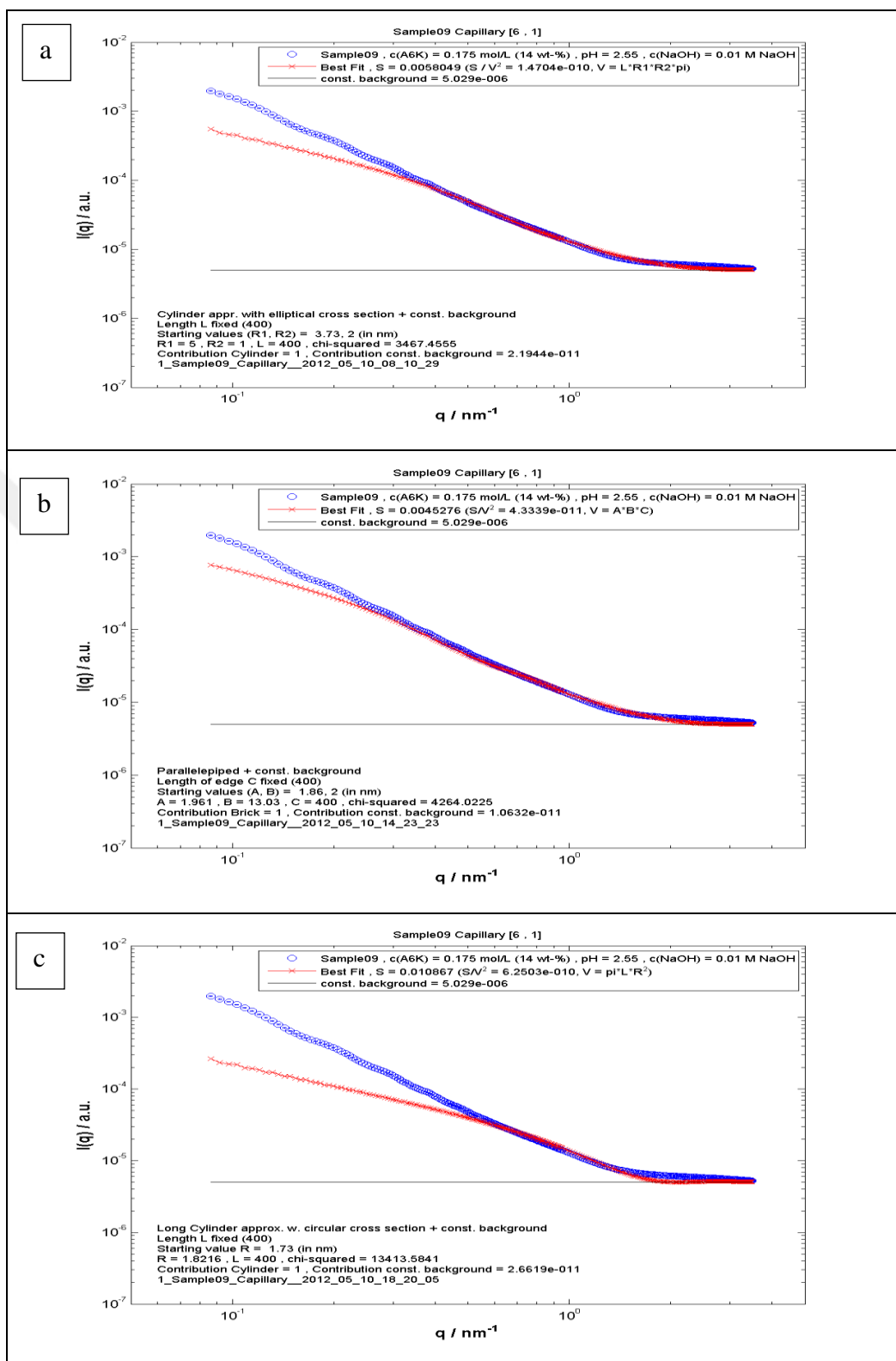


Figure 4.2. 14 Per cent (tfa)₂-A6K in 0.01 M NaOH for varying models a) Sample fitted with the elliptical cylinder model b) Sample fitted with the parallelepiped model c) Sample fitted with the circular cylinder model

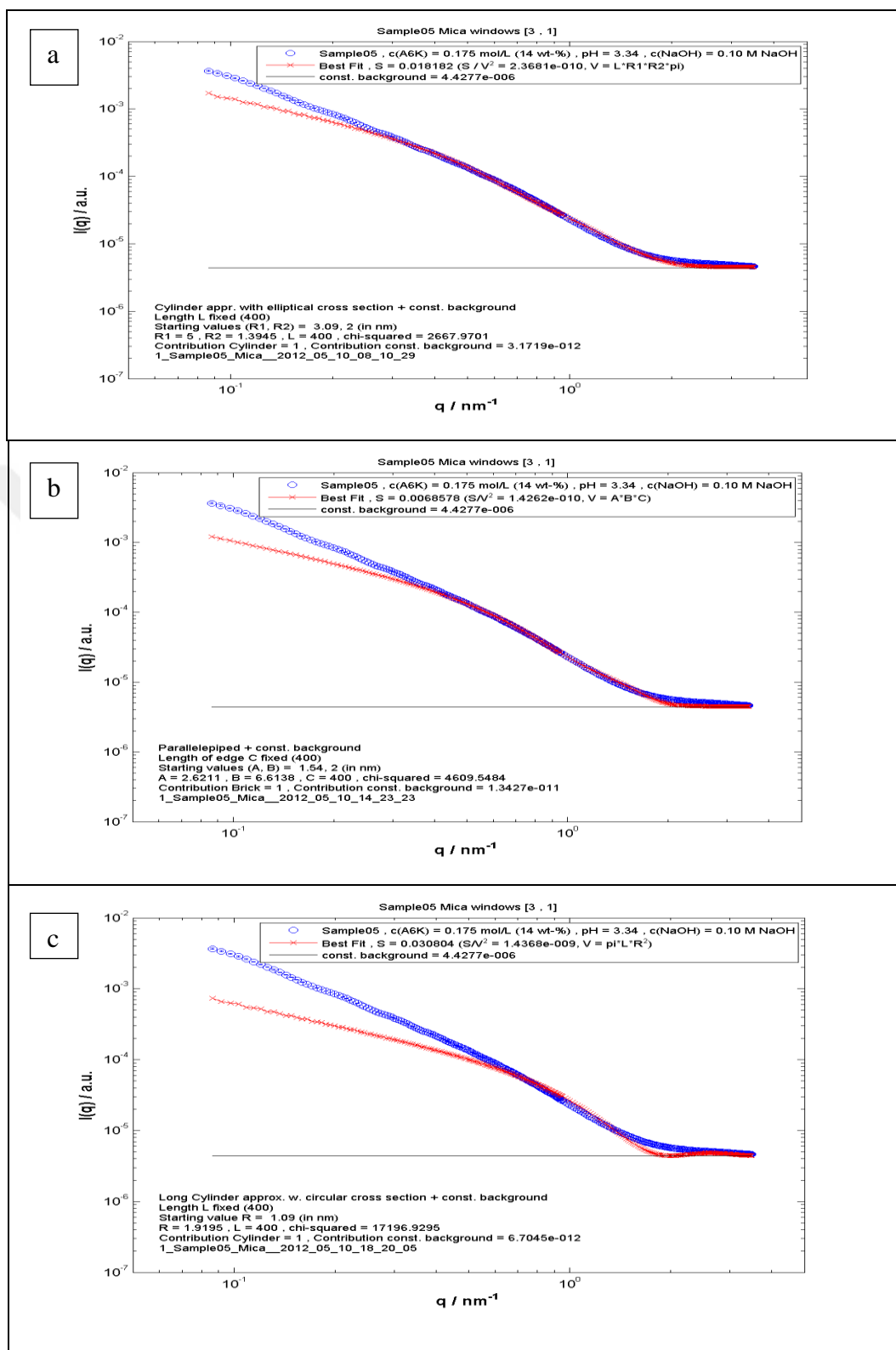


Figure 4.3. 14 Per cent (tfa)₂-A6K in 0.1 M NaOH for varying models a) Elliptical cylinder model $R_1/R_2=5.0/1.4 = 3.6$ or $(D_1/D_2 = 10.0/2.8)$ b) Parallelepiped model $A/B=6.6/2.6=2.5$ c) Circular cylinder model

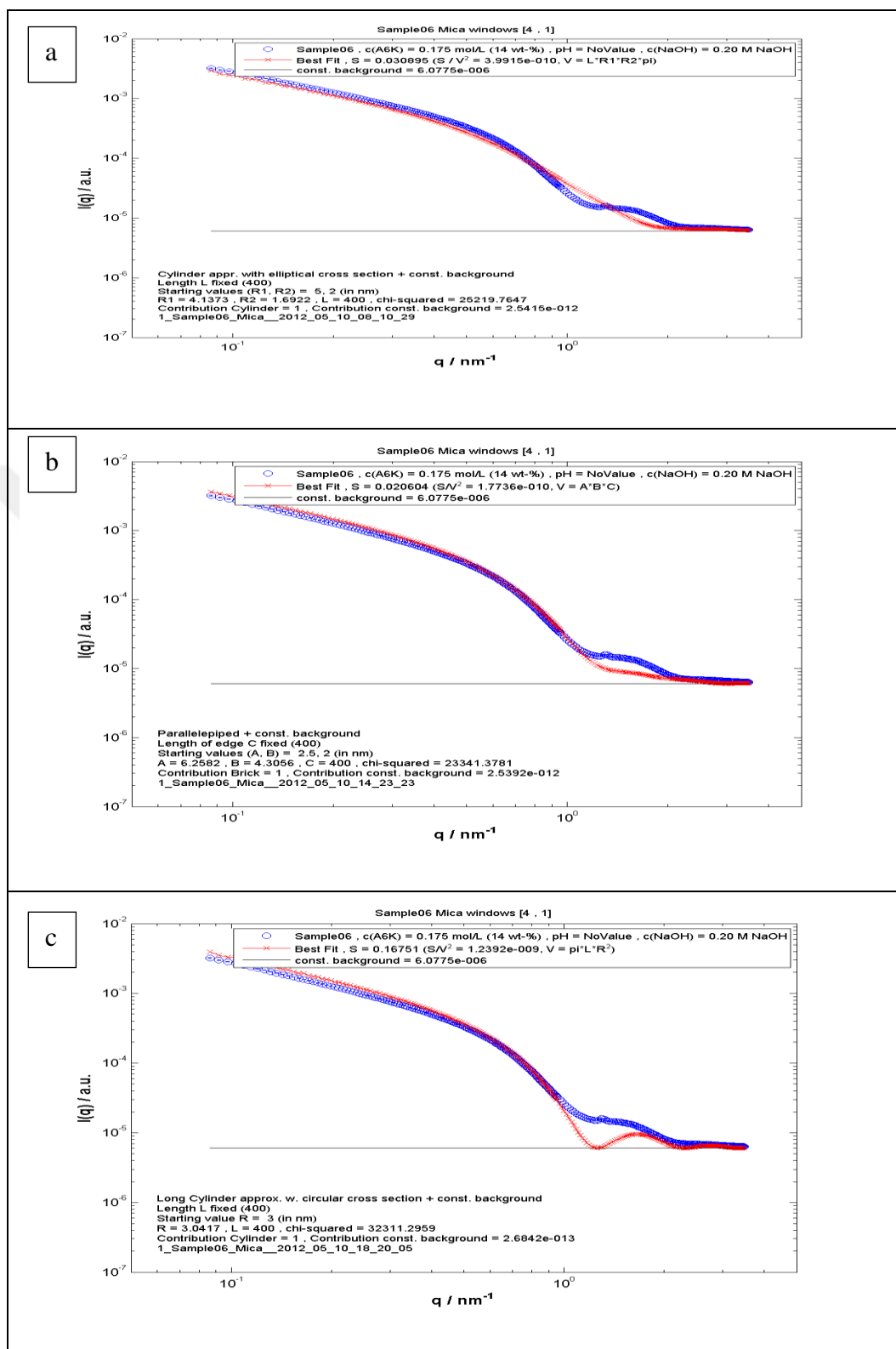
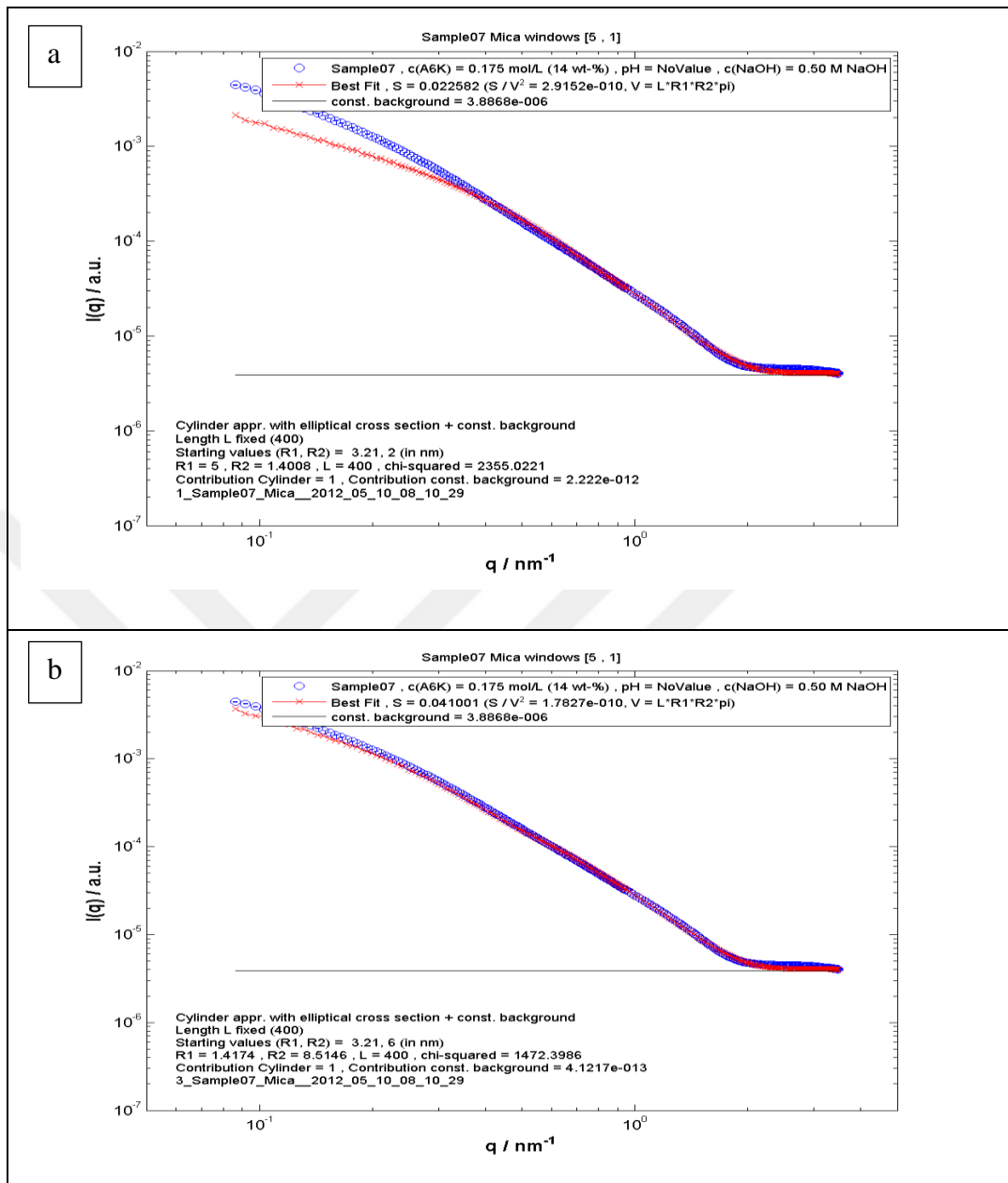


Figure 4.4. 14 Per cent (tfa)₂-A6K in 0.2 M NaOH for varying models a) Elliptical cylinder model $R_1/R_2 = 4.1/1.7 = 2.4$ or $(D_1/D_2 = 4.2/3.4)$ b) Parallelepiped model $A/B = 6.3/4.3 = 1.5$ c) Circular cylinder model



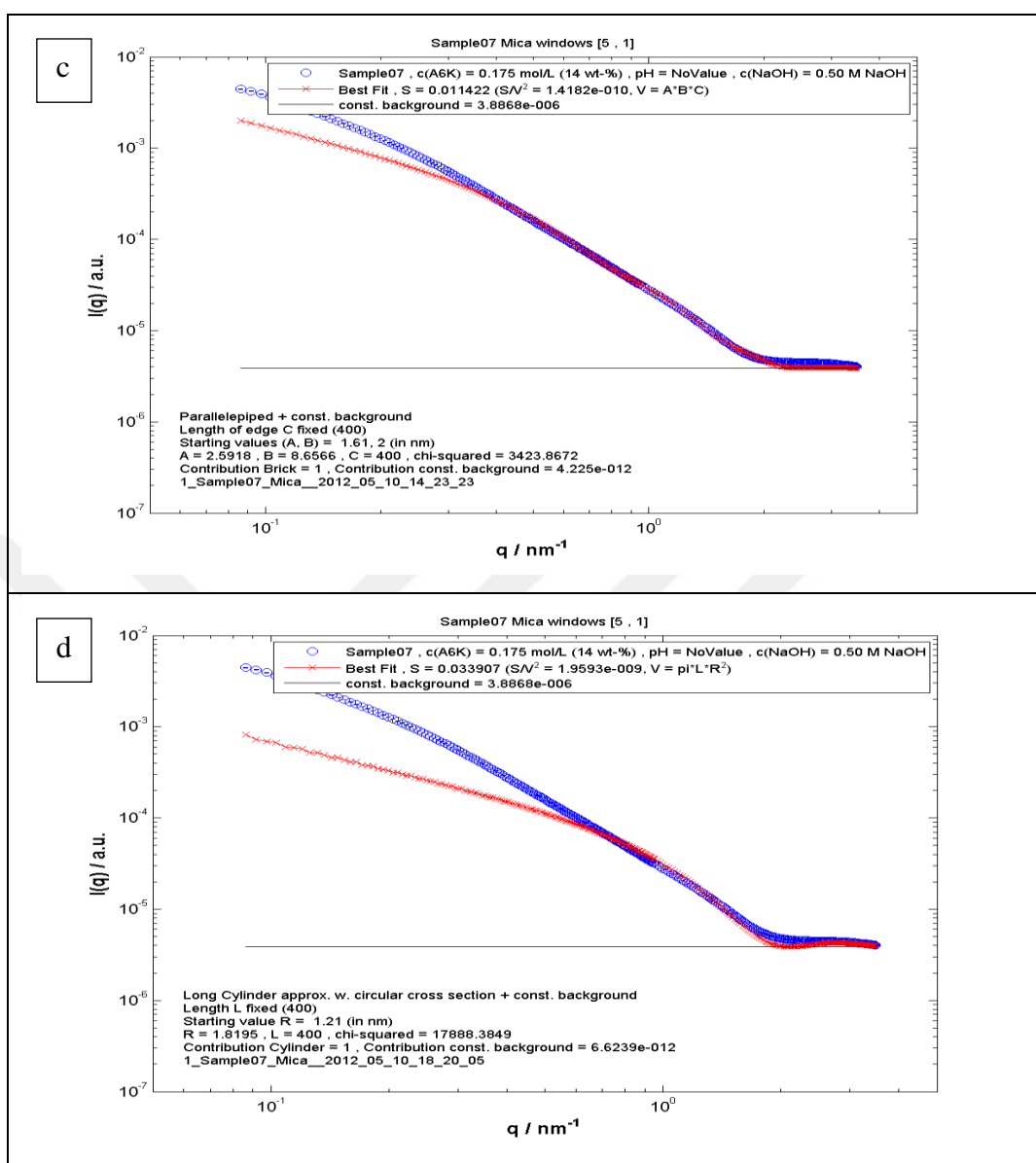
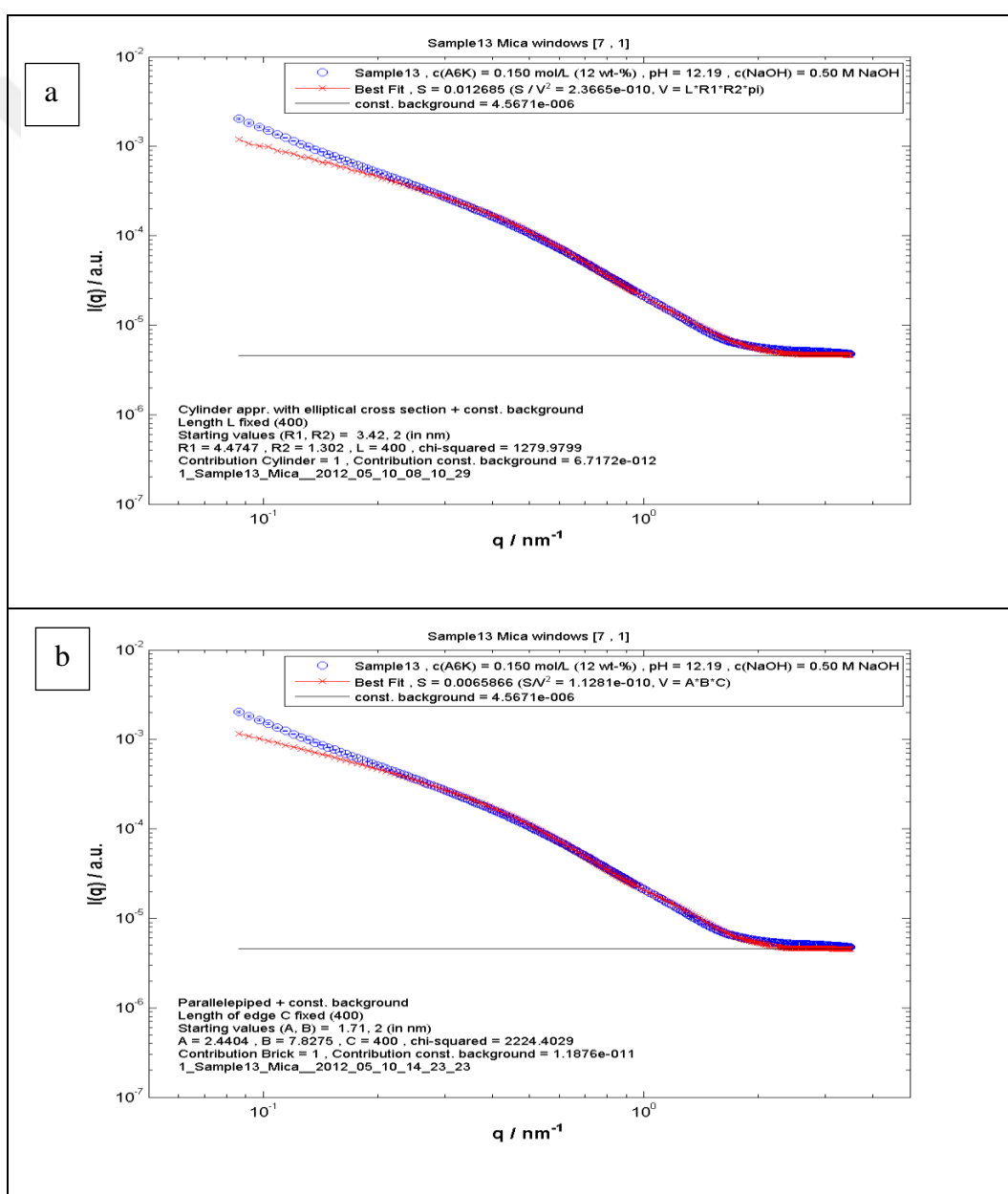


Figure 4.5. 14 Per cent (tfa)₂-A6K in 0.5 M NaOH for varying models a) Elliptical cylinder model ($D_1/D_2 = 10.0/2.8$) b) Elliptical cylinder model but with a different initial value for R_2 . $R_1/R_2 = 8.5/1.4 = 6.1$ ($D_1/D_2 = 17.0/2.8$) c) Parallelepiped model $A/B = 8.7/2.6 = 3.3$
 d) Circular cylinder model

In the case of 12 per cent (tfa)₂-A6K in 0.5 M NaOH the best model fit is achieved with the elliptical cylinder model. The model curve deviates from the experimental data only at q values $q < 0.2 \text{ nm}^{-1}$.

There is not a distinct guideline to determine which model provides the best description of 10 per cent (tfa)₂-A6K in 0.1 M NaOH. The parallelepiped and the elliptical cylinder model have smaller χ^2 values but the circular cylinder model provides a better description of the slope between $q = 0.6 \text{ nm}^{-1}$ and $q = 1 \text{ nm}^{-1}$.

This can also be applied to 8 per cent (tfa)₂-A6K in 0.1 M NaOH. The related results are submitted in Figure 4.6-4.8.



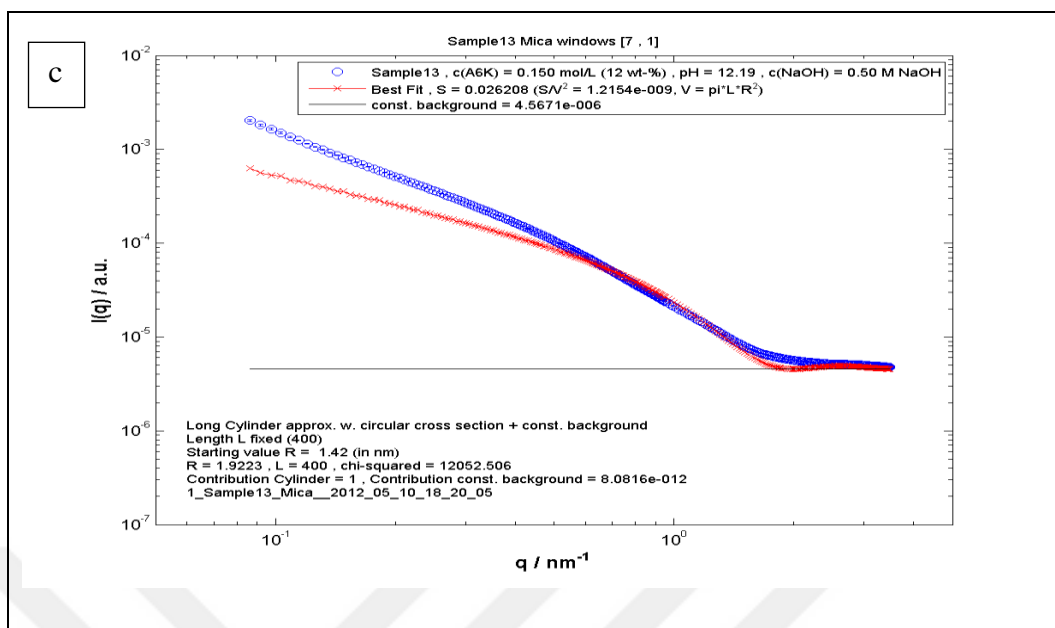
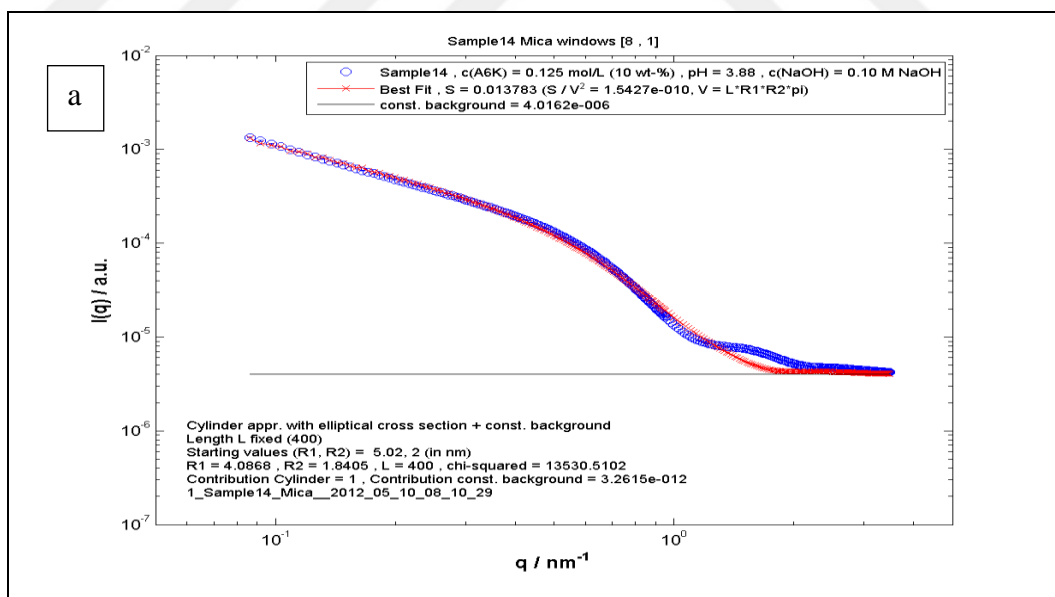


Figure 4.6.12 Per cent (tfa)₂-A6K in 0.5 M NaOH for varying models a) Elliptical cylinder model $R_1/R_2 = 4.5/1.3 = 3.5$ ($D_1/D_2 = 9.0/2.6$) b) Parallelepiped model $A/B = 7.8/2.4 = 3.3$
 c) Circular cylinder model



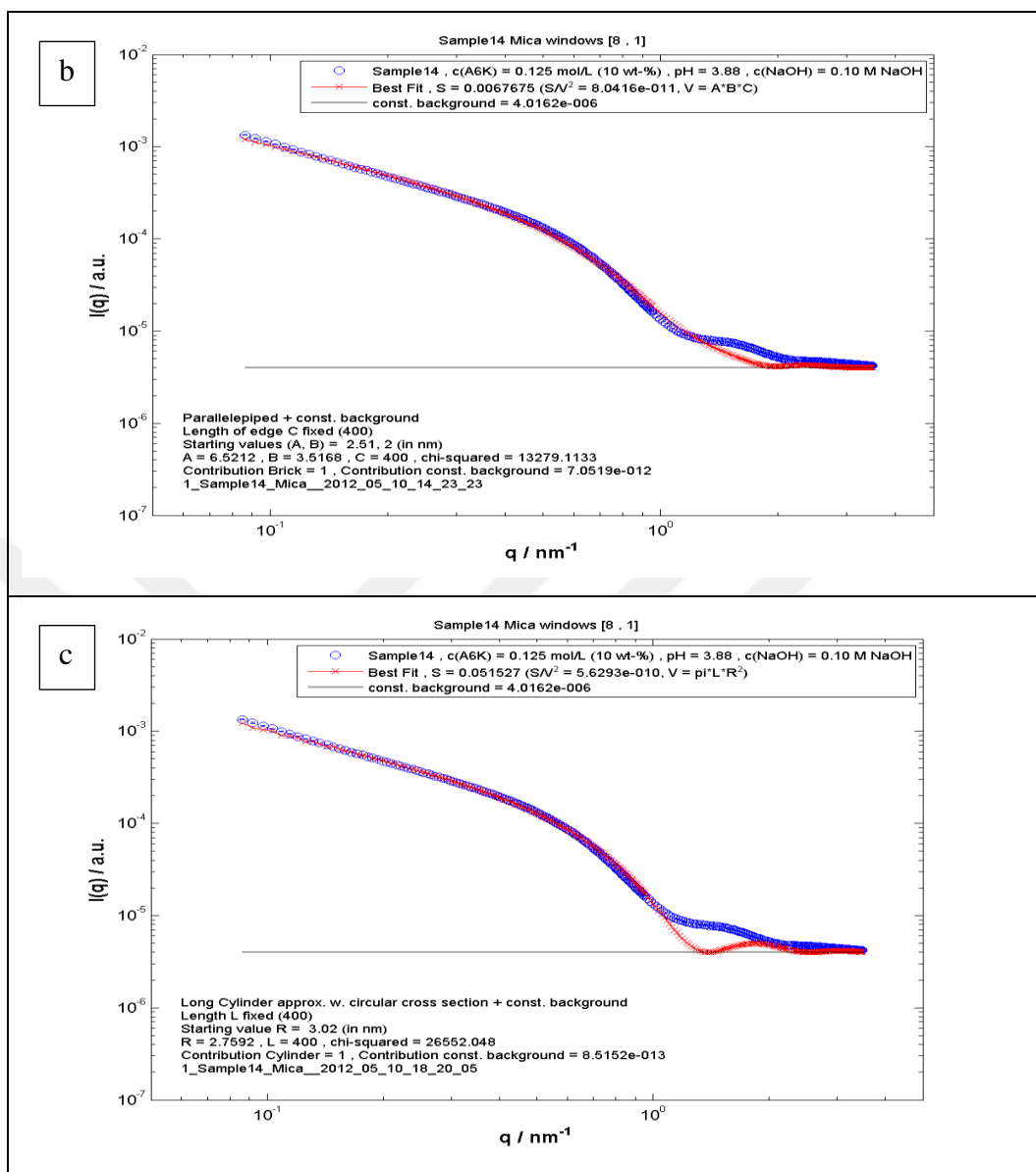


Figure 4.7. 10 Per cent (tfa)₂-A6K in 0.1 M NaOH for varying models a) Elliptical cylinder model $R_1/R_2 = 4.1/1.8 = 2.3$ ($D_1/D_2 = 8.2/3.6$) b) Parallelepiped model $A/B = 6.5/3.5 = 1.9$
 c) Circular cylinder model

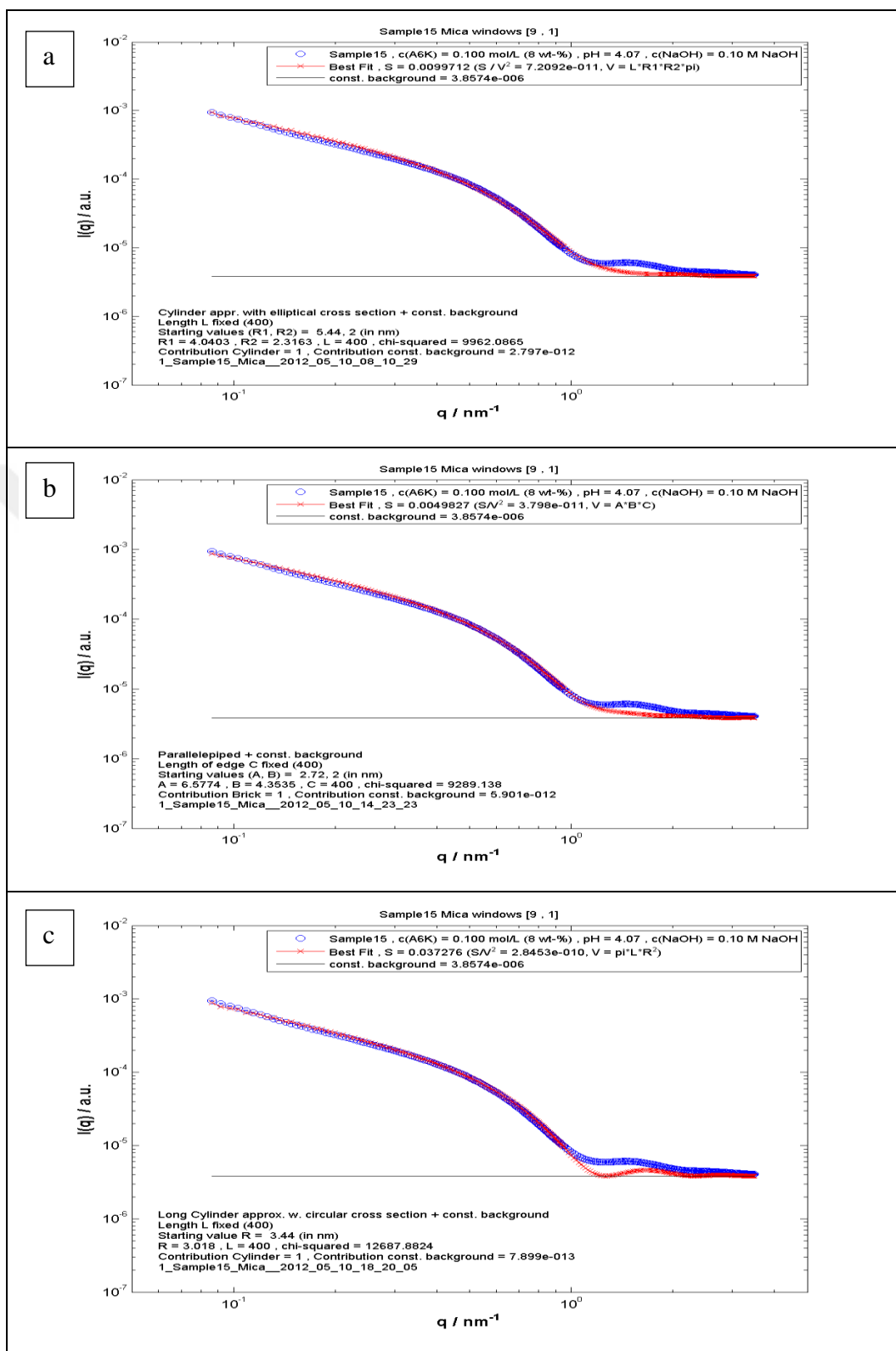
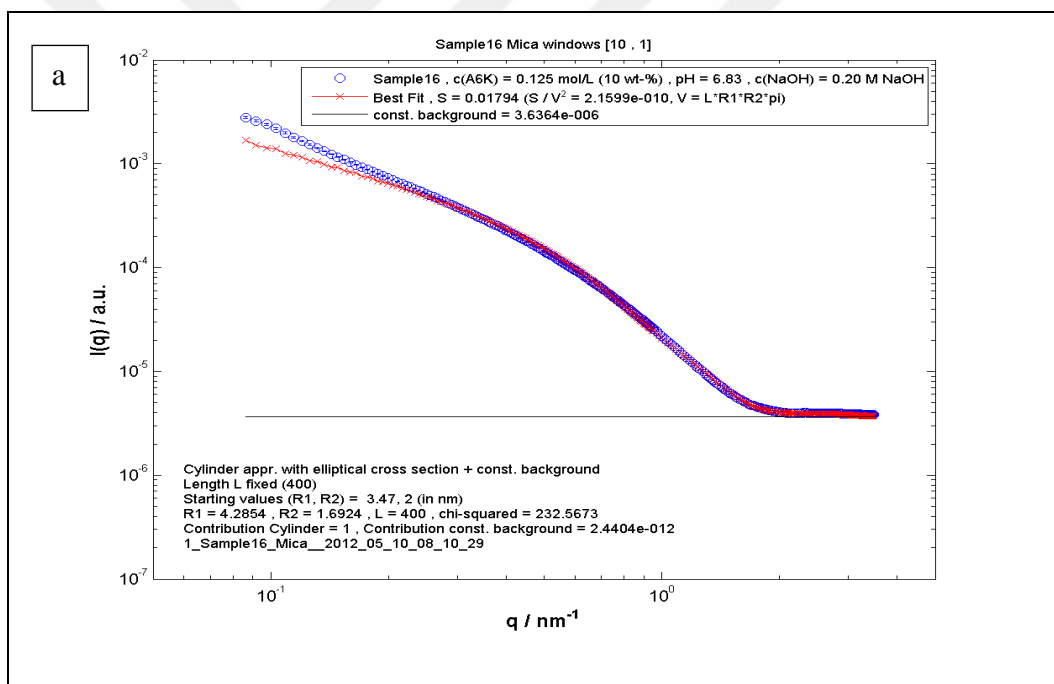


Figure 4.8. 8 Per cent (tfa)₂-A6K in 0.1 M NaOH for varying models a) Elliptical cylinder model $R_1/R_2 = 4.0/2.3 = 1.7$ ($D_1/D_2 = 8.0/2.6$) b) Parallelepiped model $A/B = 6.6/4.3 = 1.5$ c) Circular cylinder model

The best model fit for 10 per cent (tfa)₂-A6K in 0.2 M NaOH is achieved with the elliptical cylinder.

None of the three models is suitable to fit 16 per cent (tfa)₂-A6K in 0.01 M NaOH. Therefore, it involves similar discussion for 14 per cent (tfa)₂-A6K in D₂O which is going to be explained further section.

The elliptical cylinder provides the model fit for 6 per cent (tfa)₂-A6K in 0.2 M NaOH. The circular cylinder model does not reproduce the steep slope of the experimental scattering data between $q = 0.1 \text{ nm}^{-1}$ and $q = 0.5 \text{ nm}^{-1}$. Figure 4.9-4.11 give the results here below.



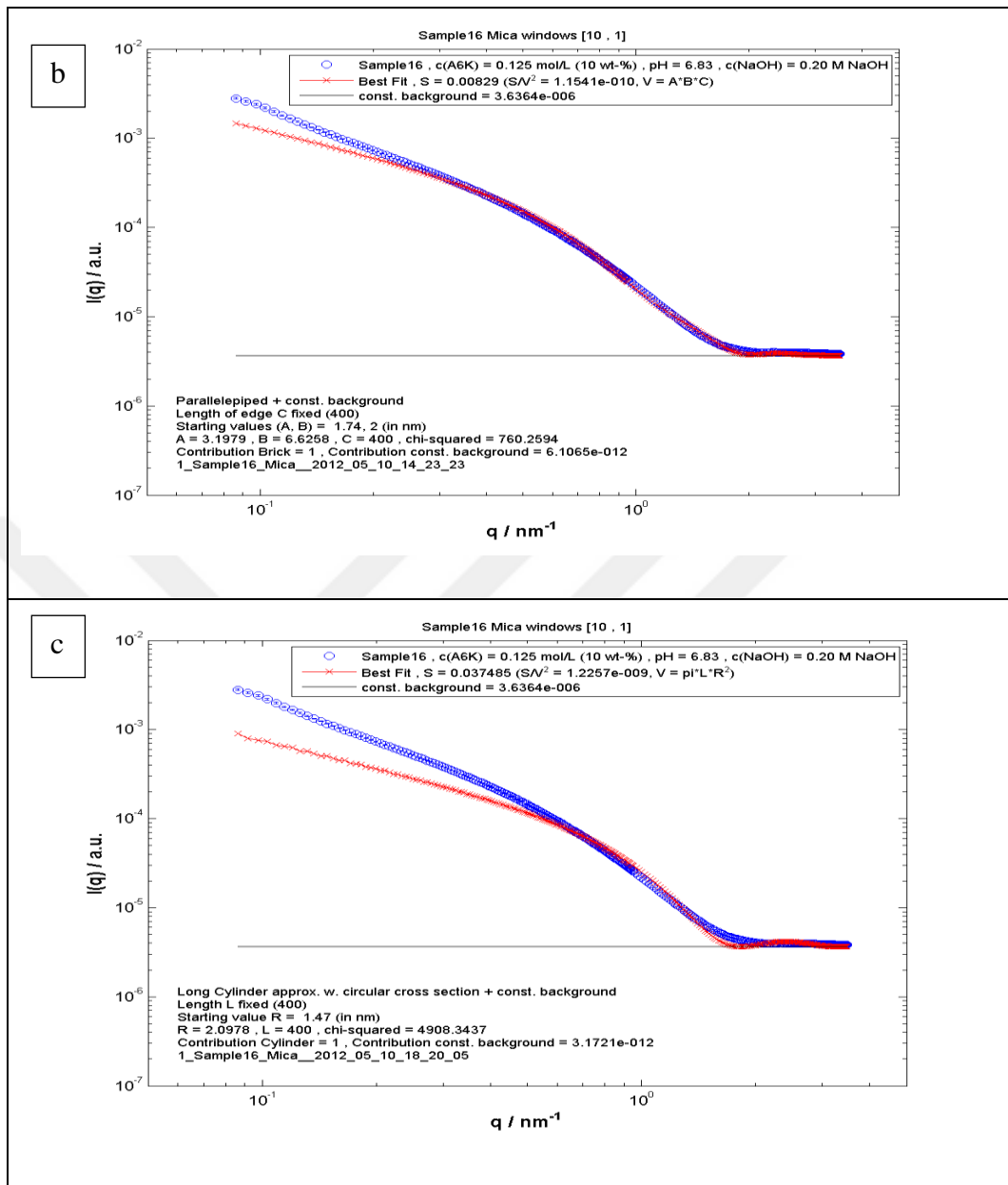


Figure 4.9.10 Per cent (tfa)₂-A6K in 0.2 M NaOH for varying models a) Elliptical cylinder model $R_1/R_2 = 4.3/1.7 = 2.5$ ($D_1/D_2 = 8.6/3.4$) b) Parallelepiped model $A/B = 6.6/3.2 = 2.1$
 c) Circular cylinder model

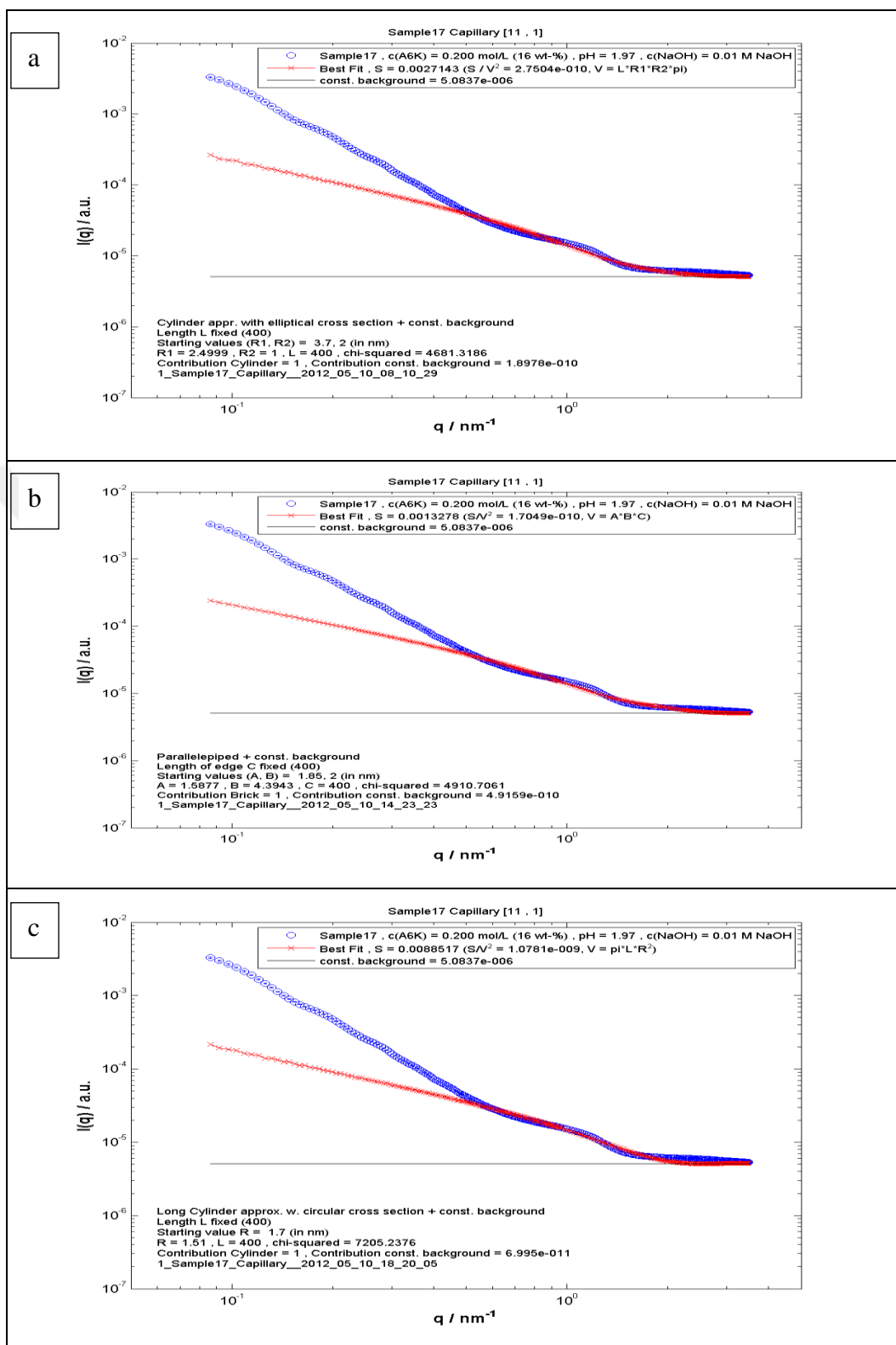


Figure 4.10. 16 Per cent (tfa)₂-A6K in 0.01 M NaOH for varying models a) Elliptical cylinder model b) Parallelepiped model c) Circular cylinder model

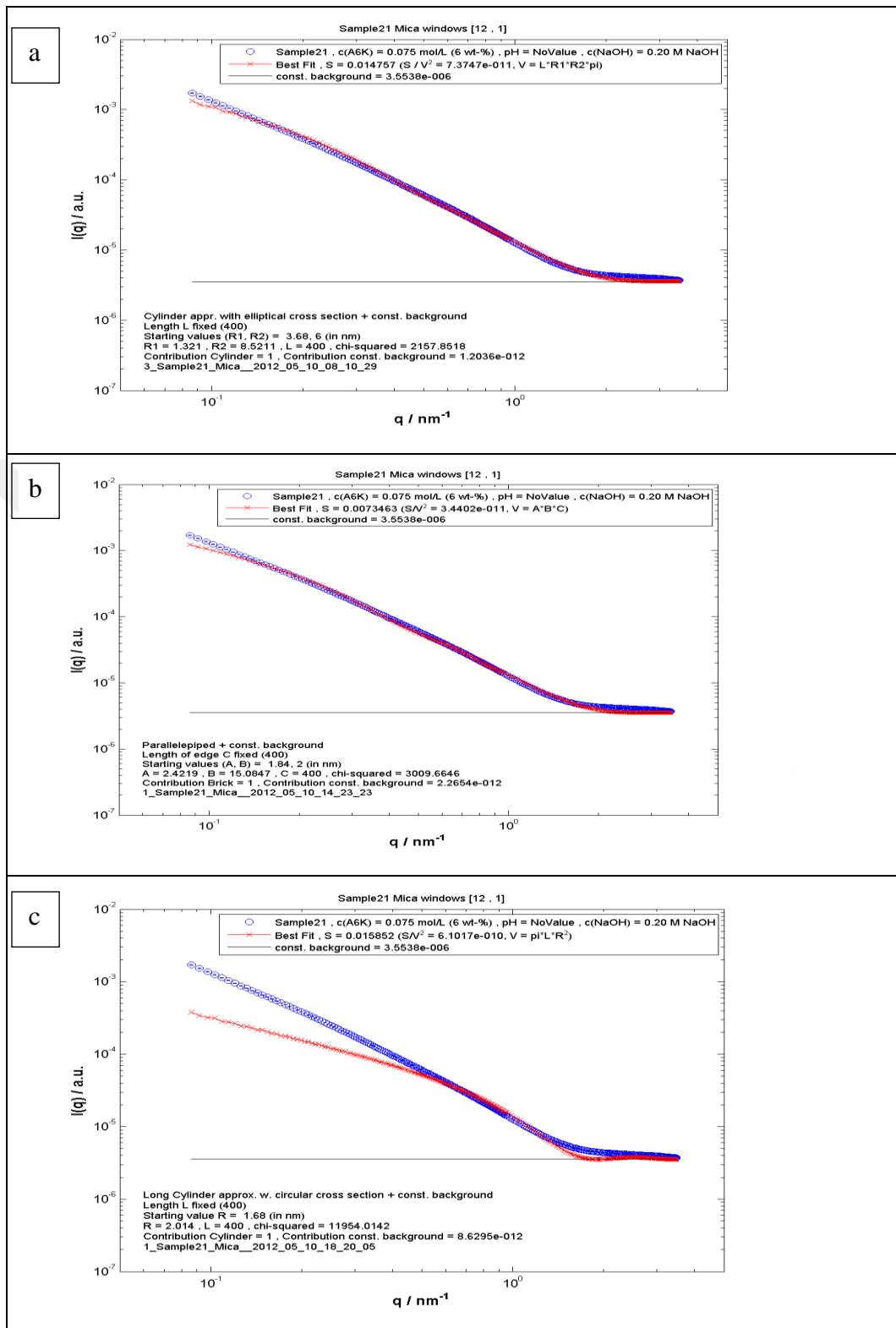
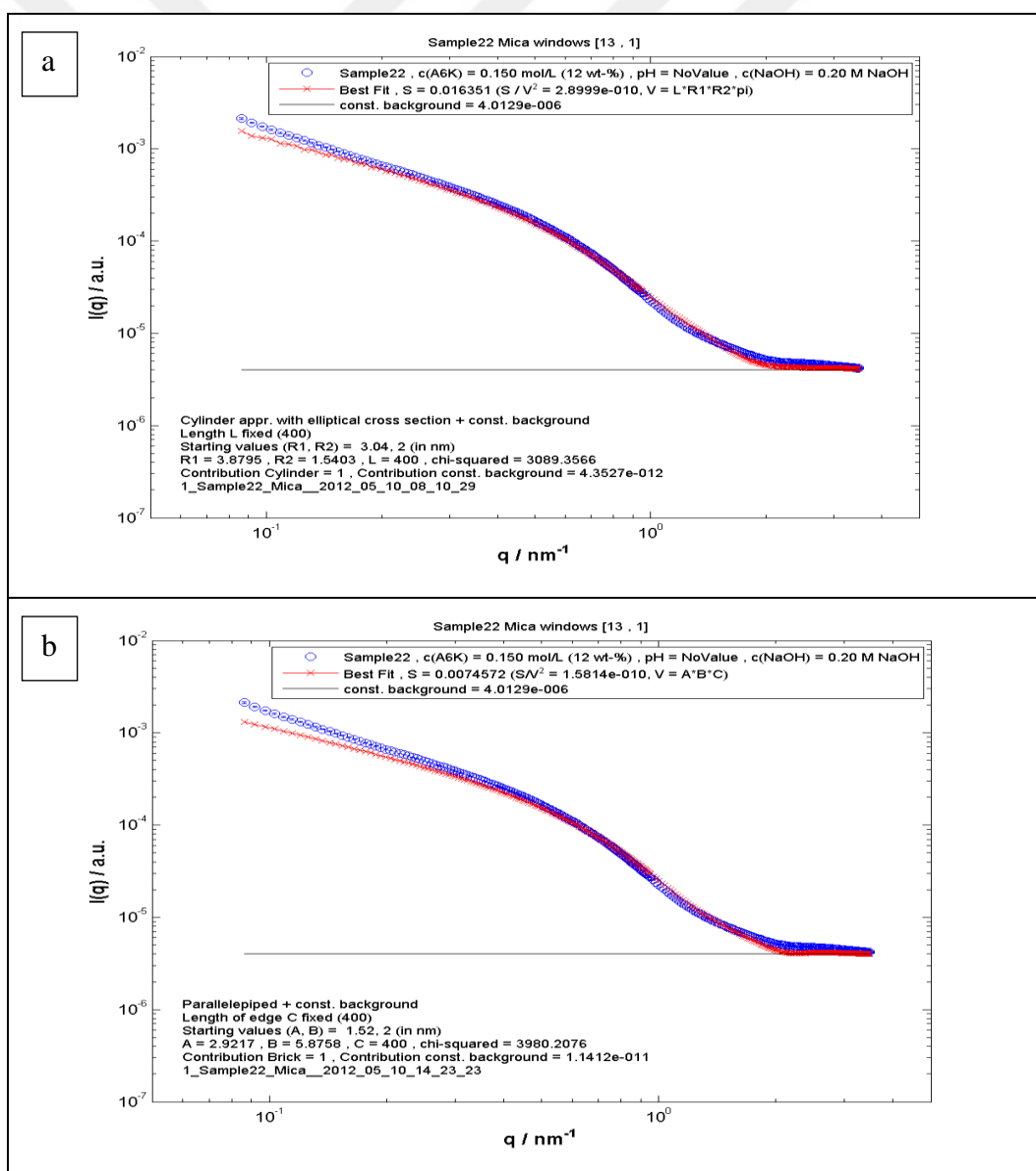


Figure 4.11. 6 per cent (tfa)₂-A6K in 0.2 M NaOH for varying models a) Elliptical cylinder model $R_1/R_2 = 8.5/1.3 = 6.5$ ($D_1/D_2 = 17.0/2.6$) b) Parallelepiped model $A/B = 15.1/2.4 = 6.3$
 c) Circular cylinder model

The best description of 12 per cent (tfa)₂-A6K in 0.2 M NaOH is achieved with elliptical cylinder which describes the scattering data at small q values a shade better than the parallelepiped form factor.

This can also be applied to the model fits done on 12 per cent (tfa)₂-A6K in 0.1 M NaOH.

8 per cent (tfa)₂-A6K in 0.2 M NaOH can best be described with the elliptical cylinder. The parallelepiped provides a good description of the scattering data too, but fails to reproduce the scattering intensity at the smallest q values. The quality of the fit in the case of the elliptical cylinder depends on the initial values of the cross section R₁ and R₂ (Figure 4.14.b). Figure 4.12-4.14 represents the results.



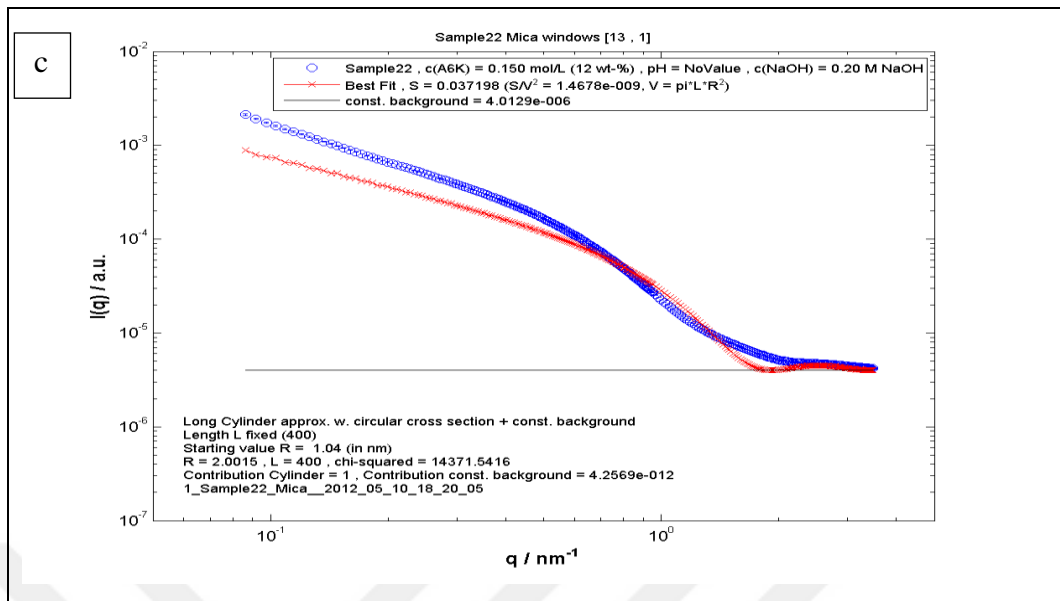
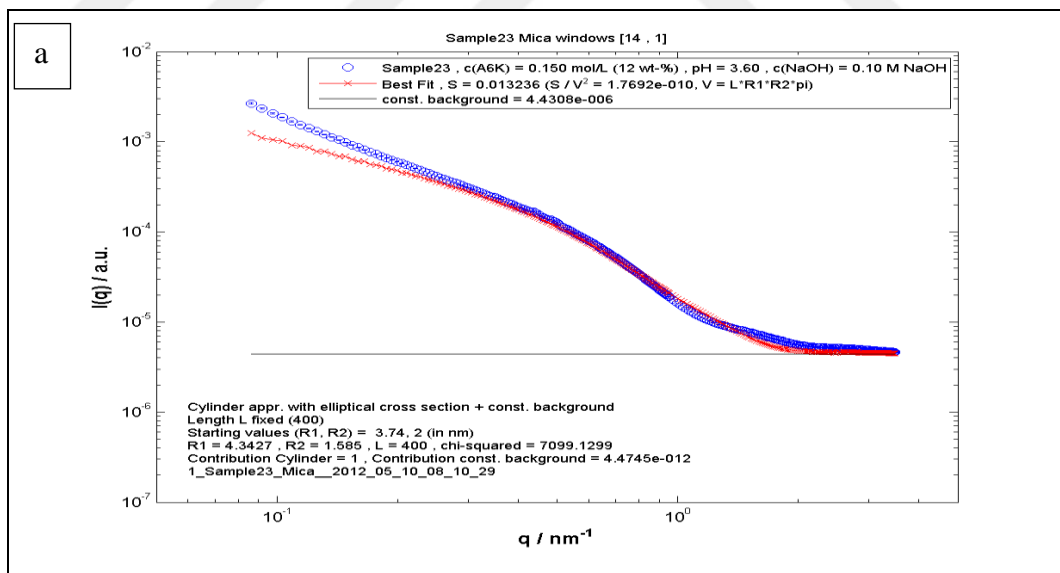


Figure 4.12. 12 Per cent (tfa)₂-A6K in 0.2 M NaOH for varying models a) Elliptical cylinder model $R_1/R_2 = 3.9/1.5 = 2.6$ ($D_1/D_2 = 7.8/3.0$) b) Parallelepiped model $A/B = 5.9/2.9 = 2.0$ c) Circular cylinder model



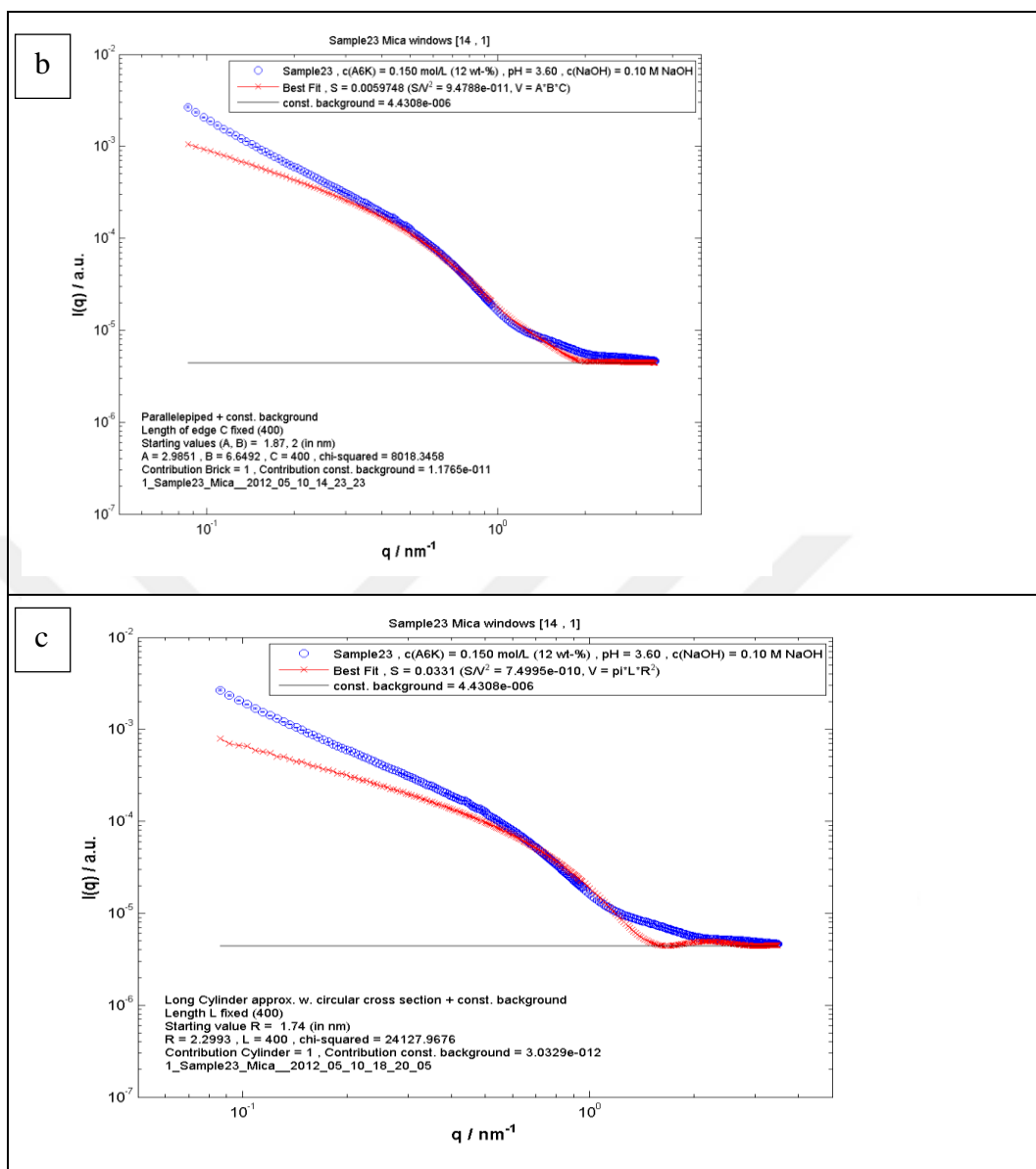
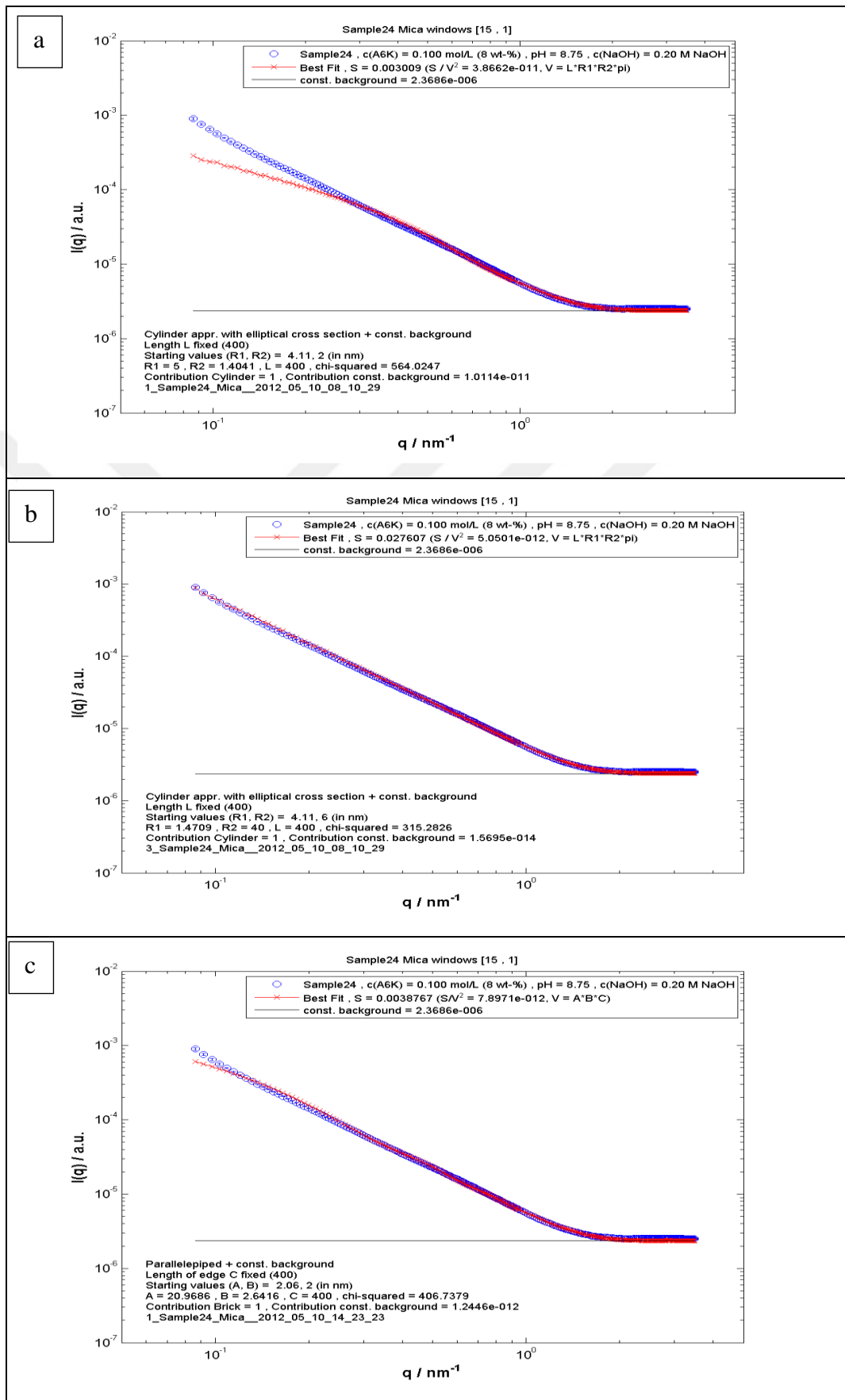


Figure 4.13. 12 Per cent (tfa)₂-A6K in 0.1 M NaOH for varying models a) Elliptical cylinder model $R_1/R_2 = 4.3/1.6 = 2.7$ ($D_1/D_2 = 8.6/3.2$) b) Parallelepiped model $A/B = 6.6/3.0 = 2.2$ c) Circular cylinder model



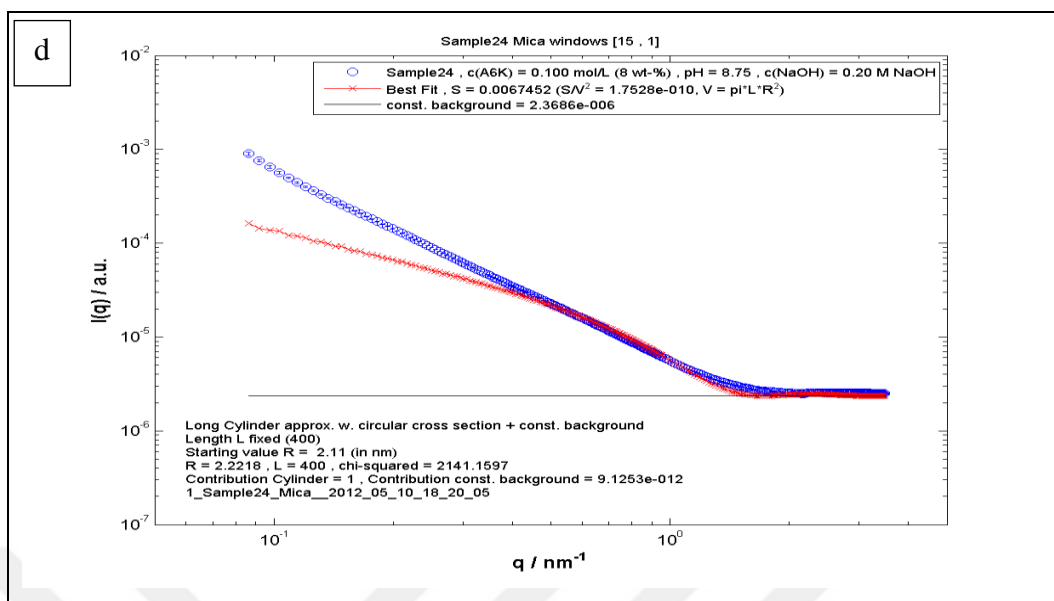


Figure 4.14. 8 Per cent $(\text{tfa})_2\text{-A6K}$ in 0.2 M NaOH for varying models a) Elliptical cylinder model b) Elliptical cylinder model but with a different initial value for R_2 $R_1/R_2 = 40.0/1.5 = 26.7$ ($D_1/D_2 = 80.0/3.0$) c) Parallelepiped model $A/B = 21.0/2.6 = 8.1$ d) Circular cylinder model

As a summary, Table of 4.7-4.8 provide a brief content of the relevant structures that exist in the investigated sample for three different mathematical models supplied by SAXS data here above.

Table 4.7. Summary of the existence of the structures for three models at different NaOH molarity while the peptide concentration kept constant

% $[(\text{tfa})_2\text{-A6K}]$	$[\text{NaOH}]$ (M)	Fitted Model	% $[(\text{tfa})_2\text{-A6K}]$	$[\text{NaOH}]$ (M)	Fitted Model
14%	0.01	Elliptical Cyl.			
14%	0.1	Elliptical Cyl.	12%	0.1	Elliptical Cyl.
14%	0.2	Circular Cyl.	12%	0.2	Elliptical Cyl.
14%	0.5	Elliptical Cyl.	12%	0.5	Elliptical Cyl.

Table 4.8. Summary of the existence of the structures for three models at different peptide concentration while [NaOH] kept constant

% [(tfa) ₂ - A6K]	[NaOH](M)	Fitted Model	%[(tfa) ₂ - A6K]	[NaOH](M)	Fitted Model
8%	0.1	None of them	6%	0.2	Elliptical Cyl.
10%	0.1	None of them	8%	0.2	Elliptical Cyl.
12%	0.1	Elliptical Cyl.	10%	0.2	Elliptical Cyl.
14%	0.1	Elliptical Cyl.	14%	0.2	Circular Cyl.

As a conclusion, most of the formed structures in the solutions at altering pH values are cylinder with elliptical cross-section. At low peptide concentrations and relatively low NaOH concentrations (8 per cent-10 per cent in 0.1 M NaOH), none of these three models seem suitable. One of the strong reason is, the alignment of the self-assembled formation has not coexist yet, while there possibly are some small fragments. This is supported by increasing concentration (12 per cent -14 per cent in 0.1 M NaOH) results with the formation of elliptical cylinder. It seemed the solution was still dynamic, where self-assembly still takes place.

As long as the concentration of the peptide increases at constant NaOH of 0.2 M, the elliptical cylinder model is compatible up to around 10 per cent. When the concentration is 14 per cent, the structure stays as a cylinder but rolls up into a circular cross-section. One possible suggestion is that the system is still dynamic, the upcoming associations or structures may come closer and roll the present structures of elliptical dimension into a circular shape.

Moreover, majority of the formed structures for 12 per cent and 14 per cent at changing NaOH concentrations are cylinder with elliptical cross-section. Remembering for 12 per cent, apart from 0.01 M NaOH, all the samples are turbid, the samples seems to be more consistent for a relatively extended pH range to stay elliptical cylinder.

4.2.3. Extended Phase Diagram

Here, to understand more about peptide self-assembly, particularly amyloid β peptides, A6K was a model peptide to function the self-assembly since the similarity of forming β -sheets. Former research revealed that A6K undergo to self-assemble into nanotubes in D_2O [58]. Unexpectedly, these small peptides role distinctive comparing to the other small peptides especially longer amyloid peptides that generally tend to organized into fibers. Nevertheless, A6K is not the only peptides who forms nanotubes, but the first one that was imaged by cryo-TEM for these kinds of systems by Bucak et al. The results introduced that the salt, $(tfa)_2$ -A6K is totally soluble in water at low concentrations ($\phi < 12$ per cent, where ϕ is the volume fraction). The solution seems transparent and occurs an isotropic phase. Above the 'cac' (>12 per cent), the aqueous solution of the peptide $(tfa)_2$ -A6K transfers to the nematic phase with a dramatic change of turbidity and a spontaneous association of the nanotubes exist that was confirmed with the images of cryo-TEM and the results of SAXS represented in Figure 4.15. The oscillations of the SAXS pattern indicate the forming structures of nanotubes when the concentration exceeds 12 per cent for the values of q in between 0.1 - 1 nm^{-1} [3].

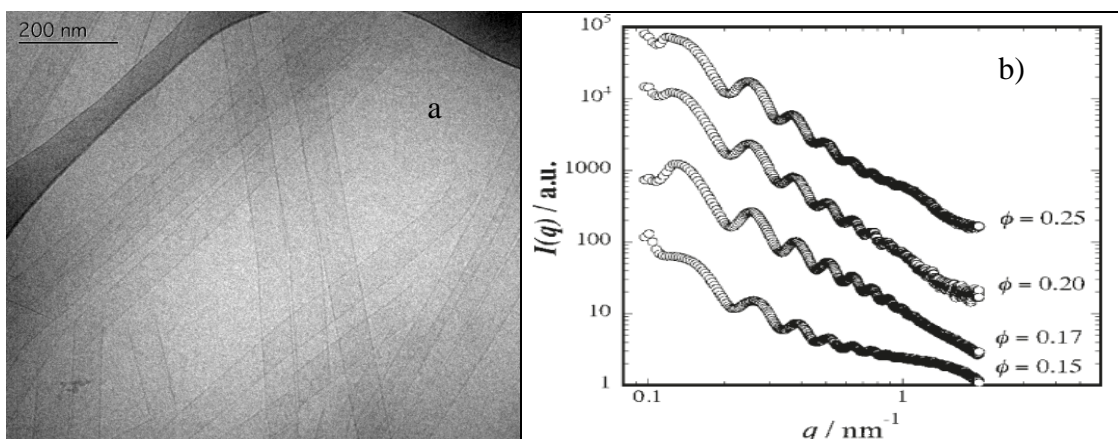


Figure 4.15. Imaging data of $(tfa)_2$ -A6K a) Cryo-TEM images of $(tfa)_2$ -A6K b) SAXS data for $\phi=0.15$ - 0.25 of $(tfa)_2$ -A6K [3]

Additionally, one estimates the formation of nanotubes in water of this salt, $(tfa)_2$ -A6K coexists through the formation of antiparallel β -sheets that was confirmed by FTIR spectra represented in Figure 4.16 [57]. Since the formation of hydrogen bonding is one of the

major driving forces of self-assembling of nanostructures, they examined Amide I band of the FTIR spectra. The characteristic band of the solution for increasing concentration up to 13 per cent suggests the presence of unassociated peptides (broad peak at 1648 cm^{-1}) and TFA salt (peak at 1672 cm^{-1}). When the concentration increases to 17 per cent, the formation of a new strand observed (1634 cm^{-1}) confirming the presence of antiparallel β -sheets.

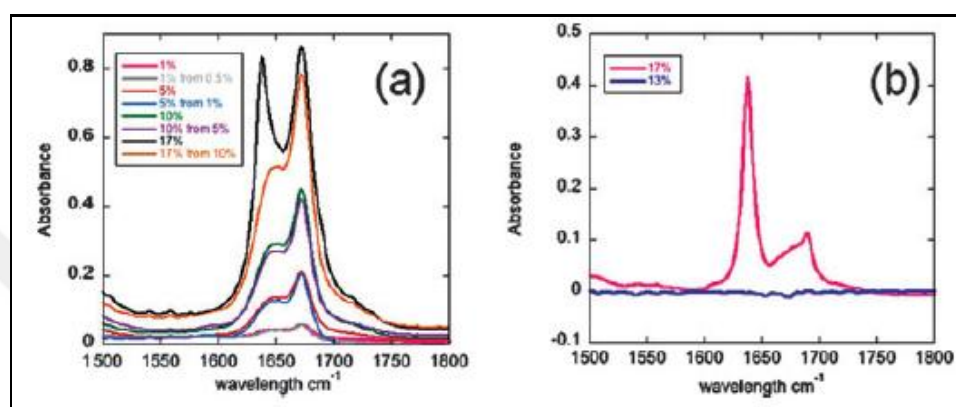


Figure 4.16. FTIR spectra of for (tfa)₂-A6K a) Concentration gradient (1 per cent-17 per cent) b) Lowest and highest levels of amount of (tfa)₂-A6K [57]

Taking the former research further, the study was planned to develop in the scope of how the peptide self-assembles at different conditions. Namely, how their solubility and the forming structures in water vary while changing the pH by adding the strong base NaOH, which changes the charge of the peptide.

In this study, for investigation of the influence of pH on the self-assembly of A6K, NaOH was again occupied and at this time it was added to a certain concentration of peptide (**w_i**) in specified ratios to meet the desired $[\text{NaOH}]/[\text{A6K}]$, further represented as **x**. For instance, at a ratio of $x = 1$ it was assumed that one acidic group was deprotonated. So the ratio approach was chosen instead of adjusting the pH to a certain value. Also, having a consistent notation, all the concentrations of A6K and pH values from SAXS data at previous section were converted to **x** ratio, other name $[\text{NaOH}]/[\text{A6K}]$.

The previous studies have already supplied the peptide has a 'cac' around 12 per cent in water. When the NaOH was occupied to change the pH, it was expected to have lower 'cac'. The turbidity appears to exist at $w_i=0.09$ and increase up to $w_i=0.13$ for $x=0.2$ based

on to the visual observation. So, depending on this observation 'cac' was expected to obtain around $w_i=0.07-0.09$. DLS experiments of the study [78] were performed to determine the exact 'cac' value and the plot of the count rate against mass ratio is represented in Figure 4.17. However, the plot revealed just one point with a higher count rate indicating there is an aggregation ($w_i=0.09$) makes it difficult to determine the exact 'cac'. But still, it is estimated that the 'cac' is between 0.07-0.09 for $x=0.2$.

Additionally, FTIR results of the same study for the concentrations $w_i=0.09$, $x=0.2$ and $w_i=0.11$ and $w_i=0.16$ exhibit information of nanotubes. This data supports the previous findings for peptide in pure water. For $x=0.2$ it seems that there still are some nanotubes in the sample. Additionally, for the sample $w_i=0.07$ at $x=0.5$ appears anisotropic, slightly turbid and had low viscosity. Anisotropy of the sample hardly allows the measurement of DLS to determine the 'cac' for this x ratio. So the plot of the intensity values of SAXS measurements versus to mass ratio revealed the 'cac' to be between $w_i=0.07-0.09$ for $x=0.5$ (Figure 4.17).

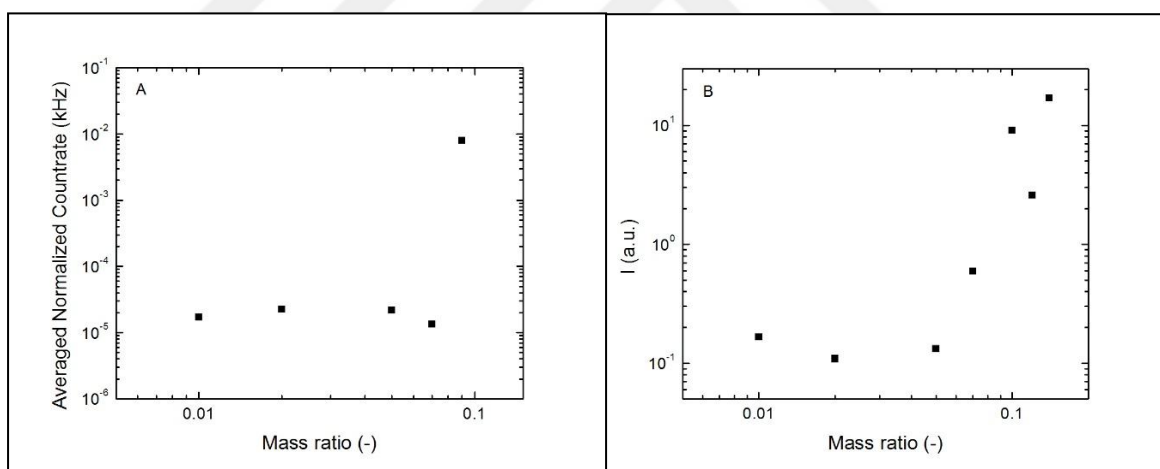


Figure 4.17. Estimation of 'cac' for $x=0.2$ and $x=0.5$ for different mass ratio (w_i) a) The plot of DLS measurement, $x=0.2$ b) Start intensity, obtained by SAXS measurement, $x=0.5$

[78]

The initial slope of the SAXS result for the increasing concentration of $x=0.5$ ($w_i=0.11$) indicated one-dimensional structure such as fibrils. In addition, FTIR spectra for $x=0.5$ $w_i=0.10$ and $w_i=0.14$ revealed an appearance of a peak at 1625 cm^{-1} that suggests a formation of another structure. In the sample $w_i=0.125$ with $x=1$, this peak is followed more dominant showed in Figure 4.18 and the peak around 1640 cm^{-1} is disappeared. It is

known by the theory and as mentioned former research, peak around 1640 cm^{-1} indicates the curved antiparallel β -sheets which is a sign of the formation of nanotubes but also for fibrils. On the other hand, another model peptide of A6D self-assembled into fibrils coexisting with plates [79]. Based on this, similar assumption is possible and self-assembly of sheets presumably present in the sample for the peak of 1625 cm^{-1} .

Since in the sample $w_i=0.125$ with $x = 1$, the peak at 1640 cm^{-1} is completely disappeared it is possible to expect all peptides in this sample to self-assemble into sheets.

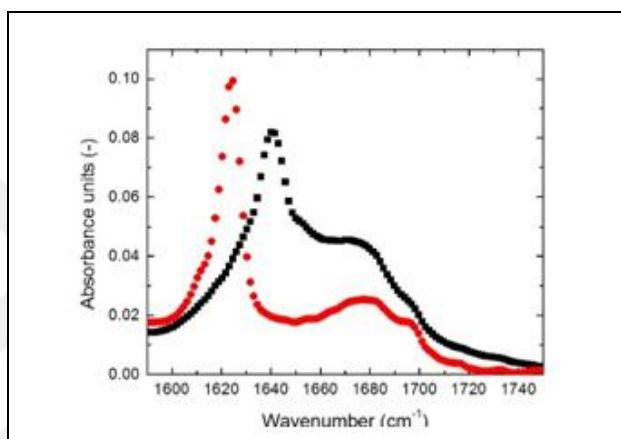


Figure 4.18. FTIR spectra of $w_i = 0.16$ A6K in pure water (black squares) and $w_i = 0.125$ with $x=1$ (red circles) [78]

Combating all the relevant data collected from SAXS, FTIR, pH measurements, turbidity of visual observations and and DLS, cryo-TEM results of the submitted report [78], the extended phase diagram was occurred showed in Figure 4.19.

In this partial phase diagram five different phases can be distinguished. Basically the regions are named: Clear, precipitation, nematic nanotubes, thin sheets or elliptical cylinders and hydrolysis. The parabolic lines are estimations of the phase transition boundaries. Characterization of the samples resulted in this phase diagram, especially focused on the region below the iso-electric point ($x = 2$).

Most likely, precipitation phase coexists for all of the concentrations of peptide followed by hydrolysis for the increasing ratio (x values). Since the peptide has charge (+1.5) at low pH and negatively (-1) at high pH values, the study has been focused on below $x=2$ which is around the iso-electric point.

Moreover, the region of blue curve denotes '*precipitation*' phase. After increasing $x=1$ precipitation starts to exist and almost all the samples between $x=1$ and $x=2$ showed precipitation which is around iso-electric point. At this point, just one nitrogen group is deprotonated. As a consequence of increasing pH by the addition of NaOH and deprotonation of amino groups, presumably weakened the salt-bridges and even completely disrupted them. Thus, disturbed nanotubes in the form of small tape-like or sheet like structures and fragments of aggregated peptide precipitate in the samples.

Known from the theory and literature the rate of hydrolysis increases for peptides at high pH [80-82], which is consistent with the observations. High x ratios especially above $x=5$, '*hydrolysis*' is shown on the phase diagram.

In addition, all the data of SAXS and visual observations described in the previous section were inserted to the phase diagram of extended version including all the collected data.

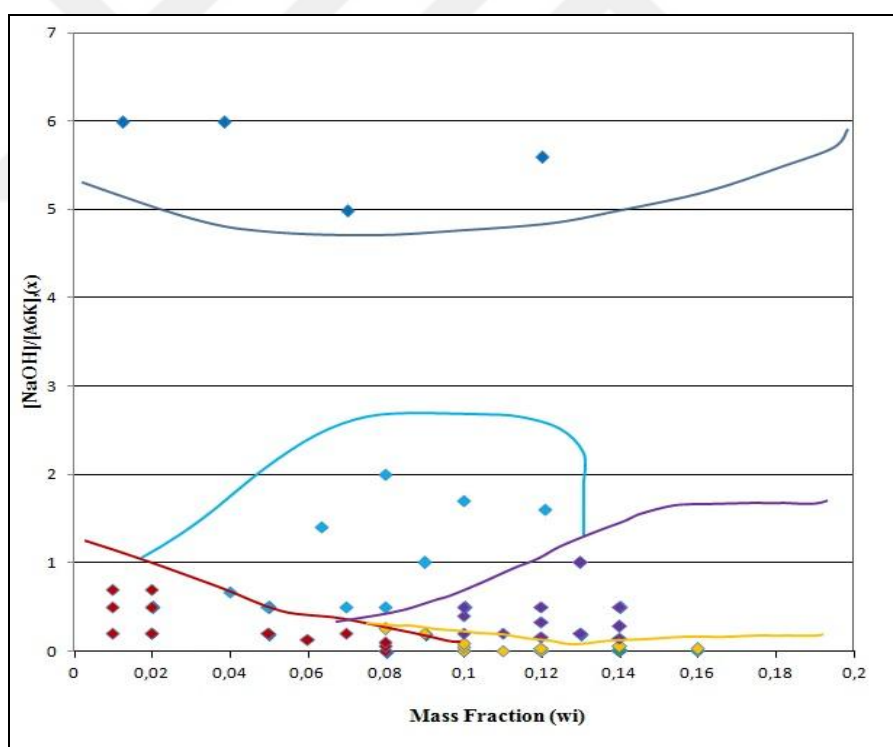


Figure 4.19. Phase Diagram of (tfa)₂-A6K [The region below red-line and dots with red squares are '*Clear*' phase, region below light blue parabolic curve is '*Precipitation*' phase, the region between purple and yellow line is '*Thin Sheets, Elliptical Cylinders*', the region below yellow line is '*Nematic*' phase with nanotubes, and the region above the dark blue curve is '*Hydrolysis*'.

The region between light and dark blue curves is unknown yet]

4.3. INVESTIGATION OF (Cl)₂-A₆K

4.3.1. Physical Properties

Additionally, effect of counter-ion of the peptide on the self-organization process was investigated using a different counter-ion. Therefore, (Cl)₂-A₆K was chosen and prepared in D₂O at different concentrations. The physical features of the solutions are listed in Table 4.9.

Table 4.9. Prepared samples at various concentrations at D₂O for (Cl)₂-A₆K

Solvent	Sample (Cl) ₂ -A ₆ K	pH	Turbidity
D ₂ O	10 % (Cl) ₂ -A ₆ K	2.50	Slightly
D ₂ O	12 % A ₆ K (Cl) ₂ -A ₆ K	2.21	Slightly
D ₂ O	14 % A ₆ K (Cl) ₂ -A ₆ K	2.03	Slightly
D ₂ O	16 % A ₆ K (Cl) ₂ -A ₆ K	1.79	Turbid

As it was expected, pH of the (Cl)₂-A₆K solutions exhibited acidic character in D₂O. Altering counter-ion of the peptide did not bring out a significant shift for the strength of the acidity of the media owing to similar electrostatic forces. Still, the turbidity of 10 per cent-14 per cent (tfa)₂-A₆K in H₂O appears less turbid relatively compared to the same concentration of samples for (Cl)₂-A₆K in D₂O.

Comparison of the (Cl)₂-A₆K in D₂O for varying concentrations are demonstrated in Figure 4.20.

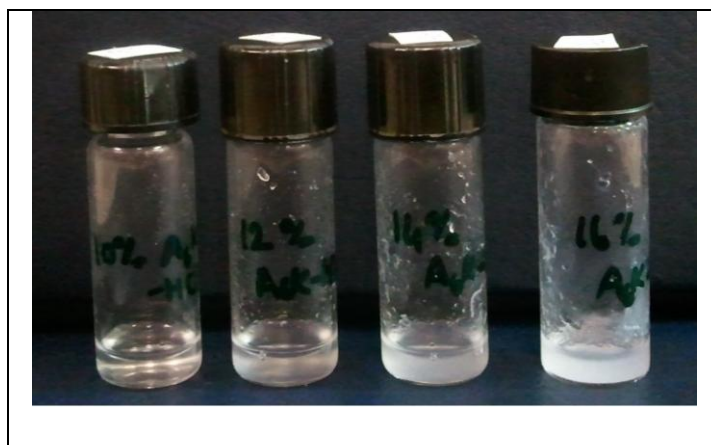


Figure 4.20. Image of $(\text{Cl})_2\text{-A6K}$ for varying concentration in D_2O

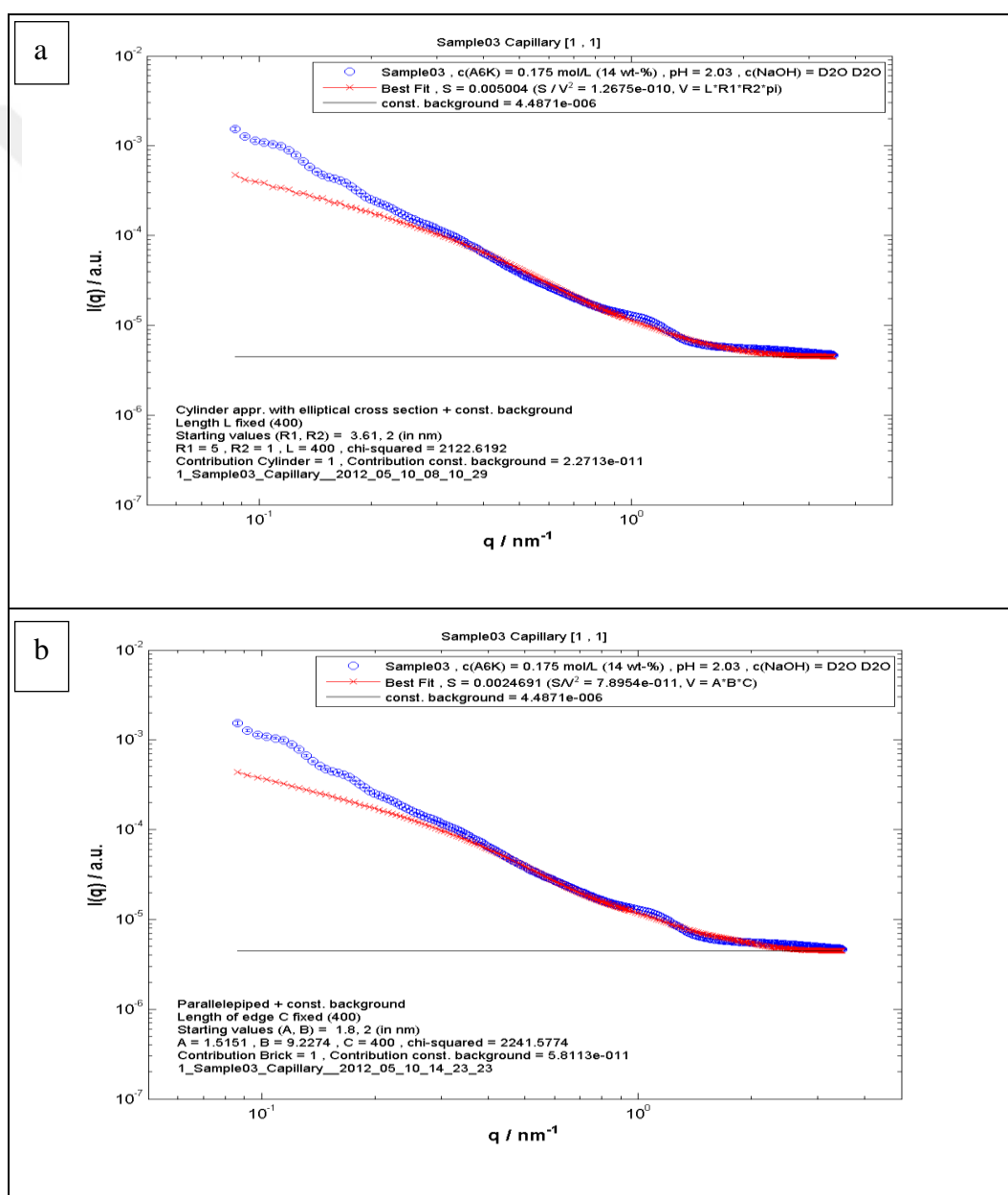
It is clearly seen that turbidity of the solutions increases as the concentrations rise. Presumably, the formation of self-assembled fragments or structures coexists in the samples around or somewhere below the concentration of 12 per cent by visual observation and the solution seems anisotropic. On the other hand, partial phase map of the solution of $(\text{tfa})_2\text{-A6K}$ revealed a spontaneous organization of the nematic phase. Here, the appearance of the system seems barely different which is supported with the data of SAXS for $(\text{Cl})_2\text{-A6K}$ at the next section. It exerts a possibility of formation for the elliptical cylinder rather than an exact hollow nanotubes resulted for $(\text{tfa})_2\text{-A6K}$. The model fit of elliptical cylinder was not sufficient enough for the best description, however it is clear that the hollow nanotubes do not persist in the presence of Cl^- counter-ions.

4.3.2. Self Assembly Behaviour by SAXS Experiments

This salt form of the peptide was also examined by SAXS technique to understand more about the effect of counter-ion. Prepared solutions (14 per cent-16 per cent $(\text{Cl})_2\text{-A6K}$) were analysed with the same instrumental set up described in section 4.2.2. The relevant data are listed in Table 4.10. As it can be clearly seen from the Figures 4.21– 4.22, none of the models applied are suited to describe the experimental scattering curves. First, the oscillations at low q values could not be reproduced with one of the models. Second, the shoulder at around $q = 1 \text{ nm}^{-1}$ could not be reproduced with the model fits. Third, the initial slope of the experimental data is bigger than the slope of the models. Here, it turns out, that

the circular cylinder is the worst fit because its slope is much smaller than the slope of the experimental scattering curve and also smaller than the slope of the other two models. The reason for this behaviour is that a second cross section size parameter can be fitted to the experimental data with the brick stone or the elliptical cylinder.

This can also be applied to the model fits which were performed with 16 per cent $(\text{Cl})_2\text{-A6K}$ in D_2O .



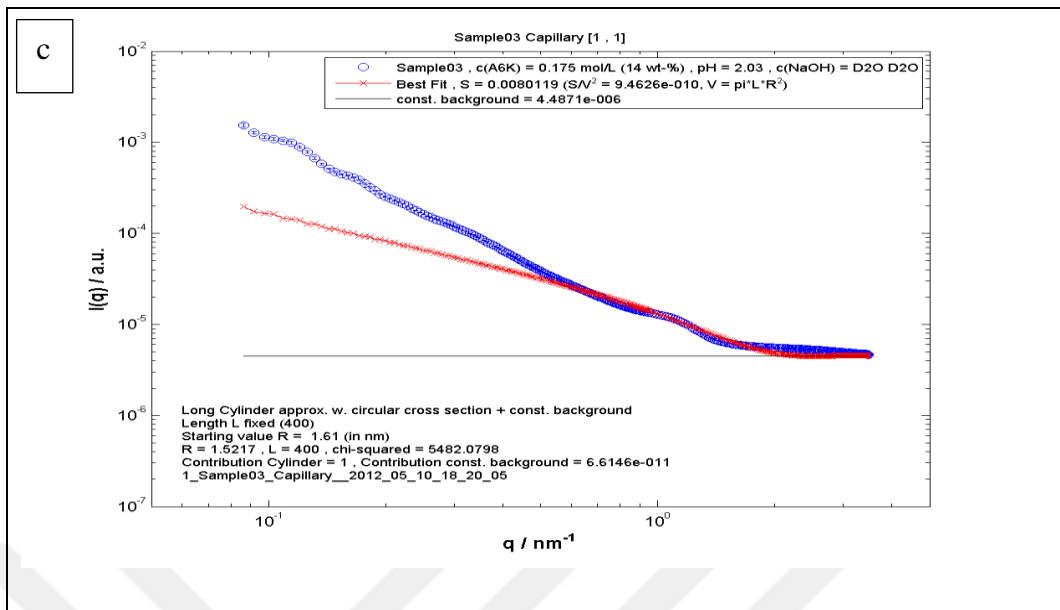
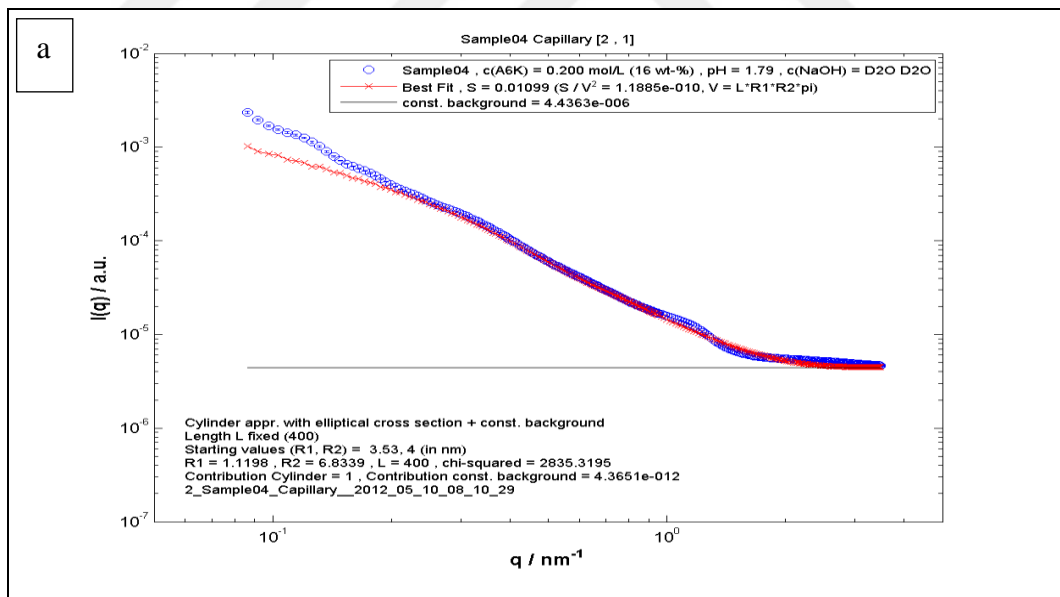


Figure 4.21. 14 Per cent $(\text{Cl})_2\text{-A}_6\text{K}$ in D_2O for varying models a) Elliptical cylinder model
 b) Parallelepiped model c) Circular cylinder model



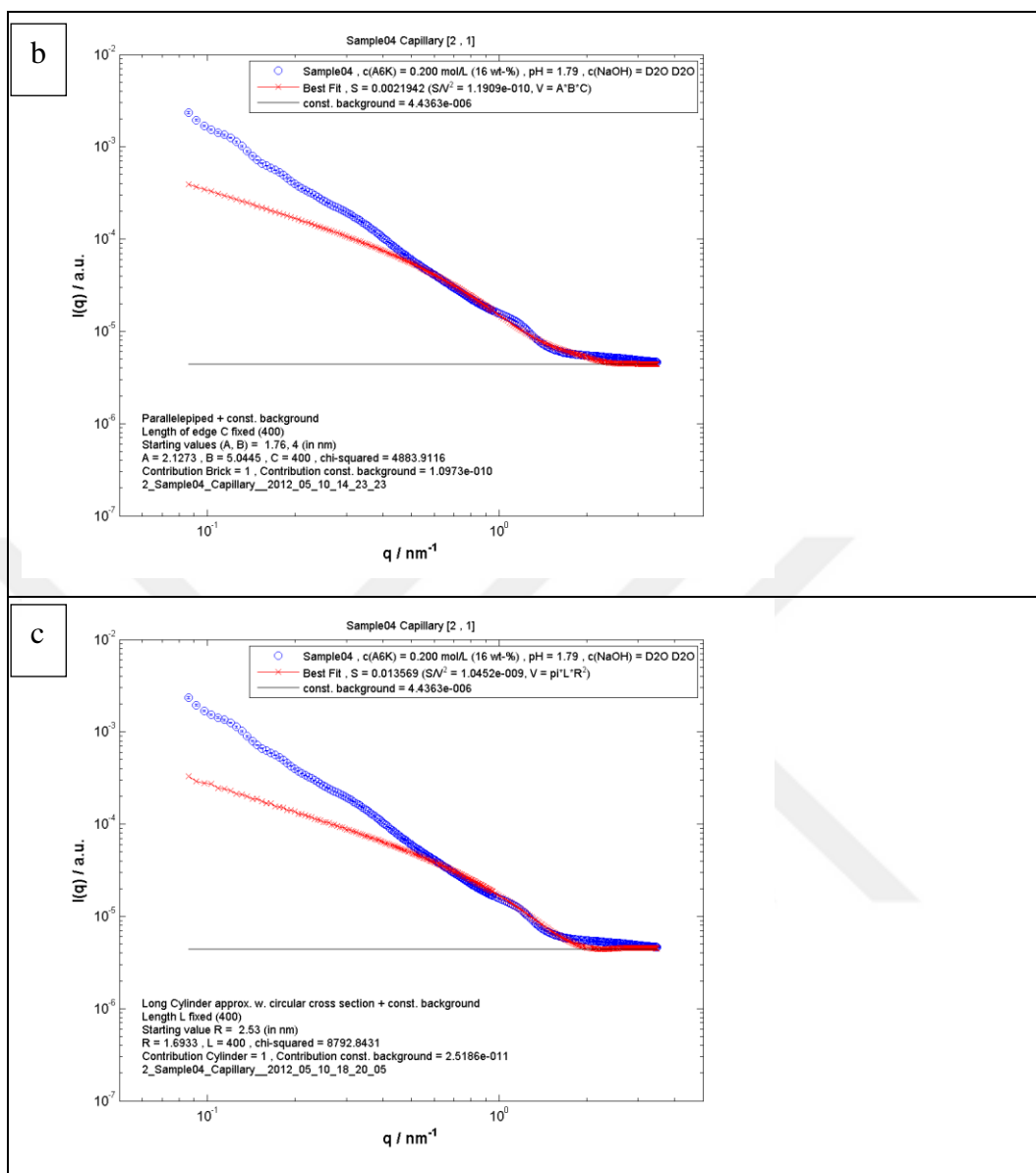


Figure 4.22. 16 Per cent $(\text{Cl})_2\text{-A}_6\text{K}$ in D_2O for varying models a) Elliptical cylinder model b) Parallelepiped model c) Circular cylinder model

As a consequence, the estimation was performed with modeling for three varying structures. Among these models cylinder with elliptical cross-section appears to have relatively better description. On the other hand, the difference of the slopes for both experimental and model curves and the values for low q values complicates this approach.

Furthermore, there are slight oscillations around $q=10^{-1}$ value for experimental data (blue curves). It is possible to say that it is one of the indications of self-assembled nanotube

formation. Presumably, the sample contains bimodal structures or the formation of the nanotube was still in progress.

4.4. SUMMARY OF (Cl)₂-A6K IN D₂O AND (TFA)₂-A6K AT VARYING NaOH SOLUTION

Here, all the related dimensions of self-assembled structures obtained SAXS calculations are summed up. The cross section diameters and the cross section edge lengths are listed in Table 4.10.

Table 4.10. The cross section diameters and the cross section edge lengths

c(A6K) / wt-%	c(NaOH) / mol/L	pH	Elliptical cylinder	Parallelepiped
			D1/D2 (= ratio)	A/B (= ratio)
14 (A6K-Cl)	D ₂ O	2.03	-	-
16 (A6K-Cl)	D ₂ O	1.79	-	-
16	0.01	1.97	-	-
14	0.01	2.55	-	-
14	0.10	3.34	10.0/2.8 (= 3.6)	6.6/2.6 (= 2.5)
14	0.20	5.2	8.2/3.4 (= 2.4)	6.3/4.3 (= 1.5)
14	0.50	11.8	17.0/2.8 (= 6.1)	8.7/2.6 (= 3.3)
12	0.50	12.19	9.0/2.6 (= 3.5)	7.8/2.4 (= 3.3)
12	0.20	5.7	7.8/3.0 (= 2.6)	5.9/2.9 (= 2.0)
12	0.10	3.60	8.6/3.2 (= 2.7)	6.6/3.0 (= 2.2)
10	0.20	6.83	8.6/3.4 (= 2.5)	6.6/3.2 (= 2.1)
10	0.10	3.88	8.2/3.6 (= 2.3)	6.5/3.5 (= 1.9)
8	0.20	8.75	40.0/1.5 (= 26.7)	21.0/2.6 (= 8.1)
8	0.10	4.07	8.0/4.6 (= 3.4)	6.6/4.3 (= 1.5)
6	0.20	11.6	17.0/2.6 (= 6.5)	15.1/2.4 (= 6.3)

When the peptide concentration is constant, increasing pH, namely NaOH concentration, generally reveals higher ratio of diameters of the structures. This is an evidence of the

cross-section is more elliptical or extended at higher pH's while the curvature appears more round shape for lower ones.

As a summary, the model peptide A6K revealed some significant self-assembled structures. The formation of nanotubes in aqueous solution for non-encapped A6K exhibits hollow tubular self-assembled structures with a circular cross-section was the starting point of the investigation. The results exposed self-assembling of model peptide A6K was very much pH-dependent. Varying conditions were analysed and as long as the pH increases the turbidity starts to appear lower concentrations. The exact 'cac' values have obtained at smaller mass ratio (w_i). This was also confirmed by the visual observations followed by the change of turbidity.

Furthermore, the major structures obtained by SAXS data were cylinder with elliptical cross-section for $w_i=0.08-0.14$ at the range $x=0.002-0.5$ (namely, 0.01M NaOH-1M NaOH for varying peptide concentrations or mass ratio). Presumably, other structures contain sheets, tapes or one-dimensional fibrils coexist in this range since the system is dynamic.

Increasing x ratio (>1) for the mass ratio, till $x=2$ (iso-electric point) around $w_i=0.02-0.14$, firstly results precipitation confirmed also by visual observation in the form of amorphous aggregates. When x ratio dramatically change above ($x>5$) hydrolysis appears also confirmed with the literature [80-82].

Upon changing the pH, the charge of the peptides decreases and finally changes the structures in the system or disrupt the formed ones in aqueous media.

5. APPLICATION OF PEPTIDE A10K

In order to employ these peptides in biotechnology, the applications of peptides for cell culture were explored in this section.

Basically, this chapter describes a potential biotechnological approach for peptide A10K. So far, A6K peptide were analyzed in detailed described in the pervious chapter and throughout the journals published by Bucak et al [3]. The study was planned to enlarged for the field of biotechnology since the peptides have the potential features on biological organisms and living cells. Therefore, the study was planned to focus on our studied peptide with a little difference. A10K was planned to utilize in the current study for the application of biotechnology. Bearing in mind A10K has longer Alanine residues which allows the peptide become more hydrophobic feature [1], the required amount of the peptide would have been less self-assemble, i.e. low 'cac' compared to A6K. The self-assembly structures formed by A10K was extensively studied by Bucak [1, 3, 58]. Therefore the advantage of studying of low concentrations of peptide was considered. For this purpose, cytotoxicity and wound healing performance of the peptide A10K for different cell-lines were investigated.

Before the experimental investigation of wound for A10K, it is better to look in detail what wound and its features are. Wound healing is the dynamic process which describes the recovery of the cells when part of the tissues in the body or in the organism, or the skin is damaged by a trauma [83]. Despite still there is not a proper consensus if the wound healing process occurs by three or four phases, it is possible to summarize the steps as inflammatory phase, proliferation phase, and remodeling phase for the process [84]. The response of the recovery of the wound could be in both ways associated with normal or pathologic healing. The normal healing process starts at the time when the tissue is injured. When blood spills over into the region of the injury, the platelets get in touch with exposed collagen and other components of the extracellular matrix. This contact stimulates the platelets to secrete clotting factors, substantial growth factors and cytokines like platelet-derived growth factor (PDGF) and transforming growth factor beta (TGF- β). After this step, generally called *hemostasis*, the neutrophils go into the region of the wound and crucial task of phagocytosis takes a start to remove foreign materials, bacteria and injured

tissue. As long as this *inflammatory* phase goes on, the macrophages arise and keep on the process of phagocytosis by releasing more PDGF and TGF β . When the region of the wound is refined, fibroblasts migrate in to initiate the *proliferative* phase and compose fresh extracellular matrix. The fresh collagen matrix then grows into cross-linked and aligned along the ultimate *remodeling* phase. During this highly controlled and efficient maintenance and reparing process, a great number of cell-signaling events are required and performed. Additionally, the recovery of the wound in pathologic conditions like non-healing pressure ulcers, this efficient and organized process disappears and the ulcers are locked into a condition of chronic inflammation characterized by numerous neutrophil infiltration with related reactive oxygen species and disruptive enzymes. Healing continues once after the inflammation is managed [85, 86].

The events that occur during the healing of a normal wound process are represented in Table 5.1.

Table 5.1. The events that take place during normal wound healing phases [87]

Phase	Cellular and Bio-physiology Events
Hemostasis	<ol style="list-style-type: none"> 1. Vascular Constriction 2. Platelet aggregation, degranulation and fibrin formation (thrombus)
Inflammation	<ol style="list-style-type: none"> 1. Neutrophil infiltration 2. Monocyte infiltration and differentiation to macrophage 3. Lymphocyte infiltration.
Proliferation	<ol style="list-style-type: none"> 1. Re-epithelialization 2. Angiogenesis 3. Collagen synthesis 4. ECM formation
Remodelling	<ol style="list-style-type: none"> 1. Collagen remodelling 2. Vascular maturation and regression

The scheme of the steps for healing is shown in Figure 5.1.

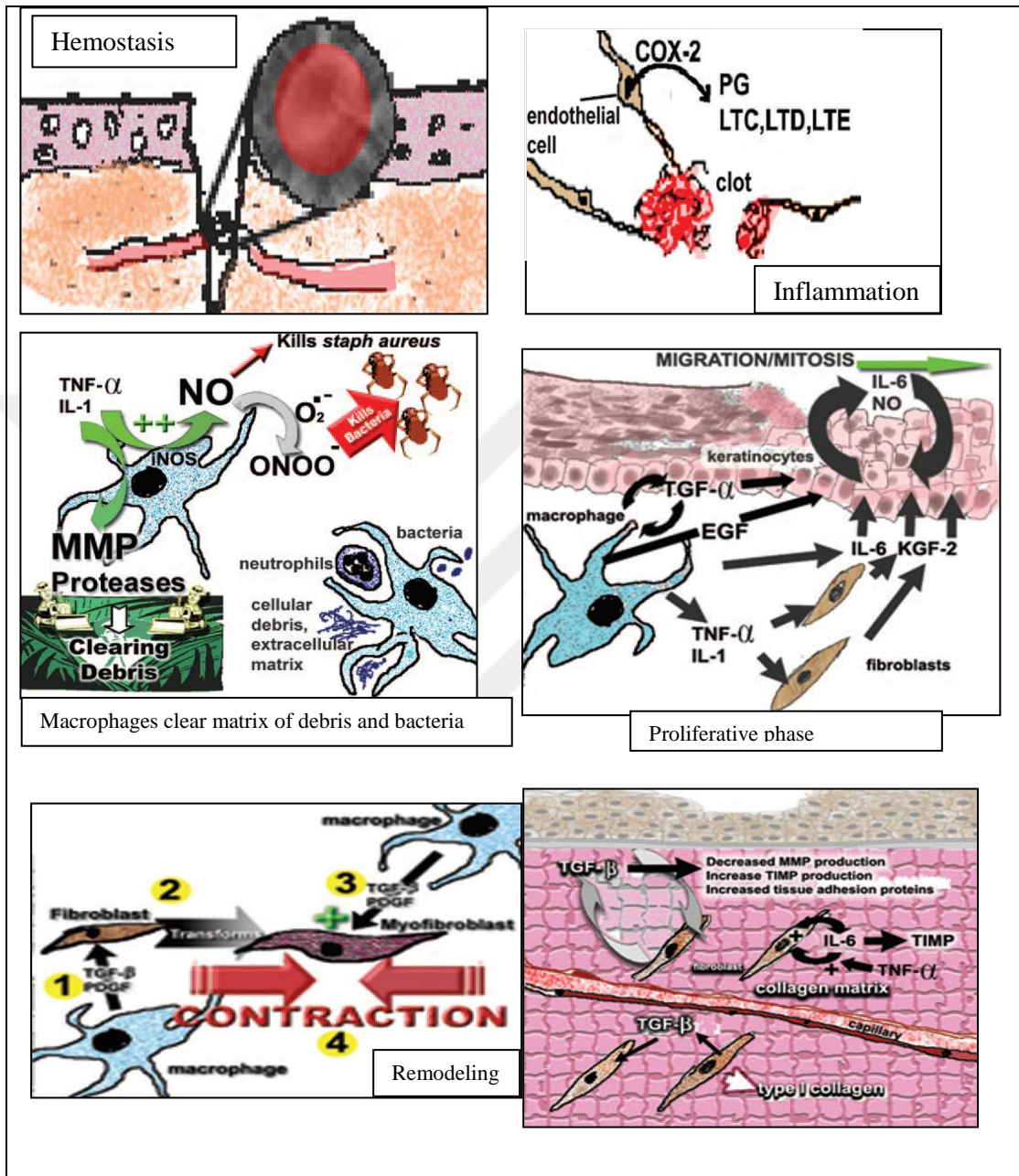


Figure 5.1. Summary of Phases for Wound Healing [88]

As long as the wound is one of the major concerns of the biological organism, there have been extensive studies about this field in the literature. Schneider et al. designed a self-assembling peptide scaffold by combining Epidermal Growth Factor (EGF) since EGF has a great potential of proliferation and stimulation for migration of keratinocytes at the

wound edge. Peptide of 16 amino-acids (RADA16-I, Ac-RADARADARADARADA-CONH₂) that undergo self-assembly into hydrogels were used in the relevant study. Using the peptide scaffold significantly increased the rate of wound closure and releasing of EGF has been increased by using this ionic self-complementary peptides [89].

Another study exhibits potential results for wound healing and infectious diseases by employing host defense peptides, also called antimicrobial peptides. Host defense peptides are classified into four categories such as linear α -helical structure, β -sheet structure stabilized by characteristic disulfide bridges, peptides with predominance of at least one amino acid, and loop-structured peptides. Here, β -sheet structure is the one that is similar to our designed peptide obtained during self-assembling process. The study exerted sufficient response of wound healing by using varying host defence peptides with their multiple functions. They are able to innate immune system as antimicrobial and immunomodulating agents which are key parameters of wound healing [90].

Another peptide of Innate Defense Regulators (IDRs) that are synthetic immunomodulatory versions of natural host defense peptides have been used by Steinststraesser et al to demonstrate wound healing activities. They obtained great results of the efficacy of IDR-1018 (peptide) in diabetic and non-diabetic wound healing models since they already reported the peptide to suppress pro-inflammatory feature [90-93].

First the behaviour of A10K in cell-medium will be investigated as constituents of the medium may affect how A10K self-assembles.

5.1. PHYSICAL PROPERTIES OF PEPTIDE-MEDIUM SOLUTION

It is well-known that medium is the major component of the cell culture through *in vitro* studies. Thus, behaviour of A10K was studied in the presence of medium of the cell for physicochemical properties at the first stage.

So, A10K peptide was prepared at DMEM (high glucose-complete, contains 10 per cent FBS and 1 per cent PSA) medium for the concentration of 2×10^4 $\mu\text{g/mL}$ and used for the determination of Zeta-Potential and pH measurements. Obtained data is presented in Table 5.2 and Table 5.3. The measurement of Zeta-Potential of only medium without peptide is

represented in Table 5.2 as well. Complete medium describes the medium that contains FBS protein and antibiotic. Incomplete medium refers to the medium without FBS protein and antibiotic.

Table 5.2. Zeta-Potential data of 2×10^4 $\mu\text{g/mL}$ A₁₀K in medium, incomplete medium and FBS

Sample Measurements	Z-potential of 2×10^4 $\mu\text{g/mL}$ A10K in complete medium (mV)	Z-potential of Complete Medium (DMEM HG) (mV)	Z-potential of Incomplete Medium (DMEM HG)	Z-potential of FBS (mV)
Measurement 1	4.44	-7.29	-4.93	-5.23
Measurement 2	3.09	-7.72	-2.57	-6.42
Measurement 3	3.37	-7.44	-6.93	-6.18
Mean	3.63 ± 0.712	-7.48 ± 0.218	-4.81 ± 2.18	-5.94 ± 0.62

It is clearly seen that addition of peptide solution to the medium dramatically changes the charge of the media from negative to positive. This is expected to cause the cell membrane's pores enlarge.

Table 5.3. pH measurements of 2×10^4 $\mu\text{g/mL}$ A₁₀K in medium, incomplete medium, FBS

Sample Measurements	pH of 2×10^4 $\mu\text{g/mL}$ A10K in Complete Medium	pH of Complete Medium (DMEM HG)	pH of Incomplete Medium (DMEM HG)	pH of FBS
Measurement 1	6.24	7.28	7.18	7.45
Measurement 2	6.38	7.32	7.22	7.32
Measurement 3	6.30	7.21	7.15	7.38
Mean	6.30 ± 0.070	7.27 ± 0.06	7.18 ± 0.04	7.38 ± 0.07

The pH of the commercial medium (incomplete medium) is supplied at pH of 7.0-7.4 that [94]. According to commercial suppliers the pH of FBS is expected to be obtained at 6.5-8.5 [95, 96]. Additionally, the aqueous solution of A10K peptide was expected to have an acidic character similar to that of A6K. Similarly it was revealed that alanine based peptides containing lysine residues differentiate the acidic property by the influence on electrostatic field [97]. Adding the peptide into the medium does not significantly change the pH of the medium which is one of the important parameters for cells vitality. On the other hand the net charge of the peptide is around +1 in theory at the pH of 6.30, which is lower than its net charge at neutral pH. This slight change of pH is also reflected in the zeta potential measurements where the surface charge changes from slightly negative to slightly positive upon addition of peptide into the medium. Although small, this pH change may affect the solubility of the peptide as some small crystals are observed in solution when peptide is introduced to the medium.

5.2. CYTOTOXICITY OF PEPTIDE A10K FOR VARIOUS CELL LINES

As a first stage of the potential application of biotechnology, the compatibility of cell survival for the assignment of the peptide should to be considered. There are couples of techniques to determine cell viability. MTS is one of the major colorimetric techniques to be utilized and is employed for different cell lines.

5.2.1 Tetrazolium Salt Based Assay (MTS Assay)

During the experimental study HUVEC, Vero, TM3, HaCaT and HDF cells were used for the determination of cytotoxicity of A10K peptide. All experiments are done in triplicate. Additionally HaCaT and HDF cells were used for scratch assay to investigate the promoting or inhibiting effect of peptide for wound healing which is described.

Commercially purchased cells which are previously frozen and kept in liquid nitrogen are incubated at T75 wells in medium at 37 °C in humidified 5 per cent CO₂ and 95 per cent air for the growth for approximately ten days to obtain sufficient amount of cells. For HDF cells, medium was prepared using 10 per cent FBS, 1 per cent Penicillin-

Streptomycin/Antimycotic (antibiotic) and phenol red containing DMEM-low glucose concentration (1g/L) (1X) with pH 7.4, whereas for the other cells DMEM-high glucose concentration (4.5g/L) is utilized.

The cells were grown until they reach logarithmic phase growth at the wells. Afterwards the tetrazolium salt based assay [3-(4,5-dimethylthiazol-2-yl)-5-(3-carboxymethoxyphenyl)-2-(4-ulfophenyl)-2H-tetrazolium, inner salt (MTS)] was employed according to the manufacturer's protocol (CellTiter96®, Promega). MTS is one of the major colorimetric techniques for assessing cell cytotoxicity. Viable cells receive MTS into their mitochondria in the presence of phenazinemethosulfate (PMS) and metabolize it into blue formazan crystals that are then detected by spectrometric instruments. For evaluation of cell survival by MTS, 5×10^3 cells were inoculated in 100 μ L of media in each well of a 96-well plate and incubated for 24 h.

On the other hand peptide solution was prepared in 10 per cent H₂O contained DMEM medium (v:v) for the concentration of 2×10^4 μ g/mL. Then serial dilution was performed for the concentrations of 5000 μ g/mL and 1000 μ g/mL (v:v). All these samples were filtered through 0.2 μ m regenerated cellulose filter and introduced to the cells.

5.2.2. Cell Viability Results of Peptide A10K for Different Cell Lines

A10K peptide was treated with different cell lines to investigate if the peptide is toxic or non-toxic. HUVEC, Vero, TM3, HDF and HaCaT cells were grown and MTS test (it was described previously in detail in Section 5.2.1) were performed and the peptide is generally found to be non-toxic to the all chosen cell lines. Figure 5.2-5.6 demonstrates the relevant results of MTS test.

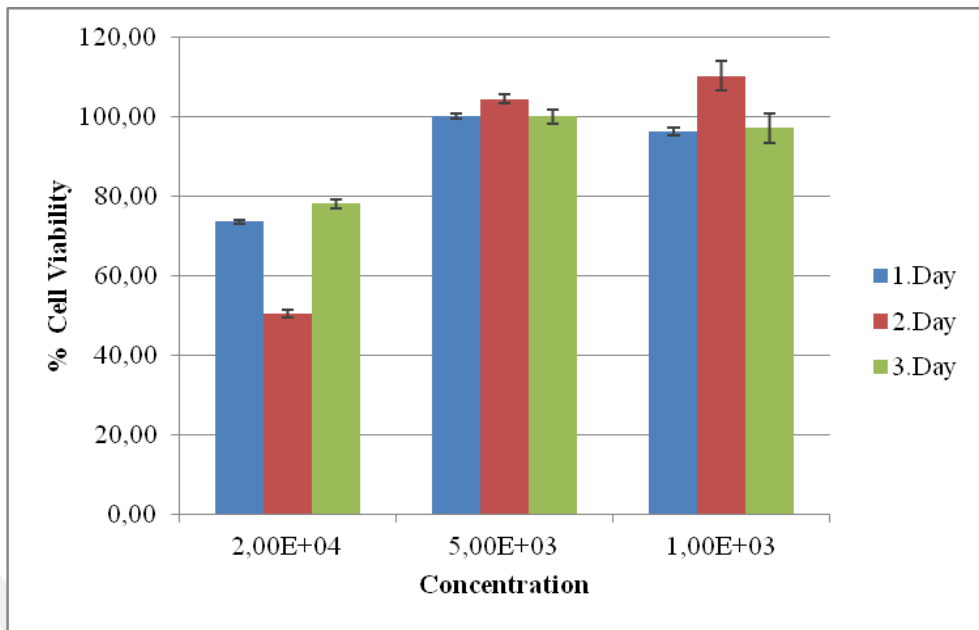


Figure 5.2. A10K viability for HUVEC

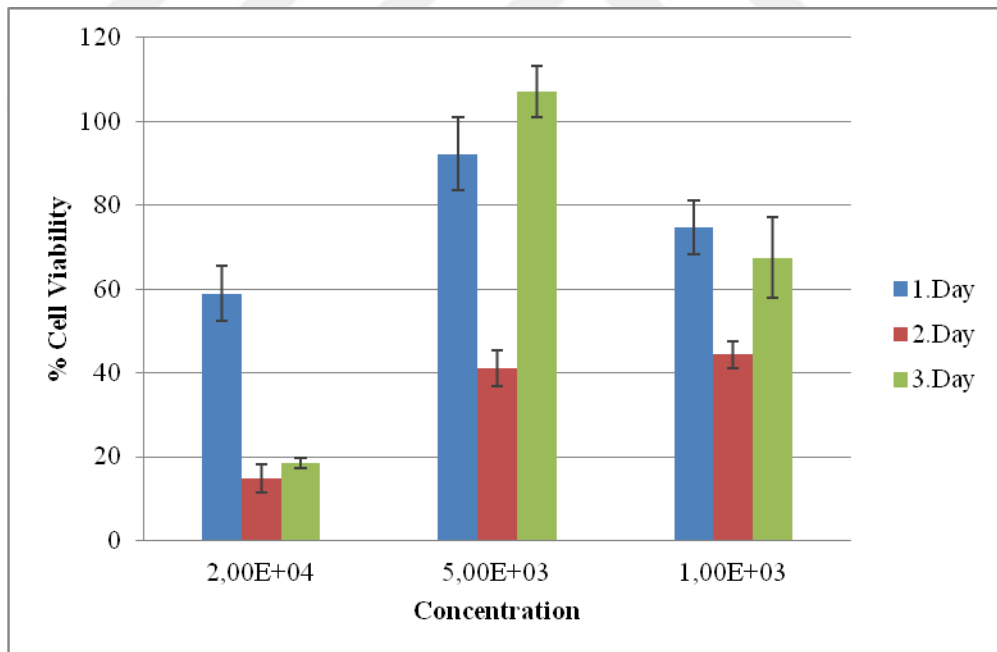


Figure 5.3. A10K viability for VERO

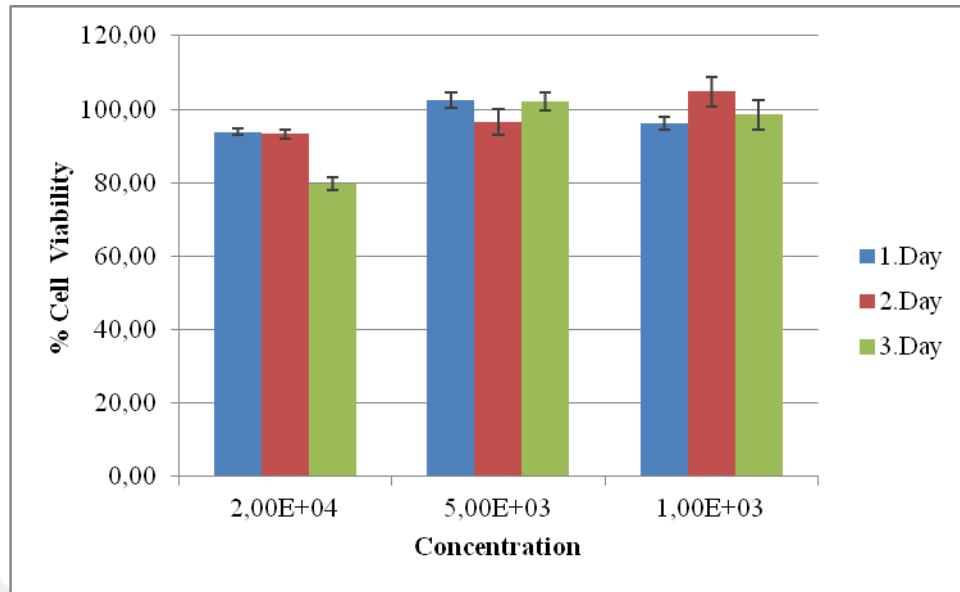


Figure 5.4. A10K viability for TM3

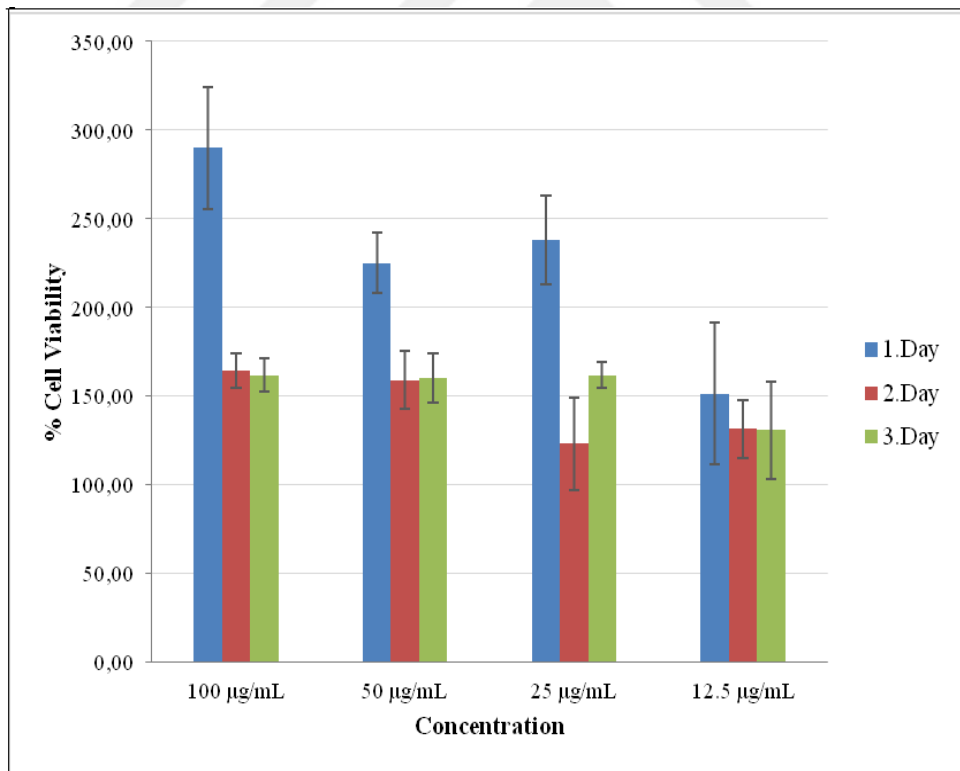


Figure 5.5. A10K viability for HDF

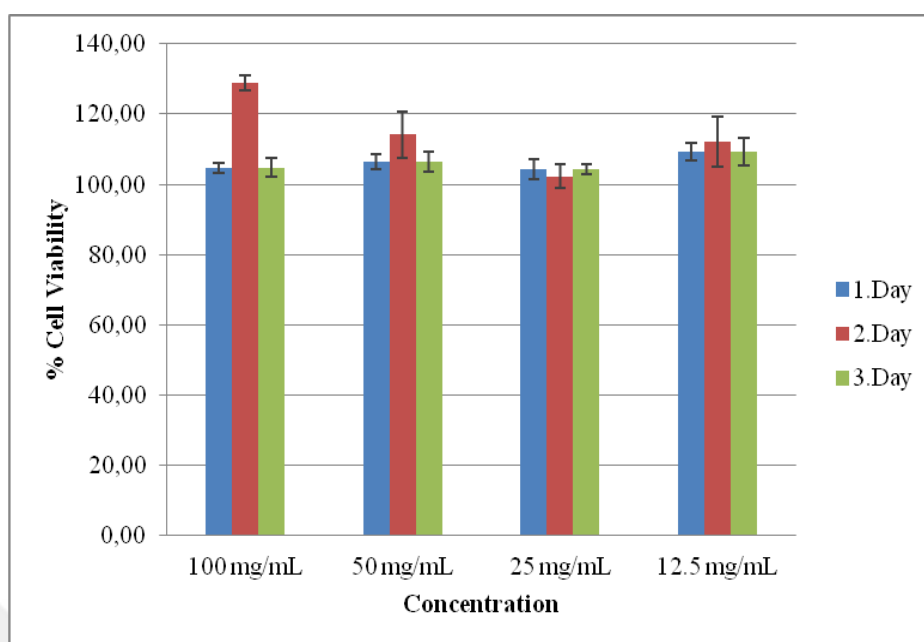


Figure 5.6. A10K viability for HaCaT

TM3 cells showed a great potential for peptide solutions for all concentrations. Unless increasing concentration exhibits a slight decrease of cell survival, respectively. The highest concentration of HUVEC and especially Vero indicated smaller cell growth. Even, 20000 $\mu\text{g/mL}$ of Vero revealed to be toxic second and third day. HDF and HaCaT cells have been demonstrated great potential for proceeding with wound healing studies.

5.3. APPLICATION OF THE PEPTIDE SOLUTION FOR WOUND HEALING

5.3.1. Preparation of Scratch Assay

HaCaT and HDF cells were utilized for performing wound healing process for the effect of peptide on the scratch. These cells were chosen on purpose. HaCaT is a type of cell that is immortalized human keratinocytes and is extensively in charge to study epidermal homeostasis and its pathophysiology. Although transformation of the cells brings a novel phenotypic features not found in normal cells, HaCaT cell line is extensively employed as a model for the great potential of easy propagation and having a near phenotype to the normal cell [98, 99]. Additionally, HDF cells were utilized to investigate the closure of the

wound. This is a type of fibroblast cells isolated from human foreskin to have the application as a model of primary cells. However, the limitations of the study of primary cells and the complication of handling the cells of attachment to the surface, HDF cells were not keep as the major line to obtain sufficient results. Still, the images of the HDF cells were submitted at Appendix A.

The HaCaT cells were grown according to the protocol that was previously described at Section 5.2.1. Afterwards 2×10^5 cells were seeded to 24-well plates for negative control and samples for triplicate. The cells were left to incubation overnight to obtain full cell growth on the surface of each well.

Prior to treat the peptide solutions as a sample to the cells, the peptide was dissolved in water to prepare a stock solution of 50 mg/mL. Then, calculated amounts of the stock solution were transferred into a flask in order to obtain 100 $\mu\text{g/mL}$, 50 $\mu\text{g/mL}$, 25 $\mu\text{g/mL}$ and 12, 5 $\mu\text{g/mL}$ concentrations by diluting them with medium.

When sufficient amount of cells were grown in 24-well plates, 1000 μL of a tip is used to perform the scratch on to the surface of the cells for each well. Later, the medium of the cells were removed and the cells were washed with using PBS. The prepared peptide solutions at desired concentrations were treated to the cells as a next step. Closure of the cells of the wound were monitored to have the comparison between the cells with peptide solutions and with the ones contain just medium. So, the distance between the scratch was measured by using light microscopy at certain time intervals (0, 12 and 24 hours).

5.4. RESULTS OF SCRATCH ASSAYS

As mentioned scratch assay was performed for two different cell lines, below is the relevant data for HaCaT cells.

5.4.1. Utilization of A10K for Scratch Assay by using HaCAT Cells

The healing process of HaCaT cells was investigated according to the distance between the scratch boundaries. Basically the idea depends on to monitoring cell growth in the area of

the scratch. Therefore, the gap needs to be covered by cells with respect to time. The relevant microscopy images of scratches for HaCaT cells are submitted in Figure 5.7.

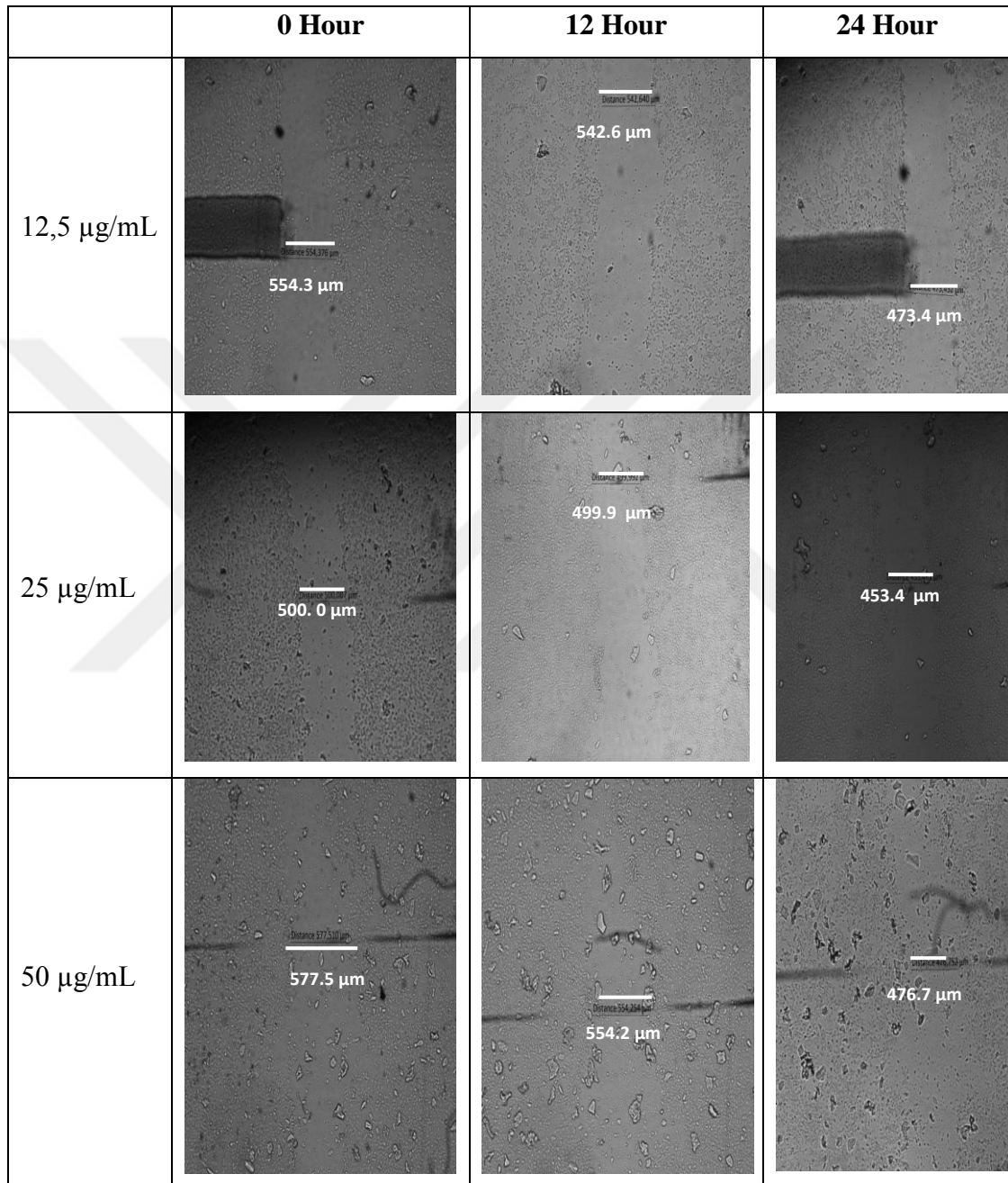


Figure 5.7. Light Microscopy images of scratch assay for HaCaT cells

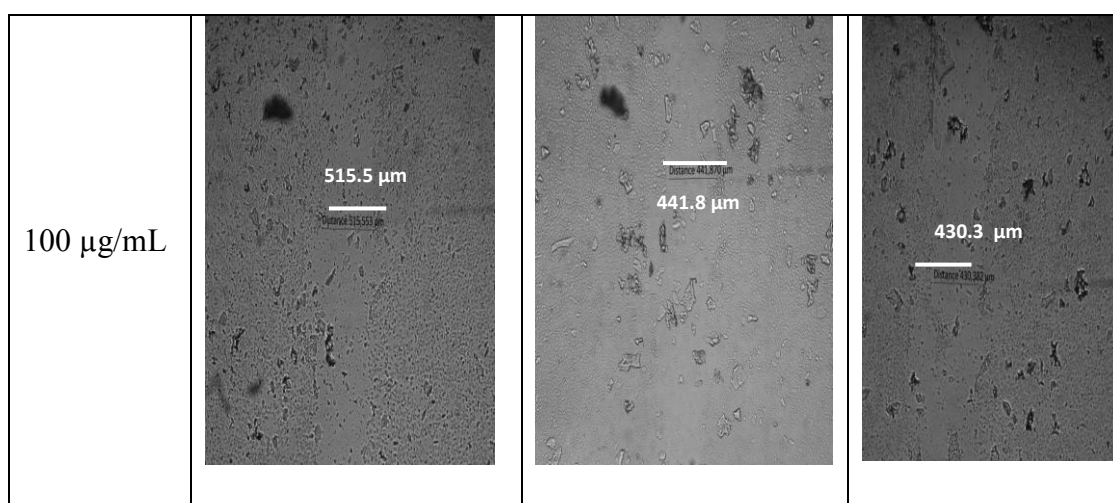


Figure 5.7. Light Microscopy images of scratch assay for HaCaT cells (continued)

Each scratch belongs to the sample containing peptide in medium (for varying concentrations) and the one with just medium, namely negative control was also observed. Prior of the introduction of the cells to the wells, each well has been drawn as three lines at the bottom side of the plate are drawn to each well. This was done to obtain the identical location of the scratches each time at different time intervals. Each well has three lines and all the experiments were performed triplicate which means three wells for each sample. Thus, ‘# **position**’ at the tables refers to the location of the scratch for each well. For instance if the position is 1-1, this means the first well of the relevant sample at the first line was considered.

Table 5.4-5.7 shows the changes in the distances of the wound for percentage. Wound closure for different time intervals were indicated at the table.

Table 5.4. Per cent closure of the wound for 12.5 µg/mL A10K at various time intervals

# position	$\Delta(0-12\text{Hour})$		$\Delta(12-24\text{Hour})$		$\Delta(0-24\text{ Hour})$	
	12.5 µg/mL	NC	12.5 µg/mL	NC	12.5 µg/mL	NC
1-1	2.12	0.73	12.75	2.95	14.60	3.67

1-2	5.77	7.68	4.76	10.97	10.26	17.80
1-3	25.29	2.01	3.72	3.27	28.07	5.21
2-1	9.33	2.85	6.61	1.70	15.32	4.50
2-2	9.79	1.82	8.50	1.36	17.46	3.15
2-3	13.06	2.75	2.12	6.85	14.90	9.42
3-1	3.00	3.65	6.17	2.82	8.98	6.36
3-2	12.34	3.23	3.66	1.67	15.54	4.84
3-3	31.15	6.32	5.84	1.91	35.18	8.11
Mean					17.81 %	7.01

Table 5.5. Per cent closure of the wound for 25 µg/mL A10K at various time intervals

# position	Δ(0-12Hour)		Δ(12-24Hour)		Δ(0-24 Hour)	
	25 µg/mL	NC	25 µg/mL	NC	25 µg/mL	NC
1-1	5.11	0.73	4.62	2.95	9.49	3.67
1-2	12.51	7.68	1.50	10.97	13.82	17.80
1-3	3.33	2.01	6.21	3.27	9.33	5.21
2-1	10.76	2.85	2.59	1.70	13.08	4.50
2-2	5.67	1.82	13.54	1.36	18.44	3.15
2-3	22.23	2.75	4.29	6.85	25.56	9.42
3-1	0.00	3.65	9.30	2.82	9.30	6.36
3-2	2.61	3.23	17.45	1.67	19.61	4.84
3-3	7.84	6.32	13.43	1.91	20.22	8.11
Mean					15.43 %	7.01

Table 5.6. Per cent closure of the wound for 50 µg/mL A10K at various time intervals

# position	Δ(0-12Hour)		Δ(12-24H)		Δ(0-24 Hour)	
	50 µg/mL	NC	50 µg/mL	NC	50 µg/mL	NC
1-1	1.71	0.73	9.56	2.95	11.11	3.67
1-2	4.03	7.68	13.98	10.97	17.45	17.80
1-3	20.86	2.01	27.87	3.27	42.92	5.21
2-1	3.78	2.85	21.56	1.70	24.53	4.50
2-2	N/A	1.82	42.23	1.36	14.58	3.15
2-3	3.70	2.75	5.38	6.85	8.89	9.42
3-1	14.49	3.65	23.73	2.82	34.78	6.36
3-2	18.46	3.23	30.86	1.67	43.62	4.84
3-3	16.55	6.32	5.40	1.91	21.06	8.11
Mean					24.33 %	7.01 %

Table 5.7. Per cent closure of the wound for 100 µg/mL A10K at various time intervals

#position	Δ(0-12 Hour)		Δ(12-24 Hour)		Δ(0-24 Hour)	
	100 µg/mL	NC	100 µg/mL	NC	100 µg/mL	NC
1-1	17.11	0.73	28.55	2.95	40.78	3.67
1-2	8.95	7.68	4.45	10.97	13.00	17.80
1-3	12.90	2.01	12.95	327	24.19	5.21
2-1	14.29	2.85	2.60	170	16.52	4.50
2-2	11.41	1.82	25.75	136	34.22	3.15
2-3	3.25	2.75	8.72	6.85	11.69	9.42
3-1	7.84	3.65	4.71	2.82	12.18	6.36
3-2	2.08	3.23	4.72	1.67	6.70	4.84
3-3	28.41	6.32	11.89	1.91	36.92	8.11
Mean					21.80 %	7.01 %

It is clearly seen that scratch has covered up better for the wells that contain peptide solutions compared to the negative control. The concentration of 50 µg/mL has revealed greater closure relatively to the others. One aspect could be a possible promotion of one of the receptors at the signaling pathways that regulates a protein synthesis for cells growth. Since some small peptides has this ability. Tang showed that, 11 amino acids residues Tiger 17 peptide (WCKPKPKPRCH) stimulates mitogen-activated protein kinase (MAPK). MAPK is a class of protein kinase that corresponds to signal the surface of the receptor and nucleus of the DNA [100, 101]. MAPKs have been indicated a significant promoting task in wound healing. Tiger17's revealed an effect on MAPK signaling pathways and were assayed in macrophage cells by using Western immunoblot analysis. Results of western blot analysis exhibited that Tiger17 significantly increased the activation of c-Jun N-terminal kinase (JNK) and extracellularly-responsive kinase (ERK) sub-group of MAPK signaling pathway and appeared to be a concentration-dependent manner [102].

5.4.2. Utilization of A10K for Scratch Assay by using HDF Cells

The same approach of wound assays were also performed for HDF cells. As it was previously demonstrated in Materials and Methods section, HDF cells were primer cell lines that were isolated from actual human foreskin. Although primer cell lines have remarkable features for *in vitro* studies, there are some handling complications of this cells relatively immortal cell lines. It is known that primer cell lines should have low passage numbers for not loosing the characteristic of cell morphology. Also a great care should be taken into account that these cells which are relatively fragile.

In the current study, utilizing HDF cells for scratch were for determining the accurate distance of the wound side. Eventually, the cells revealed some peels to the medium and difficulty attached to the surface of the wells after scratch during the experiment. All the relevant results are submitted in Appendix A.

As a conclusion, HaCaT cells revealed great potential for A10K peptide for the activity of wound healing and the convenient cell line to perform the study.

6. RESULTS AND DISCUSSION

It is possible to conclude that the physicochemical features of peptides bring an increasing attention to previous research of biotechnology. Outcomes of the improvements of nanotechnology and developments of imaging techniques at nano or micro scales supply promising data for various applications.

It is known that the molecules having regions both hydrophobic and separate hydrophilic part tend to self-assemble in aqueous medium and form basic structures such as micelles, tubes or fibrils. This is mostly due to the effect of hydrophobicity. The theory behind that is the nonpolar region which drives away from water and has a tendency to get closer to the nonpolar side. Mostly the small assemblies once form that follow extensive associated structures. Hence, the shape of the formed supramolecular structures and their dimensions are strongly related with the factors such as geometry of the polar and nonpolar groups and shape of the each molecule [39, 103, 104].

Some of the strong reasons of increasing attention of investigation of self-assembly for peptides are generation of well-defined structures, relatively simple functionalization, having fast synthesis processes and ability of biometabolism [104-106]. So, peptides have been utilized by scientists to consider great potential. It was recognized that sufficient amount of work was reported for oligopeptides or small peptide molecules that are end-capped, assemble to form nanotemplates [2, 34, 39, 41, 52, 107, 108]. On the other hand, to the best of our knowledge, there is a lack of study for non-capped small peptide molecules. Here, the investigated model peptides are non-capped to consider the variation of intramolecular interactions that likely affect the forming structures. One of the first studies was reported by Bucak that synthetic A6K self-assembles into long nanotubes with a cross-sectional radius of 26 nm for a certain size in great detail supported by cryo-TEM [3].

In the current study, the model peptide A6K provides novel data considering how if the peptide is investigated at varying pH through addition of NaOH and at different counterion forms of the peptide.

Firstly, $(tfa)_2-A_6K$ was considered in H_2O since the previous findings revealed [3] above 12 per cent cac, the solution transfers into nematic phase that is shown at Figure 6.1. It was expected to have higher ‘cac’ values of peptide in H_2O due to the greater polar interactions of D_2O . In comparison of two systems, the same concentration of 10 per cent is likely turbid. 12 per cent of the one in H_2O signs increasing turbidity presumably having assembled fragments for transition of nematic phase, it still provides slightly molecularly disperse solution.

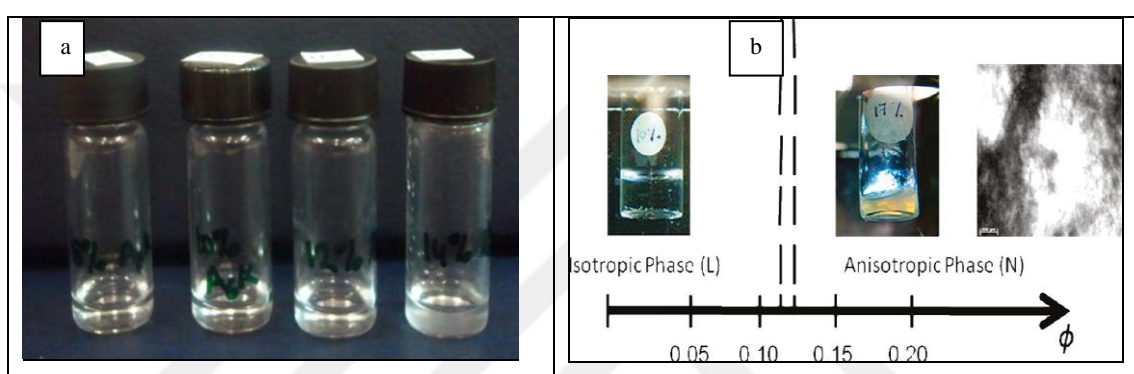


Figure 6.1. Physical features of $(tfa)_2-A_6K$ in H_2O a) Turbidity of $(tfa)_2-A_6K$ in H_2O
b) Turbidity and birefringency of $(tfa)_2-A_6K$ in D_2O [3]

Additionally, extended partial phase diagram of $(tfa)_2-A_6K$ were grouped five different phases and the regions are classified, clear, precipitation, nematic nanotubes, thin sheets or elliptical cylinders and hydrolysis. Mostly, the peptides started to form secondary structures of β -sheets for the mass fractions of w_i , around 0.08 while x is around 0.2. It is observed that when the w_i increases, structures starts to appear at lower x values. To confirm the observations with the experimental results of SAXS, elliptical cylinder was obtained the most convenient model for self-assembled structures.

In the point of cell study, it was seen that peptides were non-toxic the cell lines (HaCaT and HDF) for low concentrations such as 12.5 $\mu g/mL$ and 1000 $\mu g/mL$. The cells were considered non-toxic if the viability is greater than 90 per cent and if the viability is 80 per cent, then the cells were considered 20 per cent toxic [109, 110]. Vero which is one of the studied cells responds less compatible cell line relatively to the others for the peptide in observation above given statement. Although 20000 $\mu g/mL$ concentrations for Vero

revealed toxic for the peptide. HUVEC revealed 40 per cent-80 per cent cell viability for the first day for concentrations 20000 $\mu\text{g}/\text{mL}$ -5000 $\mu\text{g}/\text{mL}$. Also, TM3 cells were 20 per cent toxic for 20000 $\mu\text{g}/\text{mL}$ for third day. In the point of toxicity, there are sufficient amount of studies for peptides exhibits antimicrobial effect for some cell lines [111-114]. Vaucher et al. investigated P34 peptide and nisin for different eukaryotic cells for varying concentrations (0.02–2.5 $\mu\text{g}\cdot\text{ml}^{-1}$) [115]. The obtained EC50 value was 0.60 and 1.25 $\mu\text{g}\cdot\text{ml}^{-1}$ for P34 while it was 0.50 and 1.04 $\mu\text{g}\cdot\text{ml}^{-1}$ for nisin.

HDF and HaCaT, which two of these cells are quite convenient for cell survival to apply wound study. One aspect for HaCaT is its ability of expressing all epidermal differentiation markers in the tissue [116]. Thus, the role of those cells for wound healing has a great potential. HDF cells which used in the current study have some complications to handle for the wound study since the cells tend to peell on the surface of the well. These cells were primer cells that were isolated from a human foreskin. Regardless the images of preliminary studies of HDF were submitted in Appendix A.

HaCaT cells respond a great potential for healing of scratch relatively control cells. Depending on to the concentration, closure of the wound was obtained between 25 per cent-15 per cent for the cells contain A10K in 24 hours while it was 7 per cent for the cells healed in control medium. In the point of peptide level in the medium, 50 $\mu\text{g}/\text{mL}$ was obtained greater potential for the closure of the gap in the wound relatively to the other samples. In the literature, peptides or materials modified with using peptides are revealed to promote wound healing [102, 117, 118]. Thus, this is expectable and compatable for the approach of biotechnology. The relevant wound closure is submitted in Appendix A for HaCaT. It is possible to follow the migration of the cells towards the scratch during the increasing time.

As a future study the peptides, A6K or A10K, can be utilized to prepare a wound healing formulation to increase the efficiency. Also for the tissues or injuries that needs a rapid threatment; the peptide can be explored as a potential candidate for wound healing.

REFERENCES

1. Cenker CC, Bucak S, Olsson U. Aqueous self-assembly within the homologous peptide series AnK. *Langmuir*. 2014;30(33):10072-9.
2. Toksöz S, Guler MO. Self-assembled peptidic nanostructures. *Nano Today*. 2009;4(6):458-69.
3. Bucak S, Cenker C, Nasir I, Olsson U, Zackrisson M. Peptide nanotube nematic phase. *Langmuir*. 2009;25(8):4262-5.
4. Ulijn RV, Smith AM. Designing peptide based nanomaterials. *Chemical Society Reviews*. 2008;37(4):664-75.
5. Howl J. *Peptide synthesis and applications*. Wolherhampton,UK: Springer Science & Business Media; 2005.
6. Reches M, Gazit E. Molecular self-assembly of peptide nanostructures: mechanism of association and potential uses. *Current Nanoscience*. 2006;2(2):105-11.
7. Scanlon S, Aggeli A. Self-assembling peptide nanotubes. *Nano Today*. 2008;3(3):22-30.
8. De Yoreo JJ, Sommerdijk N. Investigating materials formation with liquid-phase and cryogenic TEM. *Nature Reviews Materials*. 2016;1:16035.
9. Nelson DL, Lehninger AL, Cox MM. *Lehninger principles of biochemistry*: Macmillan; 2008.
10. Academy K. Chemistry of Amino Acids and Protein Structure [cited 2018]. Available from: <https://www.khanacademy.org/test-prep/mcat/biomolecules/amino-acids-and-proteins1/a/chemistry-of-amino-acids-and-protein-structure.>]
11. Smith JG. *Organic Chemistry*. New York: McGraw-Hill International Edition; 2008.
12. Wu G. Amino acids: metabolism, functions, and nutrition. *Amino acids*. 2009;37(1):1-17.

13. Bodanszky M. *Peptide chemistry*: Springer; 1988.
14. McNaught AD, McNaught AD. *Compendium of chemical terminology*: Blackwell Science Oxford; 1997.
15. Chang R. *Chemistry*. New York: McGraw-Hill International Edition; 2007.
16. Cagri CC. *Characterisation of Oligopeptide A6K*. Lund: Lund University; 2009.
17. Sadava D, Hillis D, Heller C, Berenbaum M. *Life: The Science of Biology: Ninth Edition Textbook*. Gordonsville: Sinauer Associates; 2011.
18. Kajava AV, Squire JM, Parry DA. β -Structures in fibrous proteins. *Advances in Protein Chemistry*. 2006;73:1-15.
19. Liu Y, Carbonell J, Klein-Seetharaman J, Gopalakrishnan V, editors. Prediction of parallel and anti-parallel beta-sheets using Conditional Random Fields. *Research Showcase at CMU*; 2015; Carnegie Mellon University Research Showcase
20. Petsko GA, Ringe D. *Protein structure and function*. London: New Science Press; 2004.
21. Bragg L, Kendrew JC, Perutz MF. Polypeptide chain configurations in crystalline proteins. *Proceedings of the Royal Society of London A: Mathematical, Physical and Engineering Sciences*. 1950;203(1074):321-57.
22. Suart B. *Infrared Spectroscopy Fundamental and Applications*. New York: John Wiley & Sons, Ltd; 2004.
23. Israelachvili JN, Mitchell DJ, Ninham BW. Theory of self-assembly of hydrocarbon amphiphiles into micelles and bilayers. *Journal of the Chemical Society, Faraday Transactions 2: Molecular and Chemical Physics*. 1976;72:1525-68.
24. Whitesides GM, Grzybowski B. Self-assembly at all scales. *Science*. 2002;295(5564):2418-21.

25. Ball P, Borley NR. *The self-made tapestry: pattern formation in nature*. Oxford: Oxford University Press; 1999.
26. Hartgerink JD, Beniash E, Stupp SI. Self-assembly and mineralization of peptide-amphiphile nanofibers. *Science*. 2001;294(5547):1684-8.
27. Philp D, Stoddart JF. Self-assembly in natural and unnatural systems. *Angewandte Chemie (International Edition in English)*. 1996;35(11):1154-96.
28. Rajagopal K, Schneider JP. Self-assembling peptides and proteins for nanotechnological applications. *Current Opinion in Structural Biology*. 2004;14(4):480-6.
29. Desii A, Chiellini F, Duce C, Ghezzi L, Monti S, Tiné MR, et al. Influence of structural features on the self-assembly of short ionic oligopeptides. *Journal of Polymer Science Part A: Polymer Chemistry*. 2010;48(4):889-97.
30. Schneider JP, Pochan DJ, Ozbas B, Rajagopal K, Pakstis L, Kretsinger J. Responsive hydrogels from the intramolecular folding and self-assembly of a designed peptide. *Journal of the American Chemical Society*. 2002;124(50):15030-7.
31. Yang SJ, Zhang S. Self-assembling behavior of designer lipid-like peptides. *Supramolecular Chemistry*. 2006;18(5):389-96.
32. Colombo G, Soto P, Gazit E. Peptide self-assembly at the nanoscale: a challenging target for computational and experimental biotechnology. *TRENDS in Biotechnology*. 2007;25(5):211-8.
33. Cao M, Lu S, Zhao W, Deng L, Wang M, Wang J, et al. Peptide self-assembled nanostructures with distinct morphologies and properties fabricated by molecular design. *ACS Applied Materials & Interfaces*. 2017;9(45):39174-84.
34. Zhang S, Holmes T, Lockshin C, Rich A. Spontaneous assembly of a self-complementary oligopeptide to form a stable macroscopic membrane. *Proceedings of the National Academy of Sciences*. 1993;90(8):3334-8.

35. Fung S, Keyes C, Duhamel J, Chen P. Concentration effect on the aggregation of a self-assembling oligopeptide. *Biophysical Journal*. 2003;85(1):537-48.
36. Caplan MR, Schwartzfarb EM, Zhang S, Kamm RD, Lauffenburger DA. Control of self-assembling oligopeptide matrix formation through systematic variation of amino acid sequence. *Biomaterials*. 2002;23(1):219-27.
37. Vauthey S, Santoso S, Gong H, Watson N, Zhang S. Molecular self-assembly of surfactant-like peptides to form nanotubes and nanovesicles. *Proceedings of the National Academy of Sciences*. 2002;99(8):5355-60.
38. Von Maltzahn G, Vauthey S, Santoso S, Zhang S. Positively charged surfactant-like peptides self-assemble into nanostructures. *Langmuir*. 2003;19(10):4332-7.
39. Zhang S, Marini DM, Hwang W, Santoso S. Design of nanostructured biological materials through self-assembly of peptides and proteins. *Current Opinion in Chemical Biology*. 2002;6(6):865-71.
40. Santoso S, Hwang W, Hartman H, Zhang S. Self-assembly of surfactant-like peptides with variable glycine tails to form nanotubes and nanovesicles. *Nano Letters*. 2002;2(7):687-91.
41. Zhao X. Design of self-assembling surfactant-like peptides and their applications. *Current Opinion in Colloid & Interface Science*. 2009;14(5):340-8.
42. Fernandez-Lopez S, Kim H-S, Choi EC, Delgado M, Granja JR, Khasanov A, et al. Antibacterial agents based on the cyclic D, L- α -peptide architecture. *Nature*. 2001;412(6845):452-5.
43. Hartgerink JD, Clark TD, Ghadiri MR. Peptide nanotubes and beyond. *Chemistry—A European Journal*. 1998;4(8):1367-72.
44. Valéry C, Paternostre M, Robert B, Gulik-Krzywicki T, Narayanan T, Dedieu J-C, et al. Biomimetic organization: Octapeptide self-assembly into nanotubes of viral capsid-like dimension. *Proceedings of the National Academy of Sciences*. 2003;100(18):10258-62.

45. Fändrich M, Fletcher MA, Dobson CM. Amyloid fibrils from muscle myoglobin. *Nature*. 2001;410(6825):165-6.
46. Lynn DG, Meredith SC. Review: model peptides and the physicochemical approach to β -amyloids. *Journal of Structural Biology*. 2000;130(2-3):153-73.
47. McLaurin J, Yang D-S, Yip C, Fraser P. Review: modulating factors in amyloid- β fibril formation. *Journal of Structural Biology*. 2000;130(2-3):259-70.
48. Perutz MF, Finch JT, Berriman J, Lesk A. Amyloid fibers are water-filled nanotubes. *Proceedings of the National Academy of Sciences*. 2002;99(8):5591-5.
49. Reches M, Porat Y, Gazit E. Amyloid fibril formation by pentapeptide and tetrapeptide fragments of human calcitonin. *Journal of Biological Chemistry*. 2002;277(38):35475-80.
50. Serpell LC. Alzheimer's amyloid fibrils: structure and assembly. *Biochimica et Biophysica Acta (BBA)-Molecular Basis of Disease*. 2000;1502(1):16-30.
51. Scheibel T, Kowal AS, Bloom JD, Lindquist SL. Bidirectional amyloid fiber growth for a yeast prion determinant. *Current Biology*. 2001;11(5):366-9.
52. Zhang S. Fabrication of novel biomaterials through molecular self-assembly. *Nature Biotechnology*. 2003;21(10):1171-8.
53. Hwang W, Marini DM, Kamm RD, Zhang S. Supramolecular structure of helical ribbons self-assembled from a β -sheet peptide. *The Journal of Chemical Physics*. 2003;118(1):389-97.
54. Perutz M, Pope B, Owen D, Wanker EE, Scherzinger E. Aggregation of proteins with expanded glutamine and alanine repeats of the glutamine-rich and asparagine-rich domains of Sup35 and of the amyloid β -peptide of amyloid plaques. *Proceedings of the National Academy of Sciences*. 2002;99(8):5596-600.
55. Perutz MF. Glutamine repeats and neurodegenerative diseases: molecular aspects. *Trends in Biochemical Sciences*. 1999;24(2):58-63.

56. Nagai A, Nagai Y, Qu H, Zhang S. Dynamic behaviors of lipid-like self-assembling peptide A6D and A6K nanotubes. *Journal of Nanoscience and Nanotechnology*. 2007;7(7):2246-52.
57. Castelletto V, Nutt DR, Hamley IW, Bucak S, Cenkler Ç, Olsson U. Structure of single-wall peptide nanotubes: in situ flow aligning X-ray diffraction. *Chemical Communications*. 2010;46(34):6270-2.
58. Cenkler CC, Bucak S, Olsson U. Nanotubes and bilayers in a model peptide system. *Soft Matter*. 2011;7(10):4868-75.
59. Somuncu ÖS, Taşlı PN, Şişli HB, Somuncu S, Şahin F. Characterization and differentiation of stem cells isolated from human newborn foreskin tissue. *Applied Biochemistry and Biotechnology*. 2015;177(5):1040-54.
60. Murdock RC, Braydich-Stolle L, Schrand AM, Schlager JJ, Hussain SM. Characterization of nanomaterial dispersion in solution prior to in vitro exposure using dynamic light scattering technique. *Toxicological Sciences*. 2008;101(2):239-53.
61. Labs PPT. Analytical Testing Zeta potential analysis 2018 [cited 2018]. Available from: <https://www.particletechlabs.com/analytical-testing/zeta-potential-analysis>.
62. Caputo F. Measuring Zeta Potential. Project EUNCL2015. p. 1-4.
63. Antony PPMA, Trefois C, Stojanovic A, Baumuratov AS, Kozak K. Light microscopy applications in systems biology: opportunities and challenges. *Cell Communication and Signaling*. 2013;11(1):24.
64. Gustafsson M, Agard D, Sedat J. I5M: 3D widefield light microscopy with better than 100nm axial resolution. *Journal of Microscopy*. 1999;195(1):10-6.
65. Thorn K. A quick guide to light microscopy in cell biology. *Molecular Biology of the Cell*. 2016;27(2):219-22.
66. GmbH B. Small Angle X-Ray Scattering 2016.

67. Glatter O. KO. *Small Angle X-Ray Scattering*. Graz, Austria: Academic Press; 1982.
68. Narayanan T. Synchrotron small-angle X-ray scattering. *Soft matter characterization*: Springer; 2008. p. 899-952.
69. Putnam CD, Hammel M, Hura GL, Tainer JA. X-ray solution scattering (SAXS) combined with crystallography and computation: defining accurate macromolecular structures, conformations and assemblies in solution. *Quarterly Reviews of Biophysics*. 2007;40(03):191-285.
70. Stewart PL. Cryo-electron microscopy and cryo-electron tomography of nanoparticles. *Wiley Interdisciplinary Reviews: Nanomedicine and Nanobiotechnology*. 2016;9(2):1-4.
71. Fernandez-Leiro R, Scheres SH. Unravelling biological macromolecules with cryo-electron microscopy. *Nature*. 2016;537(7620):339-46.
72. Stuart B. *Infrared Spectroscopy-Fundamentals and Applications*: Wiley 2004.
73. Mehrotra R. *Infrared Spectroscopy, Gas Chromatography/Infrared in Food Analysis*: Wiley Online Library; 2000.
74. Kumirska J, Czerwicka M, Kaczyński Z, Bychowska A, Brzozowski K, Thöming J, et al. Application of spectroscopic methods for structural analysis of chitin and chitosan. *Marine drugs*. 2010;8(5):1567-636.
75. Owen T. *Fundamentals of modern UV-visible spectroscopy: A primer*. Hewlett-Packard; 1996.
76. Owen T. *Fundamentals of modern UV-visible spectroscopy* Agilent technologies2000.
77. Pedersen J. *Neutrons, X-rays and light. scattering methods applied to soft condensed matter*. Amsterdam: Elsevier; 2002.
78. Verstappen N. pH dependence of A6K self-assembly: Internship Report. Lund University: 2013.

79. Cenker CC. *Equilibrium and Non-Equilibrium Aggregation in the Model Peptide Family AnX* [pH Thesis]. Sweden: Lund University; 2013.
80. Kahne D, Still WC. Hydrolysis of a peptide bond in neutral water. *Journal of the American Chemical Society*. 1988;110(22):7529-34.
81. Smith RM, Hansen DE. The pH-rate profile for the hydrolysis of a peptide bond. *Journal of the American Chemical Society*. 1998;120(35):8910-3.
82. Radzicka A, Wolfenden R. Rates of uncatalyzed peptide bond hydrolysis in neutral solution and the transition state affinities of proteases. *Journal of the American Chemical Society*. 1996;118(26):6105-9.
83. Nguyen D, Orgill D, Murphy G. The pathophysiologic basis for wound healing and cutaneous regeneration. *Biomaterials for Treating Skin Loss*: Elsevier; 2009. p. 25-57.
84. Michael Mercandetti M, MBA. Wound Healing and Repair 2017 [cited 2017 19 May]. Available from: <https://emedicine.medscape.com/article/1298129-overview>.
85. Diegelmann RF, Evans MC. Wound healing: an overview of acute, fibrotic and delayed healing. *Front Biosci*. 2004;9(1):283-9.
86. Midwood KS, Williams LV, Schwarzbauer JE. Tissue repair and the dynamics of the extracellular matrix. *The International Journal of Biochemistry & Cell Biology*. 2004;36(6):1031-7.
87. Guo Sa, DiPietro LA. Factors affecting wound healing. *Journal of Dental Research*. 2010;89(3):219-29.
88. Janis J, Attinger C. The basic science of wound healing. *Plastic and Reconstructive Surgery*. 2006;117(7):12-34.
89. Schneider A, Garlick JA, Egles C. Self-assembling peptide nanofiber scaffolds accelerate wound healing. *PloS One*. 2008;3(1):e1410.

90. Steinstraesser L, Koehler T, Jacobsen F, Daigeler A, Goertz O, Langer S, et al. Host defense peptides in wound healing. *Molecular Medicine*. 2008;14(7-8):528.
91. Steinstraesser L, Kraneburg UM, Hirsch T, Kesting M, Steinau H-U, Jacobsen F, et al. Host defense peptides as effector molecules of the innate immune response: a sledgehammer for drug resistance? *International Journal of Molecular Sciences*. 2009;10(9):3951-70.
92. Steinstraesser L, Hirsch T, Schulte M, Kueckelhaus M, Jacobsen F, Mersch EA, et al. Innate defense regulator peptide 1018 in wound healing and wound infection. *PloS One*. 2012;7(8):e39373.
93. Hirsch T, Jacobsen F, Steinau H-U, Steinstraesser L. Host defense peptides and the new line of defence against multiresistant infections. *Protein and Peptide Letters*. 2008;15(3):238-43.
94. Biosciences S. Dulbecco's Modified Eagle's Medium/High Modified. Product Information Data Sheet 2018.
95. RMBIO RMB, Inc. Rocky Mountain Biologicals, Inc. Certificate of Analysis 2016.
96. Scientific TF. Specification Data Sheet. Certified, US origin 2016.
97. Makowska J, Bagińska K, Liwo A, Chmurzyński L, Scheraga HA. Acidic-basic properties of three alanine-based peptides containing acidic and basic side chains: Comparison between theory and experiment. *Peptide Science*. 2008;90(5):724-32.
98. Seo M-D, Kang TJ, Lee CH, Lee A-Y, Noh M. HaCaT keratinocytes and primary epidermal keratinocytes have different transcriptional profiles of cornified envelope-associated genes to T helper cell cytokines. *Biomolecules & Therapeutics*. 2012;20(2):171.
99. Deyrieux AF, Wilson VG. In vitro culture conditions to study keratinocyte differentiation using the HaCaT cell line. *Cytotechnology*. 2007;54(2):77-83.

100. Cuenda A, Lizcano JM, Lozano J. Mitogen Activated Protein Kinases. *Frontiers in Cell and Developmental Biology*. 2017;5:80.
101. Johnson GL, Lapadat R. Mitogen-activated protein kinase pathways mediated by ERK, JNK, and p38 protein kinases. *Science*. 2002;298(5600):1911-2.
102. Tang J, Liu H, Gao C, Mu L, Yang S, Rong M, et al. A small peptide with potential ability to promote wound healing. *PLoS One*. 2014;9(3):e92082.
103. Annabi N, Mithieux SM, Camci-Unal G, Dokmeci MR, Weiss AS, Khademhosseini A. Elastomeric recombinant protein-based biomaterials. *Biochemical engineering journal*. 2013;77:110-8.
104. Habibi N, Kamaly N, Memic A, Shafiee H. Self-assembled peptide-based nanostructures: smart nanomaterials toward targeted drug delivery. *Nano Today*. 2016;11(1):41-60.
105. Cui H, Webber MJ, Stupp SI. Self-assembly of peptide amphiphiles: From molecules to nanostructures to biomaterials. *Peptide Science*. 2010;94(1):1-18.
106. Tsutsumi H, Sawada T, Mihara H. Development of Nano-and Bio-Materials Using Nanofibers Fabricated from Self-Assembling Peptides. *KOBUNSHI RONBUNSHU*. 2017;74(3):162-71.
107. Adamcik J, Castelletto V, Bolisetty S, Hamley IW, Mezzenga R. Direct Observation of Time-Resolved Polymorphic States in the Self-Assembly of End-Capped Heptapeptides. *Angewandte Chemie International Edition*. 2011;50(24):5495-8.
108. Zhang S, Lockshin C, Cook R, Rich A. Unusually stable β -sheet formation in an ionic self-complementary oligopeptide. *Biopolymers*. 1994;34(5):663-72.
109. Demir AB. *Investiagion and comparison of different irrigation solutions using cell culture technique*. Ankara: Ankara University; 2009.
110. Cam D. *Cellular uptake of modified silver nanoparticles and cytotoxicity* [Master]. Ankara: Gazi University; 2009.

111. Mangoni ML, McDermott AM, Zasloff M. Antimicrobial peptides and wound healing: biological and therapeutic considerations. *Experimental Dermatology*. 2016;25(3):167-73.
112. Paiva AD, de Oliveira MD, de Paula SO, Baracat-Pereira MC, Breukink E, Mantovani HC. Toxicity of bovicin HC5 against mammalian cell lines and the role of cholesterol in bacteriocin activity. *Microbiology*. 2012;158(11):2851-8.
113. Pfalzgraff A, Brandenburg K, Weindl G. Antimicrobial peptides and their therapeutic potential for bacterial skin infections and wounds. *Frontiers in Pharmacology*. 2018;9:281-283.
114. Teerasak E, Thongararm P, Roytrakul S, Meesuk L, Chumnanpuen P. Prediction of anticancer peptides against MCF-7 breast cancer cells from the peptidomes of *Achatina fulica* mucus fractions. *Computational and Structural Biotechnology Journal*. 2016;14:49-57.
115. Vaucher RA, Motta SA, Brandelli A. Evaluation of the in vitro cytotoxicity of the antimicrobial peptide P34. *Cell Biology International*. 2010;34(3):317-23.
116. Maas-Szabowski N, Stärker A, Fusenig NE. Epidermal tissue regeneration and stromal interaction in HaCaT cells is initiated by TGF- α . *Journal of Cell Science*. 2003;116(14):2937-48.
117. Hong Y, Shim H, Kim S, Choi N, Kim J, Hwang J, et al. The effects on dermal wound healing using novel peptide modified by bone morphogenic protein-2. *Tissue Engineering and Regenerative Medicine*. 2014;11(5):397-404.
118. Karaman O, Onak G, Demirci EA, Kahraman E. Integrin binding peptide promotes in vitro wound closure in the L929 mouse fibroblasts. *The European Research Journal*. 2017;3(3):207-13.

APPENDIX A: LIGHT MICROSCOPY IMAGES OF HaCaT AND HDF CELLS

Table A.1. Preliminary light microscopy images of scratch assay for HaCaT cells (Higher peptide concentration)

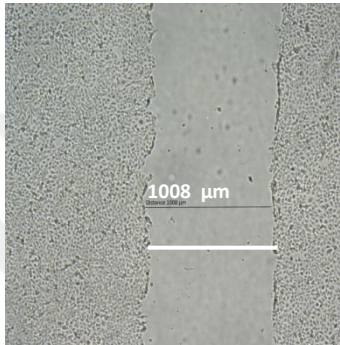
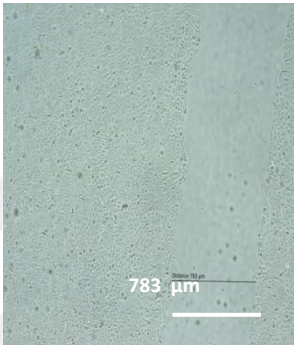
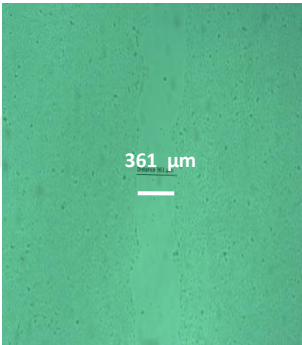
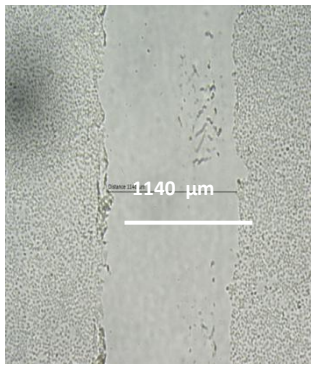
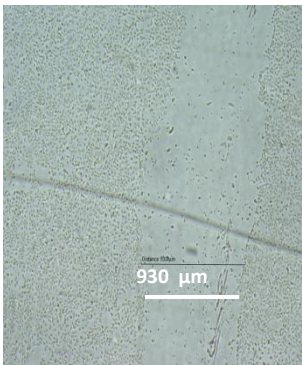
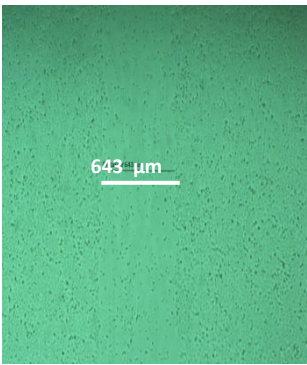
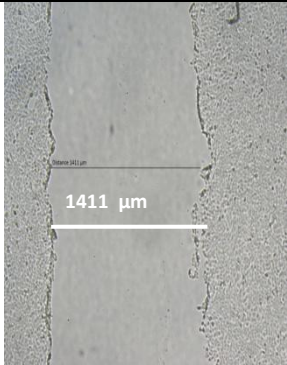
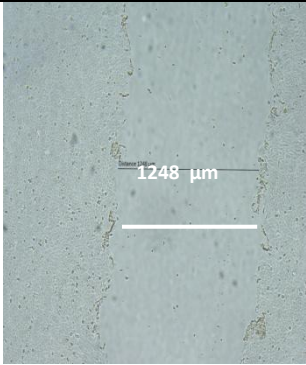
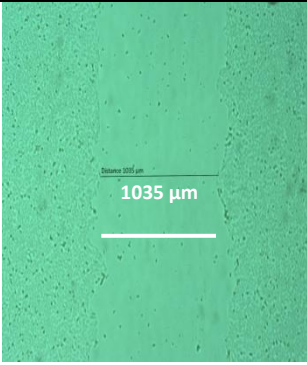

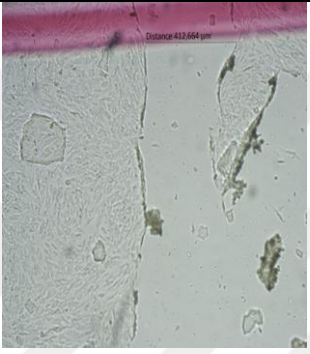
	0 Hour	12 Hour	24 Hour
NC			
NC-H₂O			
Peptide (0.5% or 5000 μg/mL)			

Table A.2. Preliminary light microscopy images of scratch assay for HDF cells

	0 Hour	12 Hour	24 Hour
12,5 µg/mL		NA	NA
100 µg/mL		NA	NA